Doctoral thesis

Terramechanics-based Analysis of Wheel Locomotion:

Proposal of Field Modeling Method and Extended Terramechanics Models

Yokohama National University

Graduate School of Engineering Science

Hirotaka Suzuki

March, 2021

Terramechanics-based Analysis of Wheel Locomotion:

Proposal of Field Modeling Method and Extended Terramechanics Models

Hirotaka Suzuki

Abstract

Terramechanics is an interdisciplinary field of study concerned with the interactions of off-road vehicles and machines with terrain . Its scope covers all types of off-road vehicles, including four-wheel drive (4WD) vehicles, construction machinery, agricultural machinery, and special vehicles. In recent years, it has also come to include lunar and planetary exploration equipment and disaster-response robots. However, a practical terramechanics-based analysis requires the development of a versatile method for modeling a wide variety of terrain surfaces, independently of the sophistication of the terramechanics model itself . The present work first discusses the usefulness and limitations of such methods . This is done by analyzing the multibody dynamics of mining dump trucks based on an existing terramechanics model and by examining the shape of rover-wheel grousers. Next, based on existing studies, a new method is proposed for creating a road-surface model. An extended terramechanics model is also presented that considers terrain surface deformations.

The eight chapters of this paper are outlined as follows.

Chapter 1 introduces the background of the present study and reviews relevant research, focusing on the terramechanics model and numerical analysis related to wheel locomotion. The purpose and contribution of this paper are also formulated.

Chapter 2 describes the terramechanics interaction model used in conventional wheel locomotion analysis. In particular, two typical terramechanics models, the Bekker-Wong-Reece (BWR) model and Resistive Force Theory (RFT), are introduced, and their application to wheel locomotion is outlined.

Chapter 3 describes the results of applying the terramechanics model to a multibody-dynamics analysis of mining dump trucks. A BWR model is used to describe the interaction between the tire and the ground, and the analysis results of the climbing performance on soft ground are shown. Furthermore, the effectiveness of the traction control system (a control method for avoiding becoming immobilized), is demonstrated based on a systematic numerical analysis.

Chapter 4 presents the results of a locomotion analysis of wheels with grousers, based on RFT. The appeal of RFT in recent years stems from its ability to analyze the interaction between an object with a complicated shape or movement and the ground at low cost . However, given the scant literature on applications of RFT to wheel locomotion, this chapter analyzes this phenomenon using both the discrete element method and RFT. By comparing the results obtained by both methods, the applicability and limitations of RFT are clarified.

Chapter 5 proposes a grouser shape designed to improve wheel runnability by combining model experiments, discrete element method analysis, and terramechanics analysis using RFT. Specifically, a grouser with a trapezoidal cross section is shown to exert a "packing effect" that is effective in avoiding immobilization.

Chapter 6 proposes a multi-stage analysis method that exploits ground-surface information obtained from other numerical analysis and measurement techniques. The data are applied to the terrain surface model of the terramechanics analysis. First, the outline of the multi-stage analysis method is explained. Then, the analysis method for generating wind ripple patterns is described, as a concrete example of the ground surface formation analysis.

Chapter 7 proposes an extended terramechanics model that considers the

deformations and changes in the terrain-surface properties associated with machine-ground interactions. In addition, the effectiveness of the model is demonstrated by comparing the model experiment results for plate drag and for wheel locomotion.

Chapter 8 closes with a concluding summary and an outlook of future prospects.

Contents

1 Introduction **1**

1.1 Background 1

1.1.1 Technical issues in terrain surface modeling 2

1.1.2 Technical issues of terramechanics model 3

1.2 Purpose and Approach 4

1.3 Organization of thesis 6

2 Terramechanics models **10**

2.1 Introduction 10

2.2 Bekker–Wong–Reece (BWR) model 10

2.2.1 Rigid wheels 10

2.2.2 Elastic wheel 13

2.3 Resistive Force Theory (RFT) 14

2.3.1 Overview of RFT 14

2.3.2 Application method of RFT 16

2.4 Review of terramechanics models 20

2.4.1 BWR model 20

2.4.2 RFT 21

2.4.3 Challenges and future prospects of terramechanics models 23

3 MBD analysis using a terramechanics model: Traveling analysis of a mining dump truck **25**

3.1 Introduction 25

3.2 Analysis model 26

3.2.1 Single-tire traveling analysis 27

3.2.2 Full vehicle model 28

3.3 Climbing analysis of vehicles with TCS 30

3.3.1 Effect of target slip ratio 31

3.3.2 Effectiveness of TCS 34

3.3.3 Effect of terrain condition . . . 36
3.4 Examination of multipass effect . . . 39
3.5 Conclusion . . . 43

4 Study on applicability of RFT to traveling analysis of wheel with grousers 45
4.1 Introduction . . . 45
4.2 Virtual plate test using DEM . . . 48
4.2.1 Analysis model . . . 48
4.2.2 Determination of scale factor ζ . . . 49
4.3 Traveling analysis of wheel with grousers . . . 51
4.3.1 Analysis model and boundary condition . . . 51
4.3.2 Comparison of results obtained by DEM and RFT . . . 53
4.4 Discussion . . . 58
4.5 Conclusion . . . 63

5 Examination of wheel shape based on terramechanics analysis 64
5.1 Introduction . . . 64
5.2 Packing effect . . . 66
5.2.1 Basic concept of packing effect . . . 66
5.2.2 DEM analysis . . . 67
5.3 Single-wheel experiment . . . 73
5.3.1 Experimental setup . . . 73
5.3.2 Experimental results . . . 76
5.4 Trafficability analysis based on terramechanics theory . . . 79
5.4.1 Analysis results and discussion . . . 79
5.4.2 Effect of equivalent radius . . . 85
5.5 Conclusion . . . 86

6 Proposal of multi-stage analysis method 89
6.1 Introduction . . . 89

6.2 Simulation of ripple formation by wind-blown sand 89
6.2.1 Model 90
6.2.2 Analysis results 91
6.3 Analysis of single wheel locomotion on wind ripples 95
6.3.1 Trafficability characteristics of flat road surface 96
6.3.2 Trafficability characteristics of wind ripples 98
6.3.3 Effects of wheel specification and traveling direction . . 102
6.3.4 Effect of scale factor distribution 109
6.4 Conclusion 112

7 Extension of semi-empirical terramechanics approach 113
7.1 Introduction 113
7.2 Terrain surface deformation and change in terramechanics parameter 114
7.2.1 Terrain surface deformation 114
7.2.2 Changes in parameters owing to the terrain surface deformation 116
7.3 Experimental apparatus 119
7.4 Plate drag analysis 122
7.5 Wheel traveling analysis 126
7.5.1 Flat terrain surface 127
7.5.2 Sinusoidal terrain surface 132
7.6 Conclusion 137

8 Summary and future work 138
8.1 Summary 138
8.2 Future work 139
8.2.1 Implementation of the proposed model to MBD analysis 139
8.2.2 Traveling analysis considering turning 140
8.2.3 Cooperation with actual machine control 140

Acknowledgement 141

References **152**

A Code for terramechanics analysis **153**

A.1 Terramechanics model 153

List of Figures

1.1 Outline of the proposed analysis method. 6
1.2 Structure of thesis. 9
2.1 Variables related to the traveling characteristics and the distribution of normal stress beneath a rigid wheel 12
2.2 Distribution of shear stress beneath a rigid wheel. 12
2.3 Substitution circle model for flexible tire. 14
2.4 Definitions of the orientation angle β, velocity vector angle γ, and stresses σ_x and σ_z: (a) Definitions when the x component of the velocity vector v is negative; (b) Definitions when the x component of the velocity vector v is positive. 15
2.5 Distributions of α_x and α_z in the (β, γ) plane obtained using Eq. (2.16), where $\zeta = 1$. 16
2.6 Application of the RFT to the wheel with grousers. The distance from the center of the wheel to the grouser surface r is in the range of $D/2 \leq r \leq D/2 + h_g$. 19
2.7 Application of the RFT to a rigid wheel, where da is the area of a small plate. The quadrangular prisms in the background of the (x, z) plane are the distribution of the cell height, which constitute the ripple pattern. 20
3.1 Single-tire model. 27
3.2 IAHV full-vehicle model. 29
3.3 Road model for climbing analysis. 29
3.4 Schematic relationship between drawbar-pull and slip ratio. . . 30
3.5 Calculation flow of TCS. 30
3.6 Relationship between slip ratio and drawbar-pull obtained using the single-tire model. 32
3.7 Relationship between slip ratio and drawbar-pull when the vertical load is changed. 33
3.8 Variations of migration length and slip ratio with the elapsed time. 33

3.9 Comparison of traveling performance with and without the TCS. 35
3.10 Variations of migration length and slip ratio with and without the TCS. 35
3.11 Relationship between slip ratio and drawbar-pull obtained with the soil conditions of Type A, Type B, and Type C. 37
3.12 Variations of migration length with the elapsed time under the conditions of Type A, Type B, and Type C. 38
3.13 Change in density and cohesion due to multipass effect. 41
3.14 Multipass effect on migration length. 42
3.15 Multipass effect on sinkage. 42
3.16 Multipass effect on vehicle pitch angle. 43
4.1 DEM Analysis model for plate tests. 48
4.2 Comparison of the vertical stress vs. sinkage relation between DEM and RFT. Here, $\beta = 0$and $\gamma = \pi/2$. The scale factor is determined as $\zeta = 0.191$ by the linear approximation. 50
4.3 Comparison of the stress vs. sinkage relation between DEM and RFT under various orientation angles and velocity vector (intrusion/extrusion) angles: (a) $\beta = 0$, $\gamma = \pi/4$; (b) $\beta = \pi/4$, $\gamma = \pi/2$; (c) $\beta = 0$, $\gamma = -\pi/4$; and (d) $\beta = \pi/4$, $\gamma = -\pi/2$. . . 51
4.4 DEM analysis model for the single wheel traveling test. The ground condition is the same as the model shown in Fig. 4.1. . 53
4.5 Variation of drawbar-pull with elapsed time under each slippage, where the wheel A is used for calculations: (a) DEM; and (b) RFT. The coefficient of traction is computed by dividing the drawbar-pull by the constant wheel load. 55
4.6 Variation of drawbar-pull with elapsed time under each slippage, where the wheel B is used for calculations: (a) DEM; and (b) RFT. The coefficient of traction is computed by dividing the drawbar-pull by the constant wheel load. 56

4.7 Variation of drawbar-pull with elapsed time under each slippage, where the wheel C is used for calculations: (a) DEM; and (b) RFT. The coefficient of traction is computed by dividing the drawbar-pull by the constant wheel load. 56
4.8 Stress distribution on wheel A. The red lines indicates stress generated in the horizontal direction, while the blue lines indicates stress generated in the vertical direction. 57
4.9 The relationship between average coefficient of traction in steady state and slippage: (a) DEM; and (b) RFT. 57
4.10 Snapshots of the wheel-soil interaction in the DEM analysis, where the wheel B is used and the slippage is 0.5. The colors in the contour map represent the magnitude of particle velocity. 60
4.11 Schematic diagram of analysis condition for plate rotation test and variation of resistive force in the horizontal direction and vertical direction with elapsed time: (a) condition of single plate rotation; (b) condition of two plates rotation; (c) results of single plate rotation; and (d) results of two plates rotation. 61
4.12 Schematic diagram of analysis condition for bulldozing test of lidded plates and variation of resistive force in the horizontal direction with elapsed time: (a) condition of bulldozing test; and (b) results of DEM and RFT analyses. 62
5.1 Schematic of driving force of grouser wheels: (a) rectangular and (b) trapezoidal grousers. 67
5.2 DEM analysis model corresponding to one period of the grousers. 69
5.3 Variation in the vertical reaction force and volume fraction with the vertical displacement. 72
5.4 Variation in the vertical reaction force with intrusion volume. . 72
5.5 Experimental setup of single-wheel traveling apparatus. In the experiment, the translation and angular velocities were controlled under constant wheel load. 74
5.6 Grouser wheels utilized in this study. 75

5.7 Variations in drawbar-pull and sinkage with traveling distance for wheels with 12 grousers (Rectangle A and Trapezoid A): (a) Drawbar-pull, (b) Sinkage. 77
5.8 Variations in drawbar-pull and sinkage with traveling distance for wheels with 18 grousers (Rectangle B and Trapezoid B): (a) Drawbar-pull, (b) Sinkage. 78
5.9 Terrain surface after the passage of a wheel. 78
5.10 Relationship between traveling performance and slippage obtained through experiment: (a) Coefficient of traction, (b) Sinkage. Each plot is evaluated by the average value of steady rolling state. 79
5.11 Variation of drawbar-pull with traveling distance under different slippage conditions:(a)$N_g = 12$,(b)$N_g = 18$. 82
5.12 Relationship between coefficient of traction and slippage obtained through RFT analysis. 83
5.13 Relationship between coefficient of traction and slippage as the scale factor is changed. 83
5.14 Trajectories of α_x during traveling on stiffness distribution map shown in Fig. 5.11 ($s = 0.1$). 84
5.15 Trajectories of α_x during traveling on stiffness distribution map shown in Fig. 5.11 ($s = 0.5$). 84
5.16 Relationship between coefficient of traction and slippage, as a function of the grouser height and wheel diameter, for (a) Wheel A and (b) Wheel B. 86
6.1 Variation of soil surface geometry with number of repetition steps k, where the condition C in Table 6.1 was adopted. The directions of row i and column j correspond to the x and y coordinates, respectively. The unit of each axis is in m. 93
6.2 Wind ripple patterns under conditions A - E in steady state ($k = 30000$). The unit of each axis is in m. 94

6.3 Relationship between drawbar-pull and slip ratio, where $R =$ 100 mm, $B = 100$ mm, and $W = 120$ N. 96
6.4 Terramechanics analysis results for a flat road surface: (a) trajectory of the wheel center; (b) variation of the slip ratio (dashed line) and the x-coordinate of the wheel centre (solid line) with the elapsed time. 97
6.5 Terramechanics analysis results for Ground C: (a) trajectory of the wheel center; (b) variation of the slip ratio (dashed line) and the x-coordinate of the wheel centre (solid line) with the elapsed time. 99
6.6 Stress distribution on the wheel surface for field C: (a) $t = t_1$; (b) $t = t_2$. 100
6.7 Terramechanics analysis results for field A, B, D, and E: (a) variation of the slip ratio with the elapsed time; (b) variation of the x-coordinate of the wheel center with the elapsed time; (c) trajectory of the wheel center for field B. 101
6.8 Trajectory of the wheel center for field C while varying the wheel radius. 104
6.9 Terramechanics analysis results for field C while varying the wheel radius: (a) variation of the slip ratio with the elapsed time; (b) variation of the x-coordinate of the wheel center with the elapsed time. 105
6.10 Terramechanics analysis results for field C while varying the wheel load: (a) variation of the slip ratio with the elapsed time; (b) variation of the x-coordinate of the wheel center with the elapsed time. 106
6.11 Trajectory of the wheel centre for field C while varying the transverse angle. 107

6.12 Terramechanics analysis results for field C while varying the transverse angle: (a) variation of the slip ratio with the elapsed time; (b) variation of the x-coordinate of the wheel center with the elapsed time. 108
6.13 Terramechanics analysis results for Ground C, as the scale factor is varied: (a) variation in the slip ratio; (b) variation in the x-coordinate; (c) histogram of the scale factor; (d) scale factor distribution. 110
6.14 erramechanics analysis results for Ground C with a scale factor distribution that depends on the terrain surface height: (a) variation in the slip ratio; (b) variation in the x-coordinate; (c) scale factor distribution. 111
7.1 Terramechanics analysis flow considering the terrain surface deformation. 117
7.2 Schematic of moving action. 118
7.3 Schematic of rolling action. 119
7.4 Experimental setup of single-wheel traveling apparatus. The translation and angular velocities were controlled under a constant wheel load. 121
7.5 Rake to create a terrain surface with a sinusoidal shape. . . . 122
7.6 Variations in the resistive force with the elapsed time. 124
7.7 Terrain surface shape and stress distribution generated on the plate, obtained in the simulation based on the proposed model: (a) Terrain surface shape after passage through the plate; (b) Stress distribution. 125
7.8 Terrain surface shape after the plate drag test. 125
7.9 Variations in the (a) drawbar-pull and (b) sinkage with the traveling distance, as obtained experimentally. The results correspond to seven levels of the slip ratio s. 129
7.10 Variations in the (a) drawbar-pull and (b) sinkage with the elapsed time, as obtained using the proposed model. 129

7.11 Relationship between the steady-state traveling characteristics and slip ratio: (a) drawbar-pull; (b) sinkage. 130
7.12 Residual deformation of the terrain surface and stress distribution on the wheel surface in the steady state: (a)s=0.3; (b)s=0.7. The black line in the figure shows the trajectory of the wheel center. 131
7.13 Determination of θ_f and θ_r in the proposed model for uneven terrain surface: (a) Descending; (b) Ascending. 134
7.14 Variations in a)drawbar-pull and (b) vertical displacement with the elapsed time on the sinusoidal surface. 135
7.15 Terrain surface deformation after traveling on sinusoidal surface and stress distribution on the wheel surface: (a)$t = t_1$; (b)$t = t_2$. The black line indicates the trajectory of the wheel center. 136

List of Tables

2.1 Fourier coefficients for RFT calculation [1]. 16
3.1 Specifications of the IAHV 26
3.2 Tire specifications (Michelin 59/80R63 XDR2). 27
3.3 Parameters of the terramechanics model. 32
3.4 Analysis parameters for Type A, Type B, and Type C. 37
4.1 Analysis condition of DEM model. 49
4.2 Specifications of wheels. 53
5.1 Particle size distribution of DEM analysis model 70
5.2 Parameters for DEM analysis. 71
5.3 Specifications of sensors. 75
5.4 Specifications of wheels. 76
5.5 Wheel specifications (Wheel A). 85
5.6 Wheel specifications (Wheel B). 86
6.1 Simulation conditions of wind ripple formation. The angle of repose is 30 deg. 92
7.1 Specifications of sensors. 121
7.2 Analysis parameters for the cellular automata 124
7.3 Specifications of the rigid wheel. 126
7.4 Analysis parameters of BWR model used for stress evaluation. 127

1 Introduction

1.1 Background

Terramechanics is an interdisciplinary field that pertains to the interaction between the ground and vehicles [2–5]. The target of terramechanics includes all off-road vehicles such as automobiles, construction machinery, agricultural machinery, and military vehicles. Recently, terramechanics has attracted renewed attention and is being applied for solving problems in extreme environments, e.g., the use of disaster response robots and lunar/planetary exploration rovers [6–11]. Typical characteristics of terramechanics are as follows:

1). Underbody design to efficiently travel through soft ground, such as sand/mud/ice/snow, without "getting stuck";

2). Sophistication of control methods and formulation of pass plans for unmanned and autonomous traveling;

3). Operator training and remote control support using a dynamics simulator;

4). Preliminary verification of respective work processes and rescue work at construction and disaster sites by computerized construction (known as i-Construction).

To performed the examination above, multibody dynamics analysis [6, 7, 12–14], which introduces a terramechanics model for the interaction between the terrain surface and machine, can be an effective method. Multibody dynamics analysis can be an effective method for various rough terrains for not only improving the performance of off-road vehicles and robots, but also for improving the efficiency of various tasks and creating safe working plans. To date, work process simulations of construction machinery [15], planetary exploration rover [6,12], and disaster response robots [7] have been performed.

However, the following two problems must be overcome in conventional terramechanics simulations.

1.1.1 Technical issues in terrain surface modeling

The first issue is terrain surface modeling. The target terrain field must be prepared before performing terramechanics analysis; however, methods to create such terrain fields have not been investigated extensively. Although the terrain fields in conventional terramechanics analysis are prepared based on various assumptions and experiences, most of them have homogeneous and flat surface conditions. Furthermore, off-road conditions may have different geometries and soil properties depending on the formation process, which should be reflected appropriately in terrain field simulations.

In this regard, sensing data may be used to create realistic terrain fields. For example, high-precision topographic data can be obtained via aerial laser scanning, such as LiDAR , and a point cloud of the topographic surface layer can be obtained by ortho mapping using satellite images or images captured by drones. A terrain field for terramechanics analysis can be created using a point cloud. In addition, the mechanical properties of soil in the target field can be determined by performing the Bevameter test or various penetration tests.

Meanwhile, many numerical simulations related to the formation process of terrains have been conducted, e.g., the formation of wind ripples in a desert [16–18], washboarding of dirt roads due to repeated traffic [19, 20], and soil compaction by rollers in construction work [21, 22]. Furthermore, in terms of disaster, numerical simulations for slope failure, landslides, and avalanches have been reported [23–31]. Therefore, if terrain fields can be created for terramechanics analysis using the results of these sensing techniques and terrain formation simulations, they can be used for the trafficability evaluation of the terrain and path planning in various situations.

In Hokkaido, the Iburi eastern earthquake that occurred in 2018 involved 41 victims, of which 36 were involved in the landslide [32, 33]. Construction

machineries are often used for restoration work, and prior verification of their traveling characteristics is indispensable to determine whether they can enter safely. Meanwhile, the evaluation of terrain surface characteristics is indispensable for lunar and planetary exploration. For instance, the Spirit, one of the Mars exploration rovers of the NASA , has been getting stuck on soft ground [34].The surface of Mars is covered with fine sand, known as regolith, and wind ripple patterns are formed by wind generated on Mars. These complicated terrain surfaces cause complicate the traversal of exploration rovers [12]. Hence, virtual field modeling for terramechanics simulation by terrain surface measurement and numerical analysis are important for terrain surfaces with complicated shapes and properties, such as disaster sites and outer space.

1.1.2 Technical issues of terramechanics model

The other issue is the terramechanics model used in the simulation. The interaction between soil and machine can be evaluated using terramechanics models, such as the Wong and Reece model (based on Bekker' s work) [2]. This type of semi-empirical approach can be applied to the behavior analysis of an entire vehicle at a relatively low cost [6,11,35]. Furthermore, although a rover' s wheels are typically accompanied by grousers or lugs for improving traveling performance, this semi-empirical approach is applicable to such cases. However, the calculable shapes are restricted, and problems such as incompatibility to arbitrary traveling parts remain.

Meanwhile, resistive force theory (RFT) has been proposed to empirically estimate the reaction force of a rigid body moving inside a loose granular medium. Although RFT was originally developed for viscous drag problems, it has received renewed attention in recent years as a method that can easily reflect the interaction between a granular medium and a traveling part with arbitrary shapes (including parts such as legs interacting with soil) [1,36–38]. RFT has been applied to multibody dynamics analysis for legged mobile robots [1, 36] and wheel traveling analysis [38]; additionally, its applicability

to terramechanics problems has been investigated. Furthermore, Slonaker et al. (2017) [38] utilized the intrusion force evaluated using RFT to derive general scaling relations for locomotion in granular media. It is noteworthy that Askari and Kamrin (2016) [37] have provided the physical reasons enabling granular media having complex behaviors locally to be expressed via RFT. According to them, RFT may be applicable to cohesive media unless a target soil is a velocity-dependent viscous medium. In addition, they organized a new family of resistive-force-obeying materials and demonstrated the good prediction accuracy of the RFT for loose granular media.

The terramechanics model proposed based on the semi-empirical method above can be introduced into multibody dynamics and used for the design of the underbody. However, this terramechanics model does not consider surface deformation due to interactions. The conventional terramechanics model allows the penetration of an object into the terrain surface, and the magnitude of stress is evaluated based on intrusion; however, in reality, when an object penetrates the terrain surface, a certain deformation occurs on the terrain surface. In the Wong - Reece model, although the terrain surface change behind the wheels is expressed in a simple form, only the compression deformation of the terrain surface is considered. Terrain surface deformation due to wheels pushing the terrain surface forward or backward is not considered. It is noteworthy that DEM analysis [39–45] and FEM analysis [39, 46–50] can be performed to consider the deformation of the terrain surface in detail. However, these methods incur a high calculation cost and are difficult to introduce into multibody dynamics. Hence, a model that has a low comparative calculation cost and can appropriately expresses terrain surface deformation is desired.

1.2 Purpose and Approach

The purpose of this study is to improve the conventional terramechanics analysis method and perform terramechanics simulation for terrain with complicated shapes and properties. The outline of the terramechanics analysis

method proposed herein is shown in Fig. 1.1.

The terrain surface information used in the analysis method was inherited from other analysis and measurement techniques. Terrain surface information was captured based on terrain surface deformation analysis obtained using the FEM and cellular automaton as well as measurement technology obtained using three-dimensional cameras and LiDAR. Depending on the method, not only the topology of the field, but also the soil properties and loading history of the terrain surface can be inherited.

Subsequently, the forces generated in the vehicle underbody were evaluated using the obtained field model. Typical terramechanics models, such as the BWR and RFT, were used for force evaluation. The deformation and changes in properties of the terrain surface due to the interaction between the ground and machine were evaluated based on the mechanism proposed by the authors.

Using the obtained forces, the motion dynamics of the target machine were evaluated. Hence, the traveling performance, known as trafficability, typified by vehicle undercarriage slip and drawbar-pull characteristics, can be confirmed. Specifically, after the vehicle position was updated, the interaction with the terrain surface was re-evaluated, and the movement of the vehicle was evaluated sequentially.

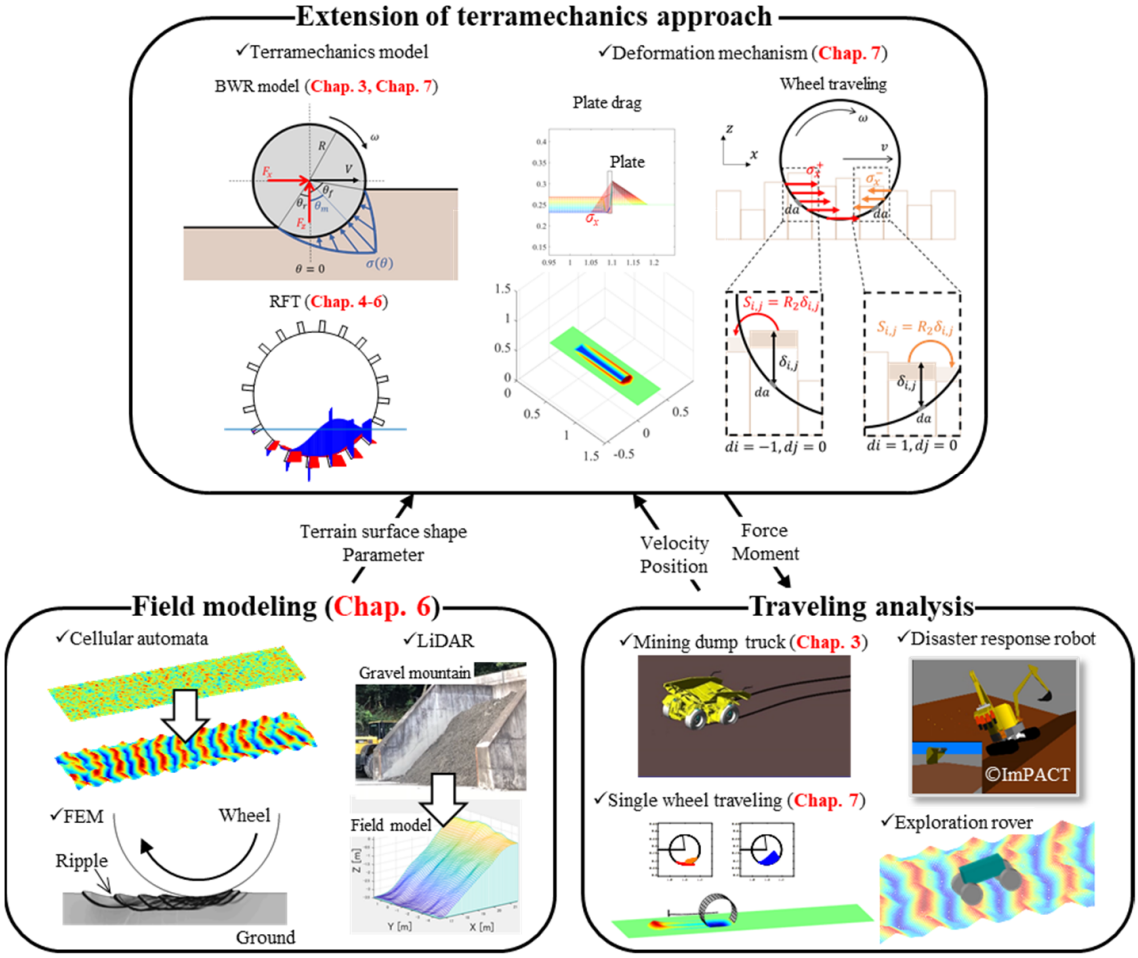

Figure 1.1: Outline of the proposed analysis method.

1.3 Organization of thesis

This thesis comprises eight chapters. The organization of the thesis is shown in Fig. 1.2.

Chapter 2 describes the terramechanics model used for the analysis. Herein, two typical terramechanics models, i.e., the BWR model and the RFT, are introduced.

In Chapter 3, the traveling analysis of a dump truck for mining is presented as an example of multibody dynamics analysis using a terramechanics model. The BWR model is introduced for the interaction between the tire and ground, and the trafficability of the vehicle on soft terrain is verified. Furthermore, a control method known as the traction control system (TCS) implemented in an actual machine is analyzed based on simulation. In this chapter, the effect TCS control on trafficability and its optimization is analyzed.

In Chapter 4, the traveling analysis of wheels with grousers is presented based on RFT. RFT, which is a relatively new theory of terramechanics, is receiving attention as a method for simulating objects with complex shapes and movements. However, the applicability of RFT to wheel traveling phenomena must be further investigated. In this chapter, the applicability of RFT is analyzed via the simulation of wheels with grousers using the DEM and RFT and then comparing both results.

In Chapter 5, the grouser shape for wheels is proposed based on simulation using RFT. Because RFT can be applied to objects with arbitrary shapes, it can be useful for studying wheel shapes. In this chapter, an RFT-based terramechanics simulation that was performed while complementarily utilizing DEM analysis and model experiments is presented. Furthermore, based on the results, a wheel shape for the lunar/planetary exploration rover is proposed.

In Chapter 6, a multistage analysis method is proposed that inherits terrain surface information obtained from other simulation and measurement techniques to a field model for terramechanics simulation. First, the outline of the multistage analysis method is described. Subsequently, as a typical example of the terrain surface formation simulation, a generation of wind ripple pattern based on a cellular automaton performed as the first step in the simulation is presented; subsequently, a single-wheel traveling simulation that inherits the terrain surface information obtained by the first step in the simulation is presented.

In Chapter 7, an extended terramechanics model for introducing terrain surface deformation and property changes associated with the interaction between the ground and machine is proposed. The proposed method is validated by comparing the results obtained from the plate drag and wheel traveling analyses with the results of model experiments.

Chapter 8 summarizes the results of the study as well as future prospects.

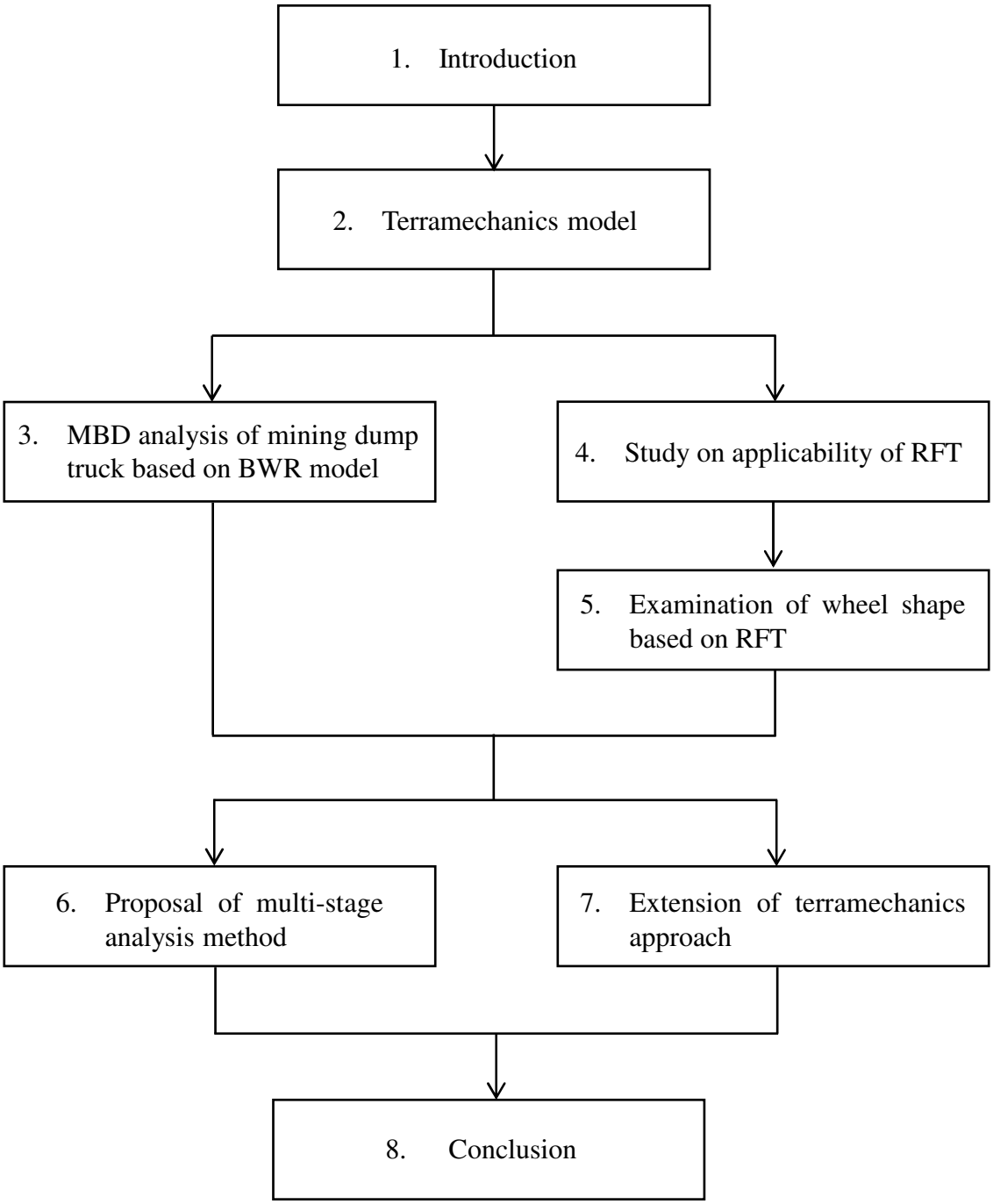

Figure 1.2: Structure of thesis.

2 Terramechanics models

2.1 Introduction

This chapter describes the terramechanics model used for simulation. In this study, the Bekker–Wong–Reece (BWR) model and the Resistive Force Theory (RFT) are used to evaluate the mechanical properties of objects moving on a rough terrain. The outline of the BWR model for rigid wheels and elastic wheels will be provided. Furthermore, the outline and application range of the RFT will be provided. Moreover, a method to apply the RFT to objects and terrain surfaces with complex shapes is described.

2.2 Bekker–Wong–Reece (BWR) model

2.2.1 Rigid wheels

The BWR model is a classical terramechanics model that has been used to evaluate the traveling characteristics of off-road vehicles [3, 35]. The normal stress $\sigma(\theta)$ changes according to the contact angle θ and is expressed by Eq. (2.1).

$$\sigma(\theta) = \left(ck_c^{'} + \rho g l k_{\varphi}^{'}\right)\left(\frac{h(\theta)}{l}\right)^n \tag{2.1}$$

where c is the adhesive stress [Pa], $k_c^{'}$ and $k_{\phi}^{'}$ are the soil constants [-], ρ is the soil density [kg/m^3], and l is the wheel contact length [m]. The stress distribution on the wheel surface is expressed by $h(\theta)$ in Eq. (2.1)

$$\begin{cases} h(\theta) = R(\cos\theta - \cos\theta_f) & (\theta_m \leq \theta \leq \theta_f) \\ h(\theta) = R\left[\cos\left\{\theta_f - \frac{\theta-\theta_r}{\theta_m-\theta_r}(\theta_f - \theta_m)\right\} - \cos\theta_f\right] & (\theta_r \leq \theta < \theta_m) \end{cases} \tag{2.2}$$

Here, R is the wheel radius. Furthermore, θ_f and θ_r are the entry and exit angles, respectively, which are calculated from the positional relationship between the wheels and the terrain surface. Moreover, θ_m represents the angle at which the normal stress $\sigma(\theta)$ becomes maximum, and it is expressed

as follows:

$$\theta_m = (a_0 + a_1 s)\,\theta_f \tag{2.3}$$

Here, a_0 and a_1 are called the maximum stress angle constants and they depend on the ground property. Furthermore, s is the slip ratio, which is defined as follows:

$$s = 1 - \frac{v}{R\omega} \tag{2.4}$$

Here, ω is the angular velocity of the wheel, and v is the translational velocity. The shear stress τ generated in the tangential direction of the wheel is expressed by the following equation using the shear strength of the soil (adhesive stress c and internal friction angle ϕ) and the relative slip displacement j_x between the wheel and the soil.

$$\tau\,(\theta) = (c + \sigma \tan\varphi)\left(1 - \exp^{-j_x/k_x}\right) \tag{2.5}$$

Here, j_x is the value obtained by integrating the relative slip velocity v_{sx} of the wheel surface over time and is expressed by the following equation:

$$\begin{aligned} j_x\,(\theta) &= \int_0^t v_{sx} dt \\ &= \int_{-\theta_r}^{\theta_f} [r\omega\,\{1 - (1-s)\cos\theta\}]\frac{1}{\omega} d\theta \\ &= r\,[\theta_f - \theta - (1-s)\,(\sin\theta_f - \sin\theta)] \end{aligned} \tag{2.6}$$

The drawbar-pull F_x is obtained by integrating the x-direction (traveling direction) components of the normal stress σ and shear stress τ acting on the wheel over the ground contact region. That is,

$$F_x = rb \int_{-\theta_r}^{\theta_f} \Big[\tau(\theta)\cos\theta - \sigma(\theta)\sin\theta\Big]\, d\theta. \tag{2.7}$$

The vertical reaction force F_z received by the wheel from the ground is calculated using the following equation by integrating the z-direction components of normal stress σ and shear stress τ over the ground contact region:

$$F_z = rb \int_{-\theta_r}^{\theta_f} \Big[\tau(\theta)\sin\theta + \sigma(\theta)\cos\theta\Big]\, d\theta \tag{2.8}$$

The drive torque T_y and traveling efficiency η can be evaluated using the following equations, respectively:

$$T_y = r^2 b \int_{-\theta_r}^{\theta_f} \Big[\tau(\theta)\Big] d\theta \tag{2.9}$$

$$\eta = \frac{F_x(1-s)r}{T_y} \tag{2.10}$$

Here, the running efficiency indicates the efficiency at which the driving torque is converted into drawbar-pull [51].

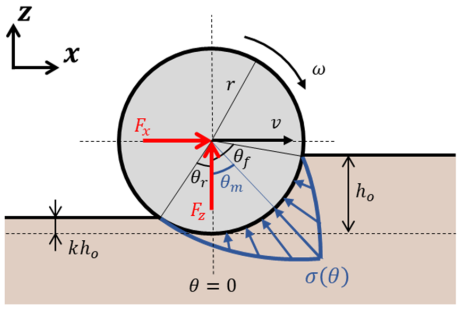

Figure 2.1: Variables related to the traveling characteristics and the distribution of normal stress beneath a rigid wheel

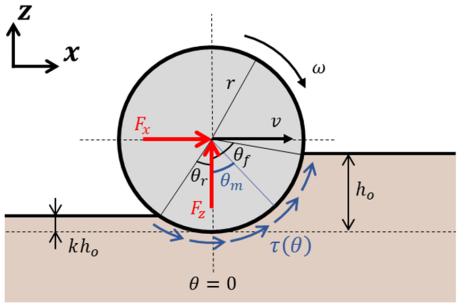

Figure 2.2: Distribution of shear stress beneath a rigid wheel.

2.2.2 Elastic wheel

This section outlines the traveling dynamics considering the flexibility of a tire based on the substitution circle theory [52]. Fig. 2.3 shows a schematic diagram of a flexible tire model.

When a flexible tire travels, it becomes deformed due to the contact pressure from the ground. As shown in Fig. 2.3, the deformation of the flexible tire during traveling can be approximated as a rigid wheel having a larger radius of curvature than that of the wheel before deformation. The circle that depicts the deformed surface of the tire is called a substitution circle.

As shown in Fig. 2.3, the sinkage under the center of the flexible tire is ${h_o}^*$, and the sinkage under the tire before deformation is h_o. ${h_o}^*$ can be expressed by the following equation:

$$ {h_o}^* = h_o - \delta \tag{2.11} $$

Here, δ is the amount of tire deflection, and its relationship with the weight M in the vertical direction is approximated by the polynomial of the following equation:

$$ \delta = T_1 M^3 + T_2 M^2 + T_3 M \tag{2.12} $$

T_1, T_2, and T_3 are the flexible tire coefficients measured through experiments, and these values can express the degree of tire deformation. By setting T_1, T_2, and T_3 to 0, a rigid wheel without deformation can also be described.

The radius r^* of the substitution circle is derived from the following approximate expression:

$$ \sqrt{\frac{r^*}{r}} \approx \sqrt{1 + \frac{\delta}{{h_o}^*}} + \sqrt{\frac{\delta}{{h_o}^*}} \tag{2.13} $$

For Eq. (2.13), r^* is evaluated through the following equation using the tire radius r before deformation, tire deflection amount δ, and sinkage ${h_o}^*$:

$$ r^* = r \left(1 + 2\frac{\delta}{{h_o}^*} + 2\sqrt{1 + \frac{\delta}{{h_o}^*}} \sqrt{\frac{\delta}{{h_o}^*}} \right) \tag{2.14} $$

The vertical load and traction force of a flexible tire can be obtained in a similar manner as that for a rigid tire by evaluating the stress distribution using r^* and ${h_o}^*$.

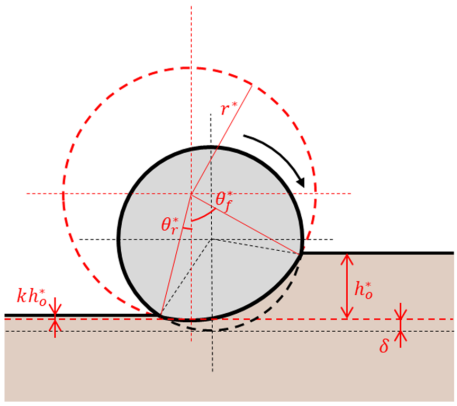

Figure 2.3: Substitution circle model for flexible tire.

2.3 Resistive Force Theory (RFT)

2.3.1 Overview of RFT

The RFT is a relatively new terramechanics model proposed by Li et al., in 2013 [1]. Although it is difficult to consider the movement and shearing of soil, the RFT can be employed to evaluate the resistive force generated in an object with an arbitrary shape and movement at a low calculation cost.

According to the RFT, the stress σ on an object (small plate) is proportional to the sinkage z and can be defined as follows:

$$\begin{aligned} \sigma_x &= \alpha_x(\beta, \gamma)\,|z| \\ \sigma_z &= \alpha_z(\beta, \gamma)\,|z| \end{aligned} \tag{2.15}$$

where the subscripts x and z represent the coordinate axes, as shown in Fig. 2.4. The stiffness α of the granular media depends on the orientation angle β of the plate and the velocity vector angle (intrusion/extrusion angle) γ. The

relationship among β, γ, and α can be obtained from the plate intrusion/extrusion test of the target granular media [1]. Note that the definitions of β, γ, and σ_x vary depending on whether the x component of the velocity vector is positive or negative, as shown in Fig. 2.4. The distributions of α can be expressed as follows:

$$\alpha_z(\beta,\gamma) = \zeta \sum_{m=-1}^{1}\sum_{n=0}^{1}\left[A_{m,n}\cos 2\pi\left(\frac{m\beta}{\pi}+\frac{n\gamma}{2\pi}\right)+B_{m,n}\sin 2\pi\left(\frac{m\beta}{\pi}+\frac{n\gamma}{2\pi}\right)\right]$$
$$\alpha_x(\beta,\gamma) = \zeta \sum_{m=-1}^{1}\sum_{n=0}^{1}\left[C_{m,n}\cos 2\pi\left(\frac{m\beta}{\pi}+\frac{n\gamma}{2\pi}\right)+D_{m,n}\sin 2\pi\left(\frac{m\beta}{\pi}+\frac{n\gamma}{2\pi}\right)\right] \quad (2.16)$$

where the coefficients A, B, C, and D are obtained via Fourier transformation. The values of the Fourier coefficients used in this study were obtained from the study by Li et al., (2013), as listed in Table 2.1. ζ is the scale factor, which is used to express the stiffness of the granular media. The scale factor is a constant that depends on the granular media, and it can be obtained from the following equation:

$$\zeta \approx \alpha_z\left(0,\frac{\pi}{2}\right) \quad (2.17)$$

Eq. (2.17) corresponds to the vertical intrusion test when the plate orientation is horizontal.

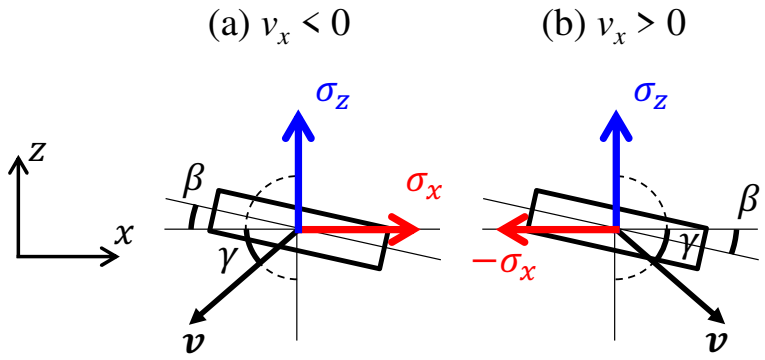

Figure 2.4: Definitions of the orientation angle β, velocity vector angle γ, and stresses σ_x and σ_z: (a) Definitions when the x component of the velocity vector v is negative; (b) Definitions when the x component of the velocity vector v is positive.

Table 2.1: Fourier coefficients for RFT calculation [1].

$A_{0,0}$	0.206
$A_{1,0}$	0.169
$B_{1,1}$	0.212
$B_{0,1}$	0.358
$B_{-1,1}$	0.055
$C_{1,1}$	-0.124
$C_{0,1}$	0.253
$C_{-1,1}$	0.007
$D_{1,0}$	0.088

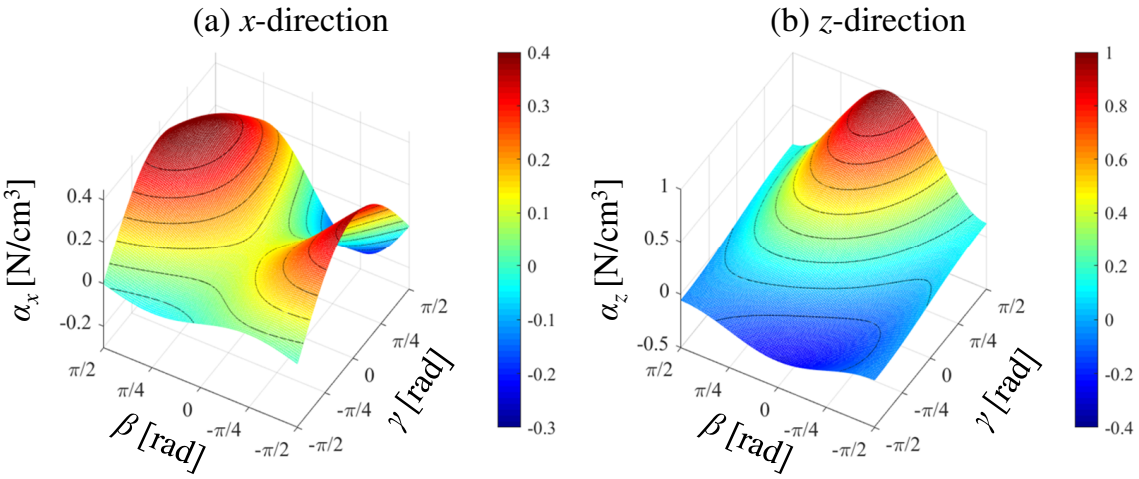

Figure 2.5: Distributions of α_x and α_z in the (β, γ) plane obtained using Eq. (2.16), where $\zeta = 1$.

2.3.2 Application method of RFT

The method of applying the RFT to terramechanics analysis can be summarized as follows:

1) The object is discretized into small sections, and the values of β and γ for each part during forced-slip traveling are calculated. Specifically, each part has an angular velocity ω and a translational velocity V as shown in Fig. 2.6. Thus, γ is obtained from these combined velocity vectors, and β can be obtained considering the inclination of each section.

2) The resistive force of each section on the wheel surface can be calculated by substituting β and γ into Eq. (2.16).

3) The horizontal and vertical forces are calculated by performing an area integration of the resistive force of the small piece-wise sections.

Eq. (2.16) presents a low-cost calculation of the RFT, and it can be applied to an object with an arbitrary shape and movement; its constants are derived based on the result of the plate intrusion/extrusion test. Therefore, applying the RFT to a closed shape, such as a wheel, requires ingenuity. For instance, a negative vertical stress calculated on the wheel parts (extrusion case) corresponds to the force acting on the inside of the wheel. However, this situation is different from the actual phenomenon because there is no granular medium inside a closed-shaped wheel. Therefore, in this study, we assumed that no stress is generated on the wheel surface (rear area in the traveling direction) where the vertical stress becomes negative. In addition, the distribution maps of α_x and α_z correspond to the range $-\pi/2 \leq \beta \leq \pi/2$, $-\pi/2 \leq \gamma \leq \pi/2$ and the definitions in Fig. 2.4(a). Therefore, when the velocity vector γ in the calculation points in the positive direction of the x-axis, the calculation method needs to be changed to apply the RFT within the range of the distribution map. In this study, when the horizontal component of the velocity vector was inverted, as shown in Fig. 2.4(b), the reference plane defining β and γ was also reversed. Thus, the sign of the resistive force calculated using the RFT in the horizontal direction was also reversed.

In this study, a 3D terrain field was discretely modeled using a quadrangular prism corresponding to the cell size (dx, dy) of the 3D terrain surface,

as shown in Fig. 2.7. Notably, it is necessary to calculate the height difference between the ground surface and each plate, which constitute the wheel surface, to evaluate the sinkage in the RFT. Therefore, in this study, the quadrangular column to which the center coordinate (x, y) of the small plate belongs was determined; then, the sinkage was evaluated using the height of the target quadrangular column.

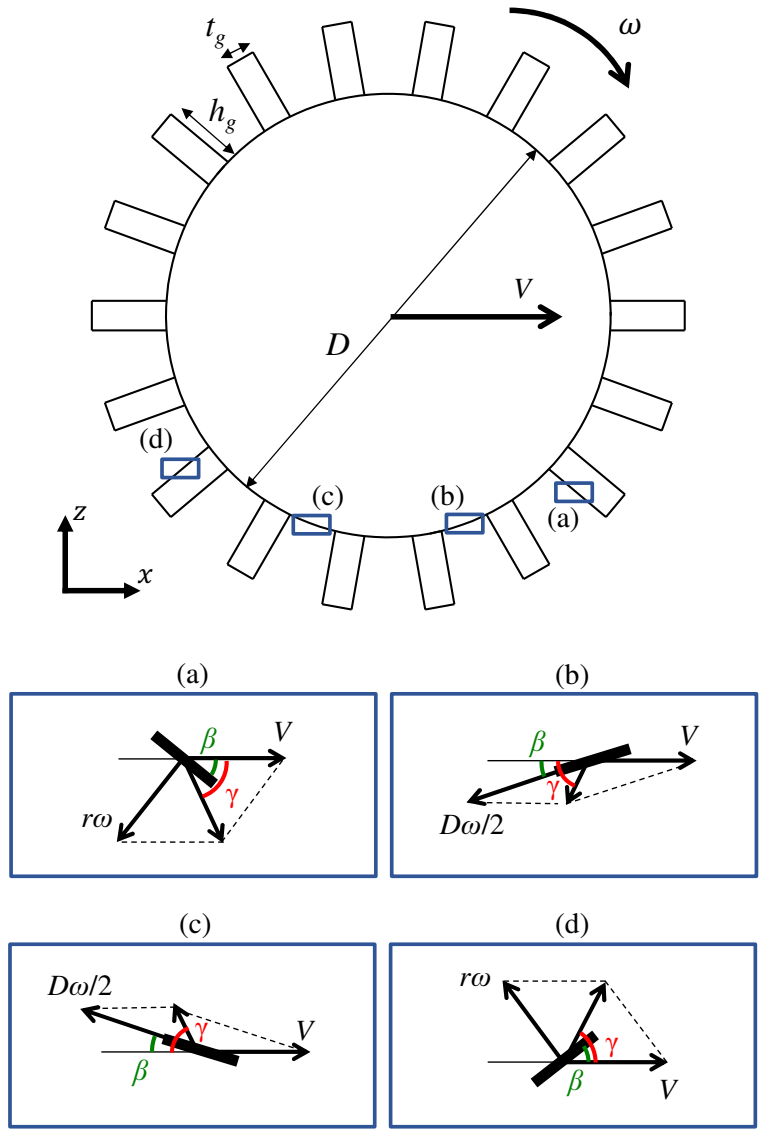

Figure 2.6: Application of the RFT to the wheel with grousers. The distance from the center of the wheel to the grouser surface r is in the range of $D/2 \leq r \leq D/2 + h_g$.

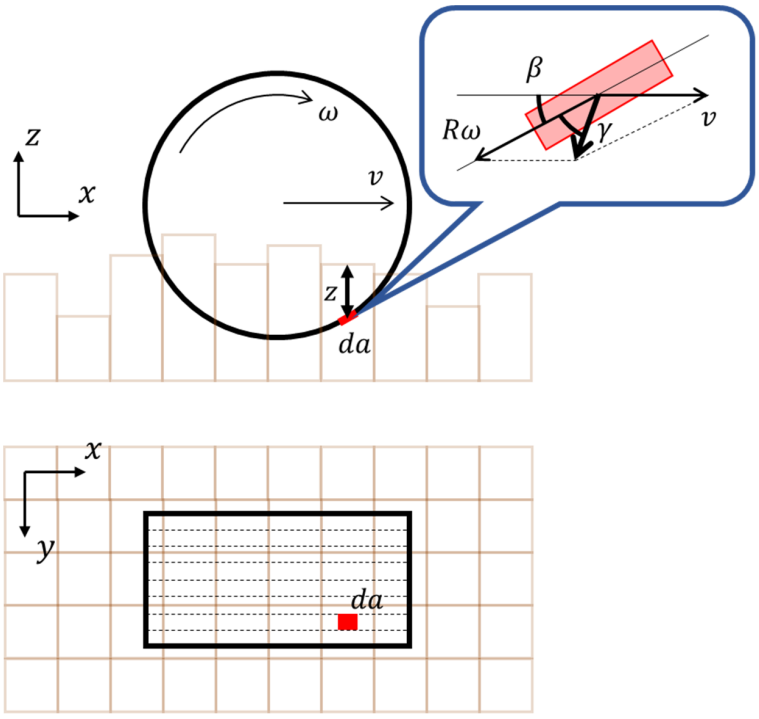

Figure 2.7: Application of the RFT to a rigid wheel, where da is the area of a small plate. The quadrangular prisms in the background of the (x, z) plane are the distribution of the cell height, which constitute the ripple pattern.

2.4 Review of terramechanics models

This section reviews the current terramechanics model. The advantages and disadvantages of each terramechanics model and the future issues are described.

2.4.1 BWR model

First, the BWR model, which is a classical terramechanics model, well expresses the stress distribution in tires without grousers, particularly large off-road vehicle undercarriages, such as dump trucks and wheel loaders. By

adjusting parameters such as a_0 and a_1, the outline of the normal stress distribution can be provided, similar to the actual phenomenon. In addition, the shear stress τ acting in the tangential direction of the wheel is based on the Coulomb's failure criterion, as shown in Eq. (2.5). This model well expresses the driving force exerted by the wheel traveling on soft ground in the steady state.

On the other hand, previous studies have indicated that the stress distribution evaluated for lightweight and small wheels is inaccurate [52], and attempts are being made to measure the stress distribution and improve the terramechanics model [53–55]. Furthermore, the scope of application needs to be studied, as it is difficult to apply this model to wheels with complicated shapes, such as those with grousers.

2.4.2 RFT

While the BWR model requires several parameters for analysis, the RFT can evaluate the motion characteristics of an object with an arbitrary shape and movement using a single parameter called a scale factor ζ. It is apparent that the parameter estimation for analysis is simple, but the scale factor ζ must be determined appropriately . Li et al. conducted a vertical penetration test of a plate to obtain the scale factor ζ [1]. In the test by Li et al., a 3.81 cm $\times$ 2.54 cm plate was penetrated. However, the plate must be sufficiently large compared with the particles to obtain the macro-mechanical interaction between the target granular material and the object. Furthermore, the material of the plate needs particular consideration. The resistive force is greatly influenced by the surface texture of the plate. Therefore, as in the study by Li et al., it is ideal that the friction coefficient of the plate is close to that of the object to be analyzed [1].

Errors may also occur in the analysis using the scale factor ζ obtained using the plate penetration test. In Li's study, the movement of a C-type leg-moving robot was performed. However, an error was confirmed in the resistance obtained via analysis and experiment. Moreover, it was indicated

that further parameter fitting was necessary [1]. For a more accurate simulation, the author believes that a scale factor more suitable for analysis needs to be obtained by using optimization methods, such as Bayesian estimation and the Levenberg–Marquardt method.

In addition, when targeting complex shapes, such as wheels with grousers, an appropriate evaluation with the RFT may be difficult, although it is possible to perform analysis. In the RFT, the relationship among the orientation angle β, velocity vector angle γ, and stress per unit depth α obtained using a plate intrusion/extrusion test is used to evaluate the stress generated in an object. However, depending on the shape to be analyzed, the grousers interfere with each other to affect the behavior of the sand, and the RFT, which evaluates the stress distribution assuming the superposition of the mechanical behavior of the plates, may not be able to handle it. The interference is likely to occur in cases where sand enters the recessed part of the object. In Chapter 5, the shape of the grouser is examined so that the sand between the grousers is strongly compressed by this interference. However, it is difficult to evaluate traveling phenomena including such a phenomenon accurately using the RFT. The target shape should be considered to obtain accurate mechanical properties using the RFT.

In addition, the motion conditions of the target object should be considered. The RFT is formulated based on the dynamics of collisions with fluids and highly fluid granular media that form craters during collisions [56, 57]. Although there is no velocity dependence in the normal RFT, the resistive force term proportional to the square of velocity cannot be ignored at a high velocity [56–58]. The plate penetration test conducted by Li et al. was performed at a penetration velocity (1 cm / s or lower) so low that the velocity term was negligible. When using the RFT described in this chapter, the velocity of the analysis target needs to be sufficiently low as in the penetration test by Li et al. The property of the target granular bed should also be considered. Granular beds that are significantly different from those considered in the formulation, such as strongly compacted sandy soils and cohesive soils

with low fluidity, should be avoided.

Nevertheless, the only terramechanics model that can currently evaluate qualitative mechanical properties for arbitrary shapes and movements is the RFT. If used properly, it can be said to be an effective terramechanics model for examining the specifications and work efficiency of machines, such as wheels.

2.4.3 Challenges and future prospects of terramechanics models

It is believed that wheels in motion exert a driving force generated by the complex combination of the wheel surface–sand slip and the sand–sand slip. This phenomenon can also be confirmed by observing the periodic formation of the shear plane using Particle Image Velocimetry (PIV) and Finite Element Method (FEM) [46, 53–55]. No model proposed so far reflects this complicated slip. In particular, a method for evaluating the frictional force between the wheel surface and the sand has not been established in the field of terramechanics. As a method for expressing this friction, a friction model based on the elasto-plastic constitutive law has been proposed [59–61]. By using this method to evaluate the friction between wheels and sand and combining it with the classical terramechanics model, terramechanics analysis can be realized by considering complex slippage, which was not possible until now.

The frictional force between the wheel surface and the sand increases with relative slip, which transitions to dynamic friction. If the frictional force does not exceed the shear strength of the sand in this process, the dynamic frictional force exerted at the interface becomes dominant without forming ruts. However, if it exceeds the shear strength of the sand, slippage occurs between sands, and ruts are formed. Sand-sliding on sand relieves the friction at the interface, and subsequently, the friction at the interface becomes dominant again. The author believes that a process such as stick slip is repeated under the condition that ruts are formed. By expressing each of these phases by combining friction laws and classical terramechanics

models, a highly accurate terramechanics model that considers the periodic formation of shear bands may be constructed.

3 MBD analysis using a terramechanics model: Traveling analysis of a mining dump truck

In this chapter, as an example of terramechanics simulation, multibody dynamics (MBD) analysis using a terramechanics model is demonstrated. In this study, the traveling simulation of a mining dump truck is performed, and the control method mounted on the vehicle is examined.

3.1 Introduction

In recent years, development aimed at unmanned, automated, and remote-controlled off-road vehicles, such as construction machinery and disaster robots, has been undertaken, and it has begun to be applied to various tasks [7, 62]. Furthermore, in the mining industry, the automatic operation of mining dump trucks and bulldozers is being promoted to reduce costs and improve safety. On a wide variety of off-roads, including soft ground such as in mines, vehicles are extremely likely to slip and become stuck, even at relatively low speeds. Therefore, efforts are being made to improve their traveling performance by introducing slip control, such as a traction control system (TCS) and an anti-lock braking system. However, a tool for pre-evaluating the motion characteristics of the vehicle is indispensable to examine the effects of these control methods. Numerical analysis based on terramechanics is effective for evaluating the traveling characteristics considering the slip and sinkage of off-road vehicles.

Therefore, in this study, by introducing the Bekker–Wong–Reece (BWR) model [2, 3, 35, 63, 64], which is a semi-empirical terramechanics model, to MBD analysis, the traveling analysis of mining dump trucks is performed and the effectiveness of TCS is examined. Specifically, a single-wheel model and vehicle model are created, and the climbing performance under several types of soil conditions is evaluated. Furthermore, the changes in terrain parameters that accompany the passage of wheels are expressed using a multipass model [65]. The effect of the multipass model on the traveling characteristics

of the vehicle is also examined.

3.2 Analysis model

This section describes the model for traveling analysis. In this study, an unmanned dump truck (Innovative Autonomous Haulage Vehicle: IAHV) manufactured by Komatsu Ltd. [66] was targeted. Table 3.1 lists the specifications of the IAHV. The IAHV has a total weight of 416 tons and a maximum load capacity of 230 tons, which make it one of the largest dump trucks used for mining. A major difference from general mining dump trucks is that each wheel is equipped with a drive motor, and a four-wheel drive/four-wheel steering system is adopted. Therefore, the drive torque of each wheel can be controlled independently.

Table 3.1: Specifications of the IAHV

Vehicle weight	[ton]	416
Maximum load capacity	[ton]	230
Power source		Diesel engine
Drive system		All wheel motor
Rated output	[kW(HP)]	2014 (2700)
Maximum speed	[km/h]	64
Minimum turning radius	[m]	15.9
Full length	[m]	15
Full width	[m]	8.5

In this study, MBD analysis was performed using the commercial software Adams. Here, the terramechanics model was introduced by using a user subroutine (tire model). Specifically, the six-component force of the tire was evaluated using the terramechanics model from the sinkage at each time step and is reflected in the vehicle behavior.

3.2.1 Single-tire traveling analysis

In the full vehicle model (four-wheel model), traveling analysis is possible considering not only the interaction between the ground and the tires but also the influence of the movement of the entire vehicle and the shape of the slope. However, a single-tire pre-analysis is also important to investigate the effect of the interaction between the ground and the tire, which is the focus of this study. Therefore, first, an analysis model focusing on a single-tire will be described.

Fig. 3.1 shows a single-wheel model. The tire specifications were set to be similar to those installed on the IAHV. The tire specifications are listed in Table 3.2. As for the tire width, the effective width considering flexibility was used in the terramechanics analysis. In the single-tire analysis, traveling parameters, such as drawbar-pull and slip ratio, were evaluated by inputting the specified translational velocity and angular velocity under a constant vertical load.

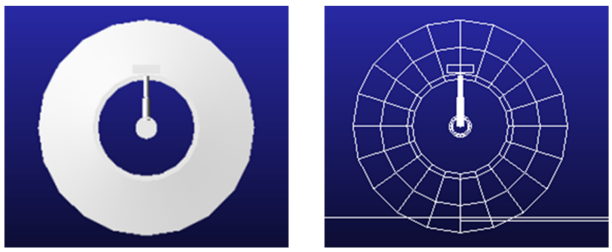

Figure 3.1: Single-tire model.

Table 3.2: Tire specifications (Michelin 59/80R63 XDR2).

Tire size		59/80R63
Diameter	[m]	4.028
Width	[m]	1.503

3.2.2 Full vehicle model

Fig. 3.2 shows the full vehicle model of the IAHV. The full vehicle model is constructed based on the vehicle specifications of the IAHV, and the drive system is 4WS. In addition, although the empty/loaded state can be selected as needed, the empty condition was used in this analysis. To confirm the effectiveness of TCS, a terrain surface with a slope of 15%, which has a relatively severe slope as shown in Fig. 3.3, was adopted as the course model. The driving conditions for the four-wheel model are four-wheel independent full throttle control based on the drive torque obtained from the actual machine. Full throttle control refers to axle torque control that reflects the wheel rotation velocity–wheel torque relationship measured in the actual machine. Moreover, as shown in Fig. 2.1, compression and elastic recovery of the terrain surface occur behind the wheels. Therefore, the height of the reference terrain surface after the wheel has passed is lower by $(1-\kappa)h_o$ with respect to the front of the wheel.

Next, the TCS introduced in this study will be described. Fig. 3.4 shows a schematic diagram of the traction force characteristics on soft ground. As shown in the figure, drawbar-pull shows a maximum value at a certain slip ratio and then gradually decreases due to excessive slippage. This is because the traveling resistance increases with sinkage. In this study, the system that controls the drive torque so that the wheel slip ratio is at the target value s_t is defined as TCS and introduced to the analysis.

Fig. 3.5 shows the TCS control flow. The vehicle velocity and the number of revolutions are detected, and the rotational velocity difference P_1 between the front and rear wheels is calculated using the following equation:

$$\frac{\omega_f - \omega_r}{\omega_f + \omega_r} = P_1 > P_c \tag{3.1}$$

Here, ω_f and ω_r are the tire average rotation velocities of the front and rear wheels (average rotation velocities of the right and left wheels) [rad / s], respectively. P_c is the TCS control value (threshold value). The TCS is activated when P_1 exceeding the threshold value continues for a certain

period (operation judgment time t_c). When the TCS is activated, the drive torque is controlled independently for each wheel to follow the target slip ratio s_t.

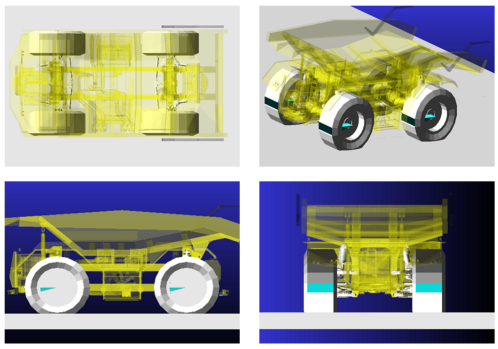

Figure 3.2: IAHV full-vehicle model.

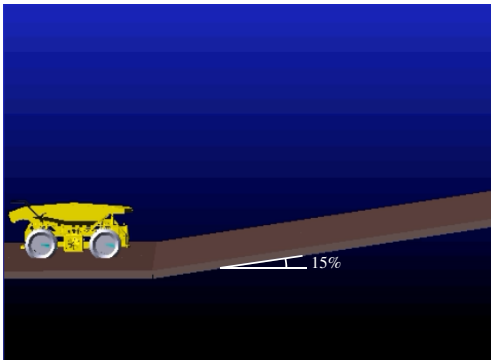

Figure 3.3: Road model for climbing analysis.

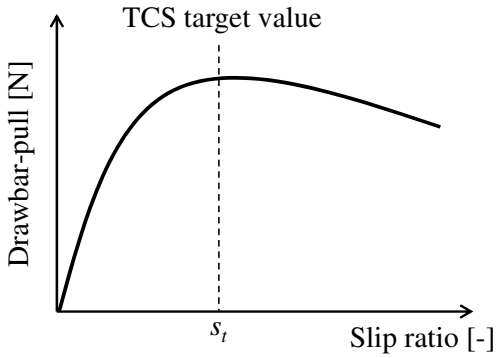

Figure 3.4: Schematic relationship between drawbar-pull and slip ratio.

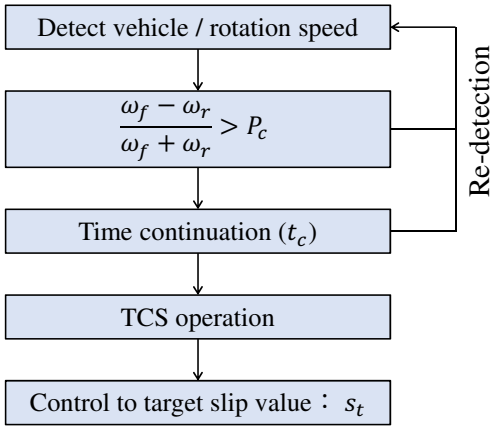

Figure 3.5: Calculation flow of TCS.

3.3 Climbing analysis of vehicles with TCS

In this section, the climbing analysis of the vehicle with TCS is performed, and the target slip ratio required for control is determined. Then, the effect of the presence or absence of TCS on the traveling characteristics is examined. Furthermore, the terrain surface conditions are changed, and the effect of the changes on the traveling characteristics and TCS is confirmed. The

traveling characteristics under each terrain surface condition are confirmed by acquiring the drawbar-pull–slip ratio relationship using single-tire traveling analysis.

3.3.1 Effect of target slip ratio

First, an appropriate target slip under the assumed terrain conditions is examined. Table 3.3 lists the terramechanics parameters set in this analysis. Note that the parameters do not assume a specific terrain surface. We adopted a value that can express the traveling characteristics on soft ground. Fig. 3.6 shows the drawbar-pull–slip ratio relationship obtained by performing single-tire traveling analysis under the conditions listed in Table 3.3. The figure shows that this relationship is qualitatively consistent with that of typical soft ground. In addition, under the terrain surface condition, drawbar-pull becomes the maximum value near a slip ratio of 0.25 [-]. On the other hand, the vertical load on the wheels changes depending on the posture of the vehicle. Fig. 3.7 shows the slip ratio–drawbar-pull relationship when the vertical load is changed. The peak of the drawbar-pull increases as the load increases, whereas it decreases at high slip rates. The results show that, at a high load, large traction is likely to be generated, but the sinkage increases due to the high load and the resistance from the front also increases. However, the slip ratios at which the drawbar-pull reaches its peak are approximately the same under all the load conditions.

A traveling analysis of the full vehicle model was performed on a terrain surface with a slope of 15%, which has the terrain conditions listed in Table 3.3. In the analysis, the target slip ratio s_t during the TCS operation was set to 0.10, 0.25, 0.40, and 0.60, and the effect of the control target value on the traveling characteristics was confirmed. The threshold value P_c was set to 0.10, and the operation judgment time t_c was set to 1.0 s.

Fig. 3.8 shows the changes over time in the horizontal displacement and slip ratio. Under all the conditions, the TCS operates near 8 s and finally maintains the target slip ratio. Moreover, when the target slip ratio is set

to $s = 0.25$, which maximizes the drawbar-pull in Fig. 3.6, the migration length becomes maximum. Therefore, this value is an appropriate target slip ratio for this terrain surface.

Table 3.3: Parameters of the terramechanics model.

c	Cohesion stress of soil [kPa]	0.100
ϕ	Soil internal friction angle [deg.]	15.0
k_c	Pressure sinkage modulus for cohesion stress [-]	0
k_ϕ	Pressure sinkage modulus for internal friction angle [-]	50.0
ρ	Soil density [kg/m^3]	1500
n	Pressure-sinkage ratio [-]	1.1
k_x	Soil deformation modulus in the x direction [m]	0.10
κ	Exit angle coefficient [-]	0.15
a_0	Maximum stress angle coefficient [-]	0.210
a_1	Maximum stress angle coefficient for slippage [-]	0.615

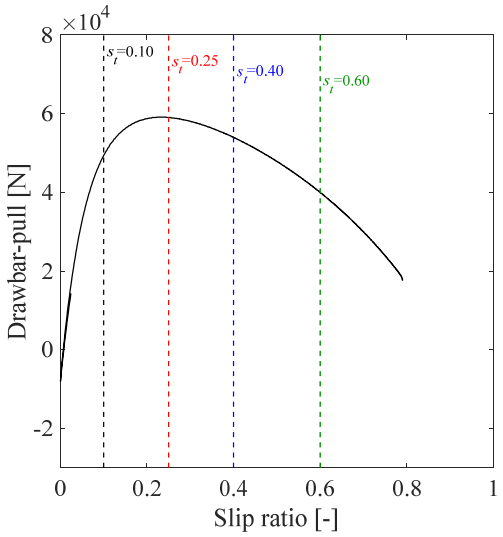

Figure 3.6: Relationship between slip ratio and drawbar-pull obtained using the single-tire model.

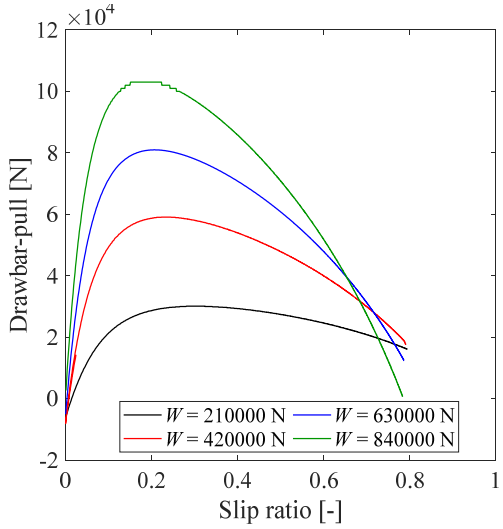

Figure 3.7: Relationship between slip ratio and drawbar-pull when the vertical load is changed.

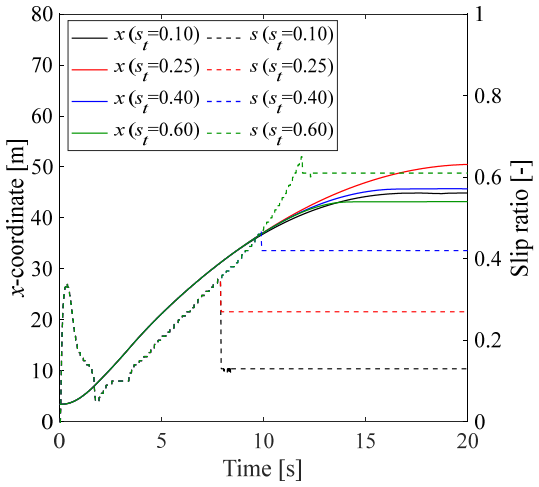

Figure 3.8: Variations of migration length and slip ratio with the elapsed time.

3.3.2 Effectiveness of TCS

In this section, the effectiveness of TCS is examined. The climbing analysis of the vehicle is performed using the above conditions and terramechanics parameters. The effect of the presence or absence of TCS (hereinafter TCS-ON or TCS-OFF, respectively) on the traveling characteristics of the vehicle is confirmed. The target slip ratio for TCS-ON is set to $s_t = 0.25$, which had a considerable effect in the analysis described in the previous section.

Fig. 3.10 shows the changes over time in the migration length and slip ratio. The figure shows that the vehicle becomes stuck under the TCS-OFF condition. However, under the TCS-ON condition, it continues to climb the slope within the analysis time. Thus, it can be confirmed that the TCS is effective in improving the traveling performance of vehicles on soft ground. In addition, driving at the lowest possible slip ratio is possible by properly controlling the target slip ratio. Therefore, from Eq. (2.10), not only the climbing performance but also the fuel consumption and tire consumption can be expected to be reduced.

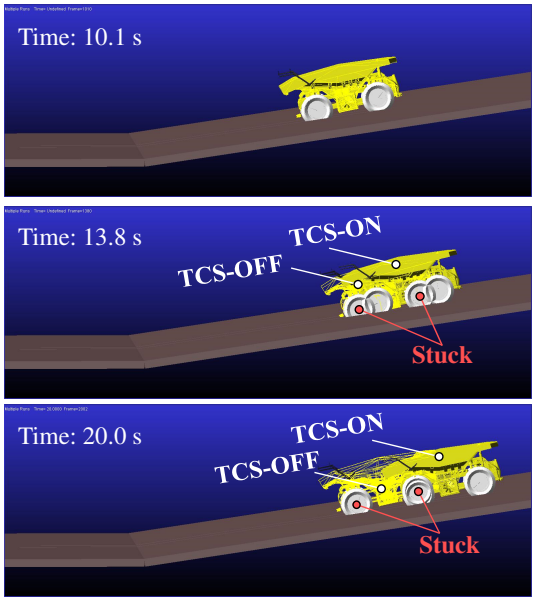

Figure 3.9: Comparison of traveling performance with and without the TCS.

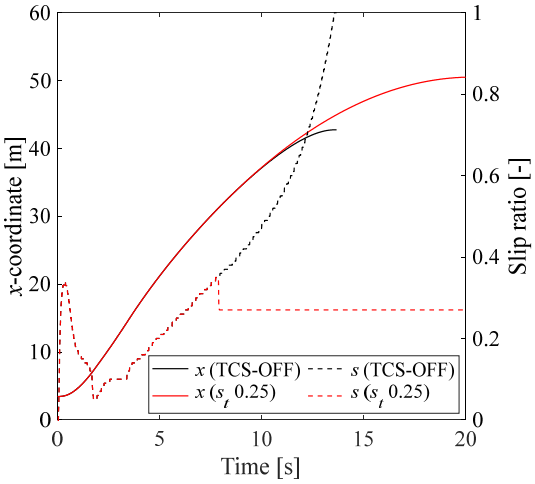

Figure 3.10: Variations of migration length and slip ratio with and without the TCS.

3.3.3 Effect of terrain condition

Next, the effect of the variation of the traveling characteristics depending on terrain conditions on the TCS control is examined. Using the terramechanics parameters of the three conditions (Type A, Type B, Type C) listed in Table 3.4, the same climbing analysis as in the previous section was performed. Fig. 3.11 shows the drawbar-pull characteristics obtained by analyzing the single-tire model. From the figure, under the conditions of Type A, Type B, and Type C, the drawbar-pull is the maximum at $s \approx 0.1$, 0.4, and 0.6, respectively.

Fig. 3.12 (a), (b) and (c) show the analysis results of the migration length obtained under the conditions of Type A, Type B, and Type C, respectively. Here, all the traveling analyses are performed under the condition of TCS-ON, and the target slip ratio s_t is 0.10, 0.25, 0.40, and 0.60. The figure shows that the climbing performance differs depending on the target slip ratio under all the terrain conditions. Moreover, when the slip ratio that maximizes the drawbar-pull is set to s_t in Fig. 3.11, the migration length becomes maximum. In general, the drawbar-pull required for climbing a slope differs depending on the slope, but this analysis method facilitates vehicle traveling analysis that reflects the terrain conditions and traveling conditions. Therefore, it is considered to be effective for the preliminary examination of TCS control methods and control values required for unmanned traveling.

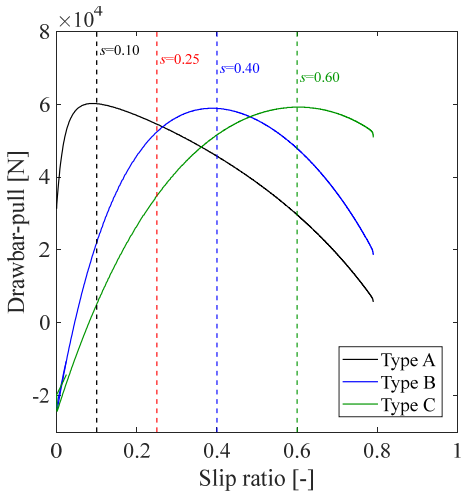

Figure 3.11: Relationship between slip ratio and drawbar-pull obtained with the soil conditions of Type A, Type B, and Type C.

Table 3.4: Analysis parameters for Type A, Type B, and Type C.

		Type A	Type B	Type C
c	Cohesion stress of soil [kPa]	0.100	0.100	0.100
ϕ	Soil internal friction angle [deg.]	14.0	25.0	35.0
k_c	Pressure sinkage modulus for cohesion stress [-]	0	0	0
k_ϕ	Pressure sinkage modulus for internal friction angle [-]	45.0	25.0	80.0
ρ	Soil density [kg/m^3]	1500	1500	1500
n	Pressure-sinkage ratio [-]	1.1	1.1	1.1
k_x	Soil deformation modulus in the x direction [m]	0.030	0.370	0.680
κ	Exit angle coefficient [-]	0.15	0.15	0.15
a_0	Maximum stress angle coefficient [-]	0.210	0.210	0.210
a_1	Maximum stress angle coefficient for slippage [-]	0.615	0.615	0.615

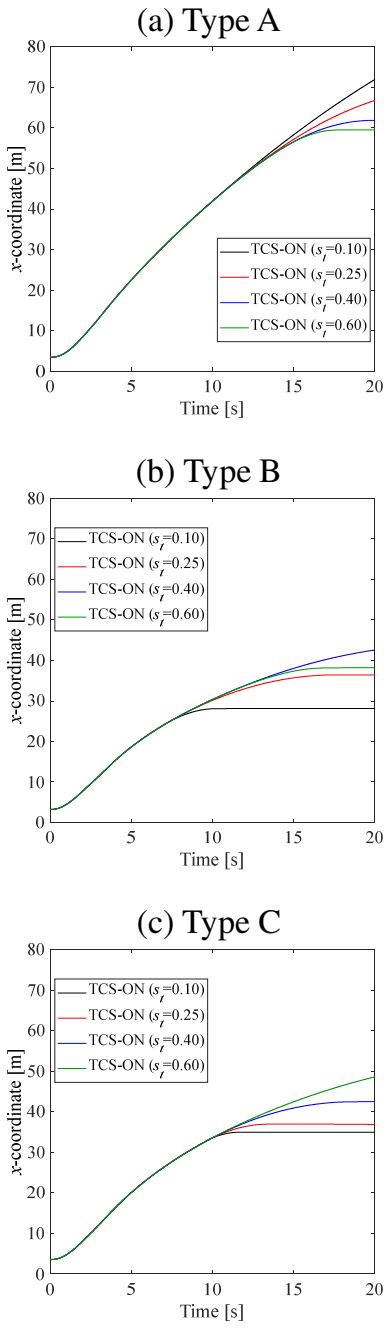

Figure 3.12: Variations of migration length with the elapsed time under the conditions of Type A, Type B, and Type C.

3.4 Examination of multipass effect

Finally, the multipass effect is examined. The multipass effect indicates that the terrain characteristics change when the ground is compacted by the tires and tracks when the off-road vehicle is traveling. It is apparent that the multipass effect has a strong influence on the traveling performance evaluation of off-road vehicles. In this study, the behavior when the rear wheels pass over the ruts that the front wheels have compacted is targeted. Here, the following preconditions are set for the MBD analysis using Adams.

1. The rear wheels must pass on the ruts of the front wheels, and offset from the ruts is not considered.

2. The compacted terrain property is not calculated automatically in the subroutine. This phenomenon is handled by setting the terramechanics parameters for the front and rear wheels separately. That is, it is assumed that the front wheels compact the soil and the rear wheels are traveling on a ground with different characteristics compared with the front wheels.

In setting the terramechanics parameters, we refer to the studies by Holm [67] and Senatore & Sandu [65]. Holm experimentally showed that the change in terrain characteristics is a function of the slip ratio, and the density change is approximated by the following equation:

$$\rho^N = \rho_0[1 + (1 - e^{-s/k_1})k_2 + k_3 N] \tag{3.2}$$

Here, k_1, k_2, and k_3 are multipass effect coefficients. s is the slip ratio, and N is the number of repeated runs. In addition, the cohesion stress c listed in Table 3.3 and the parameter k_x related to shear stress are approximated by the following equations:

$$c^N = c[1 + (1 - e^{-s/k_1})k_2 + k_3 N] \tag{3.3}$$

$$k_x{}^N = k_x[1 + (1 - e^{-s/k_1})k_2 + k_3 N] \tag{3.4}$$

In this study, for the sake of simplicity, the same k_1, k_2, and k_3 were used in Eq. (3.2)–Eq. (3.4).

In the following, the effect of the multipass model on the climbing performance will be examined. The set analysis conditions and terramechanics parameters are the same as those listed in Table 3.3. However, due to the multipass effect, the three terramechanics parameters shown in Eq. (3.2)–Eq. (3.4) change according to the number of repeated runs N. Specifically, the terramechanics parameters of $N = 0$ for the front wheels and $N = 1$ for the rear wheels are applied during the first climb. When passing the same terrain surface again, the terramechanics parameters of $N = 1$ for the front wheels and $N = 2$ for the rear wheels are applied. Fig. 3.13 shows the changes in density and cohesion stress due to the multipass effect used in this analysis. Here, assuming soft ground, the parameters are set to $k_1 = 0.10$, $k_2 = 0.50$, and $k_3 = 0.05$ to reproduce the situation where the ground is largely compacted in the first run and then gradually compacted in the subsequent runs. As this study is intended for the case where TCS operates, this issue was dealt with by substituting the control target value s_t into s in Eq. (3.2)–Eq. (3.4).

Fig. 3.14 shows the migration length when the multipass effect is applied under various conditions. Here, the solid line shows the case where the multipass effect is not considered, the broken line shows the case where the multipass effect is considered, and the dotted line shows the case where the same terrain surface is climbed again considering the multipass effect. The figure shows that the climbing performance is improved by considering the multipass effect. This is because the traveling performance is improved by compacting the ground, and the load sharing ratio changes due to the difference in sinkage. Fig. 3.15 shows the time-series variations in the sinkage of the front and rear wheels during the first run. The black line in the figure shows the sinkage of the front wheels, and the red line shows the sinkage of the rear wheels. The solid line is the result with the multipass effect, and the broken line is the result without the multipass effect. As the terramechanics

parameters are the same, there is no difference in the sinkage of the front wheels, regardless of the presence or absence of the multipass effect. The sinkage of the rear wheels is reduced by approximately 120 [mm] when the multipass effect is considered. It can be confirmed that the inclination of the vehicle body changed as the sinkage of the rear wheels decreased, and the drawbar-pull required for climbing also changed. From the time series variations of the vehicle pitch angle shown in Fig. 3.16, it can be observed that the inclination of the vehicle when the multipass effect is considered is suppressed. Thus, it is important to evaluate the multipass effect in the MBD analysis of a dump truck for mining, particularly when it is traveling on soft ground.

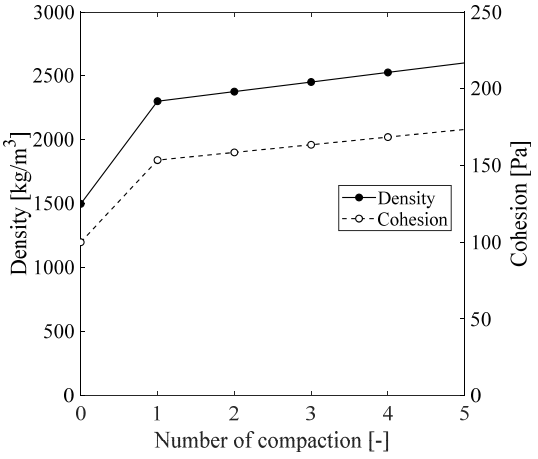

Figure 3.13: Change in density and cohesion due to multipass effect.

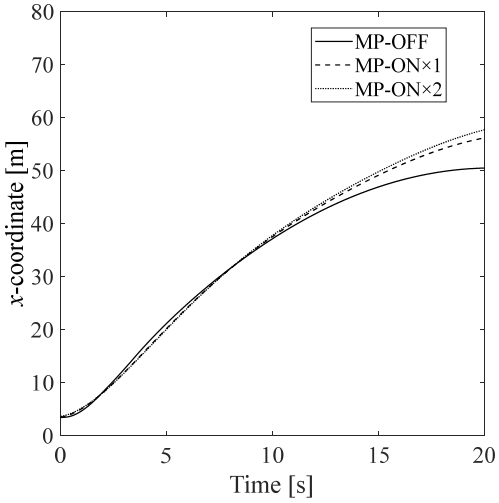

Figure 3.14: Multipass effect on migration length.

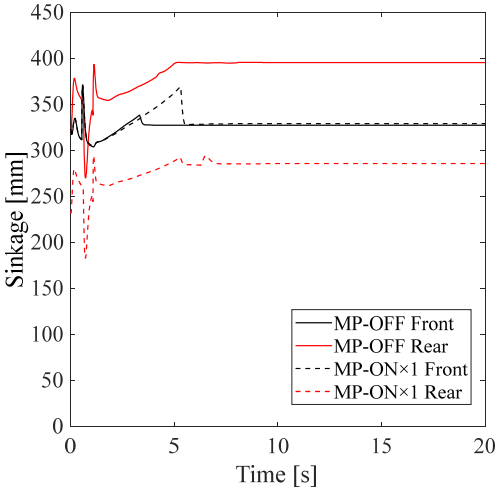

Figure 3.15: Multipass effect on sinkage.

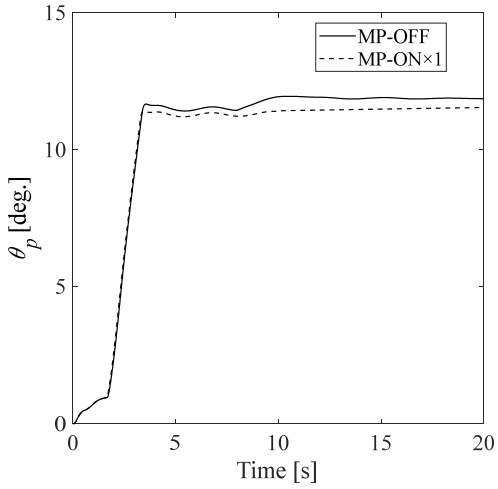

Figure 3.16: Multipass effect on vehicle pitch angle.

3.5 Conclusion

In this chapter, traveling simulations were conducted by introducing the terramechanics model for the interaction between the terrain surface and the dump truck for mining. In particular, TCS was incorporated to study slip control during climbing and its control target value. In addition, analyses in which the terrain conditions were changed to several types were conducted, and the effectiveness of TCS was confirmed for various terrain surfaces. Furthermore, it was shown that it is indispensable to consider the influence of the multipass effect in verifying the traveling performance and setting the control target value. However, when studying slip control systems, such as TCS, it must be considered that the traveling characteristics of the front and rear tires change when compaction occurs. Although not considered in this analysis, examining whether the target slip ratio of TCS should be set individually for each wheel according to the multipass effect should be undertaken as a future task. Furthermore, note that the terramechanics parameters used in this study do not assume specific terrain conditions. Analysis assuming specific terrain conditions requires on-site soil testing and parameter fitting.

This issue should be addressed in the future.

Furthermore, the terramechanics model used in this simulation has restrictions on the applicable shapes. The BWR model adopted in this study is intended for tires with a simple shape and does not assume simulations for wheels with protrusions called lugs or grousers. It is necessary to reexamine the terramechanics model used, to conduct traveling simulations and shape studies for tires with complex shapes.

4 Study on applicability of RFT to traveling analysis of wheel with grousers

As mentioned in Chapter 3, the BWR model, which is a classic terramechanics model, has restrictions on the applicable shapes. Therefore, in this chapter, the traveling characteristics of the grouser wheel are evaluated by utilizing RFT, which is a relatively new terramechanics. The applicability of RFT is verified by comparing the RFT analysis results with the DEM analysis results.

4.1 Introduction

In future moon and planetary exploration activities, various operations are expected on soft soils, such as the landing of landers, drilling and sampling of the ground, installation of observation equipment, and construction of bases. To realize these tasks, rovers and robots moving on soft ground are indispensable, and related research has been conducted.

However, it is widely known that the surface of the moon/ planet is covered with fine sand, called the "regolith", under a microgravity environment. Therefore, vehicles can easily sink and become stuck [68–71]. In addition, there are various sand ripples on the ground of Mars, and these are also known to interfere with wheel traveling [6, 12]. To proceed with tasks while avoiding getting stuck, it is effective to establish a traveling plan by simulators based on the terramechanics analysis method, which can accurately and quickly evaluate the traveling characteristics. There are various approaches to calculating the traveling characteristics of off-the-road vehicles on soft ground. Representative examples include numerical analysis methods, such as discrete element method (DEM) [39–45, 72] and finite element method (FEM) [46–48, 50, 73–75], focusing on the interaction between the traveling part and the soil. In these methods, advanced contact models and constitutive models are introduced, and thus, the soil deformation and movement can be accurately analyzed by adopting fine discretization (fine particles or

elements). However, it is difficult to apply DEM and FEM to the analysis of the behavior of the entire vehicle because high calculation cost is required.

Meanwhile, it is possible to evaluate the interaction between soil and machine within the framework of the multibody dynamics using common engineering terramechanics models, such as the Wong and Reece model (based on Bekker' s work). This type of semi-empirical approach can be applied to the behavior analysis of the entire vehicle at a relatively low cost [6, 35, 76]. Furthermore, in general, although the rover' s wheels are accompanied by grousers or lugs to improve the traveling performance, this semi-empirical approach can also be applied to such cases. However, there are restrictions on calculable shapes, and problems, such as being unsuitable for arbitrary traveling parts, remain.

On the other hand, Resistive Force Theory (RFT) has been proposed to empirically estimate the reaction force of a rigid body moving inside a loose granular medium. Although the RFT was originally developed for viscous drag problems, RFT has attracted renewed attention in recent years as a method that can easily reflect the interaction between a granular medium and a traveling part having arbitrary shapes (including parts, such as legs, interacting with soil) [1, 36–38]. The RFT has been applied to multibody dynamics analysis for legged mobile robots [1, 36] and wheel traveling analysis [38], and its applicability for terramechanics problems has been verified. Furthermore, Slonaker et al. [38] utilizes the intrusion force evaluated by RFT to derive general scaling relations for locomotion in granular media. Note that Askari and Kamrin [37] have already explained the physical reasons why granular media having complex behaviors locally can be expressed by RFT. According to their research, RFT may be applicable to cohesive media unless a target soil is a velocity-dependent viscous medium. In addition, they are organizing a new family of resistive-force-obeying material, and it has been shown that RFT shows good prediction accuracy with loose granular media. Therefore, if this theory can also be applied to traveling analysis of wheels with grousers (or lugs), RFT is expected to be an effective

method in the field of terramechanics.

In this study, we examine the effectiveness of RFT on the analysis of wheels having grousers by comparing RFT results with DEM analysis results, because DEM is already recognized as an effective numerical analysis method in the field of terramechanics. The strategy of this research is as follows:

1). DEM can demonstrate high analytical accuracy if appropriate conditions are set for the interaction between soil and machine [39–45, 72].

2). We conducted wheel traveling analyses for a loose frictional soil as a virtual test based on the DEM. We used rigid wheel models with several patterns of grousers.

3). Using a DEM ground model (testbed) with the same condition of wheel traveling analysis, we conducted a plate intrusion test to obtain parameters for RFT analysis.

4). Using the parameters obtained in Step 3, we conducted an RFTbased wheel traveling analysis under the same conditions as in Step 2.

5). If the results of the DEM can be satisfactorily reproduced by RFT, it will lead to the realization of multibody dynamics analysis with high accuracy and low cost for complex wheel shapes. Also, if there is some discrepancy between them, it is possible to clarify the cause and to consider the scope of application.

In Section 4.2, we conduct plate tests using both DEM and RFT and compare these results. We then identify the parameters for calculation of RFT. In Section 4.3, we calculate the traveling characteristics of the wheels with grousers using the obtained RFT parameters, and we compare them with the calculation results using DEM. Furthermore, we also discuss the validity of RFT and its limitations. Finally, in Section 4.4, we present our conclusions.

4.2 Virtual plate test using DEM

4.2.1 Analysis model

As a virtual plate intrusion/extrusion test, we conducted DEM analysis. In this study, the discrete element function of the commercial software LS-DYNA was used. Fig. 4.1 shows the DEM analysis model. Here, the soil particles were filled in the testbed by free falling from the upper side, to realize a loose deposit condition (the density is 905.4 kg/m^3). We adopted the Voigt model for the treatment of particle contact. Table 4.1 shows the parameters used for the DEM analysis. Here, we chose DEM parameters as that the angle of repose corresponds to typical sandy soil.

The plate was set to be a rigid body, and the prescribed forced displacement was given corresponding to the specified orientation angle b and velocity vector angle c. Here, the plate was the same size as that used for the real test [1], and we assumed that the friction coefficient between the soil particle and plate is the same as that between the soil particles.

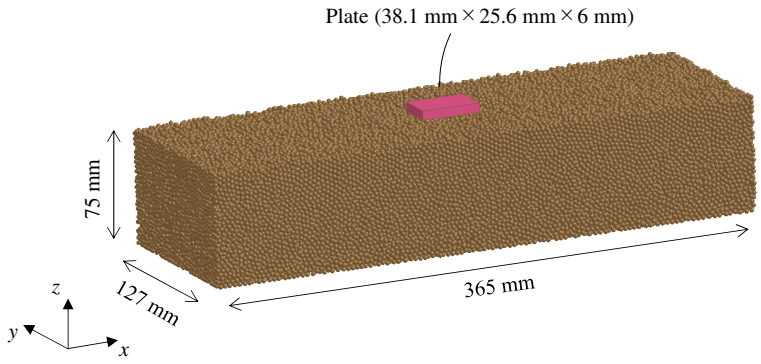

Figure 4.1: DEM Analysis model for plate tests.

Table 4.1: Analysis condition of DEM model.

Particle diameter	[mm]	3.00
Static friction coefficient	[-]	0.750
Dynamic friction coefficient	[-]	0.750
Density of particle	[kg/m^3]	1550
Young's modulus	[MPa]	100
Poisson ratio	[-]	0.400

4.2.2 Determination of scale factor ζ

First, the scale factor was determined using the results of the virtual plate test by DEM. Because the scale factor is obtained from Eq. (2.17), we analyzed the condition in which the horizontal plate intrudes vertically downward. Fig. 4.2 shows the stress - sinkage relationship obtained by DEM and RFT. Here, the solid line is the result of DEM, while the dashed line is the result of RFT. Because α is defined as the stiffness of the stress - sinkage relationship, the scale factor can be determined by the inclination. In general, although the stress - sinkage relationship shows nonlinearity, the RFT result shown in Fig. 4.2 was approximated to a straight line passing through the origin by the least-squares method. Thus, the scale factor of the soil model shown in Fig. 4.1 was determined to be 0.191.

Next, to confirm the validity of the obtained scale factor, we compared the stress - sinkage relationships between DEM and RFT under several orientation angles β and velocity vector angle γ. The scale factor of RFT used was $\zeta = 0.191$, which was already determined. Fig. 4.3 shows the stress - sinkage relations under two conditions of intrusion and two conditions of extrusion. The solid line is the result of DEM, while the dashed line is the result of RFT. It is confirmed from Fig. 4.3 that the stress - sinkage relations in the horizontal and vertical directions obtained by the RFT are in good agreement with those obtained by DEM. The abovementioned results show that the virtual plate test using DEM can be reproduced by RFT.

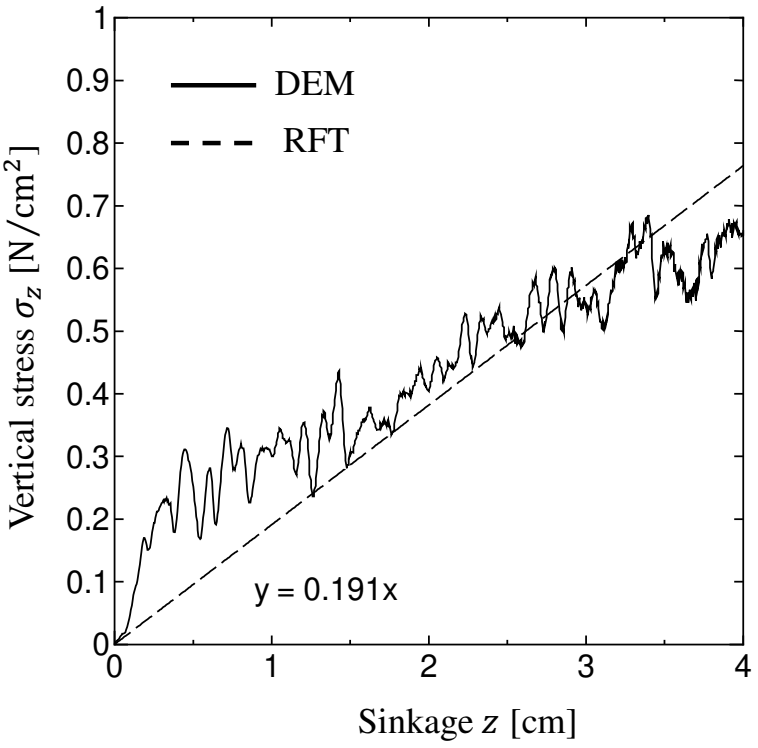

Figure 4.2: Comparison of the vertical stress vs. sinkage relation between DEM and RFT. Here, $\beta = 0$and $\gamma = \pi/2$. The scale factor is determined as $\zeta = 0.191$ by the linear approximation.

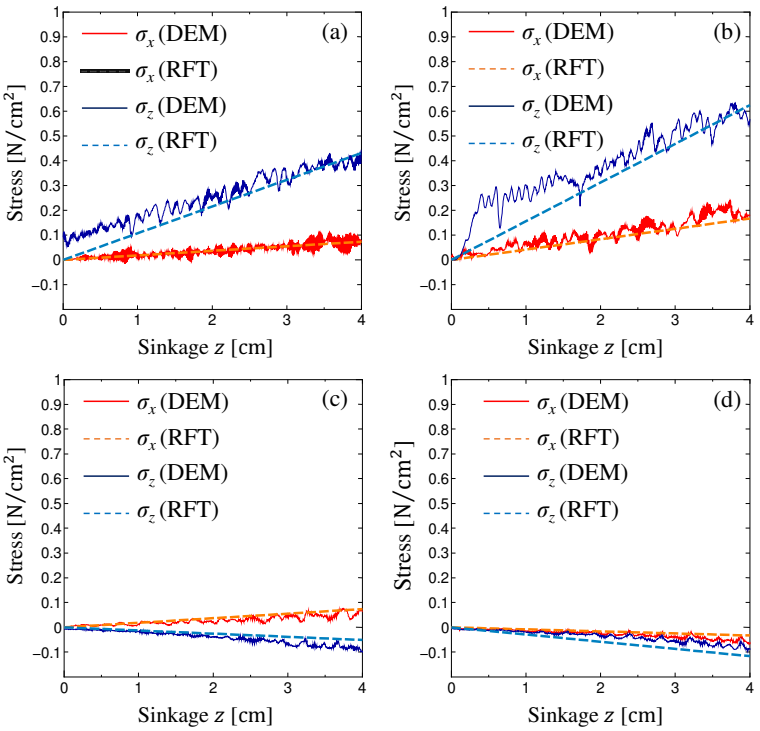

Figure 4.3: Comparison of the stress vs. sinkage relation between DEM and RFT under various orientation angles and velocity vector (intrusion/extrusion) angles: (a) $\beta = 0$, $\gamma = \pi/4$; (b) $\beta = \pi/4$, $\gamma = \pi/2$; (c) $\beta = 0$, $\gamma = -\pi/4$; and (d) $\beta = \pi/4$, $\gamma = -\pi/2$.

4.3 Traveling analysis of wheel with grousers

Because the consistency of DEM and RFT was confirmed in the plate test, in this section, we confirm the applicability of RFT to the wheel traveling analysis with more-complex shapes and movements.

4.3.1 Analysis model and boundary condition

Fig. 4.4 shows the DEM analysis model for the single-wheel traveling analysis, which is used as the virtual test. We adopted three types of wheel, as

shown in Table 4.2, while the condition of the testbed was the same as in Fig. 4.1. The width of the wheel and that of the testbed were the same; thus, the plane strain condition was assumed.

In the DEM and RFT analyses, the slippage of the wheel was controlled by independently setting the prescribed traveling velocity v and rotation velocity ω. For verification of RFT, we focused on the variation of the coefficient of traction, which is defined by the ratio of the drawbar-pull and wheel load. The slippage s is defined as follows:

$$s = 1 - \frac{v}{D\omega/2} \tag{4.1}$$

where D is the diameter of wheel. In the analyses, the rotation velocity ω of the wheel was fixed at 0.5 rad/s, while the traveling velocity v was adjusted. In addition, a lightweight and compact vehicle was assumed for these analyses, and the wheel load was set to be 20 N.

In this study, the wheel surface part was discretized by a 0.5 mm length of plates. The grouser part was discretized by 30 plates, while wheel part was discretized by 0.01 rad intervals. We also conducted the RFT analysis under the condition that the discretization was further refined, and we confirmed that the influence was small enough.

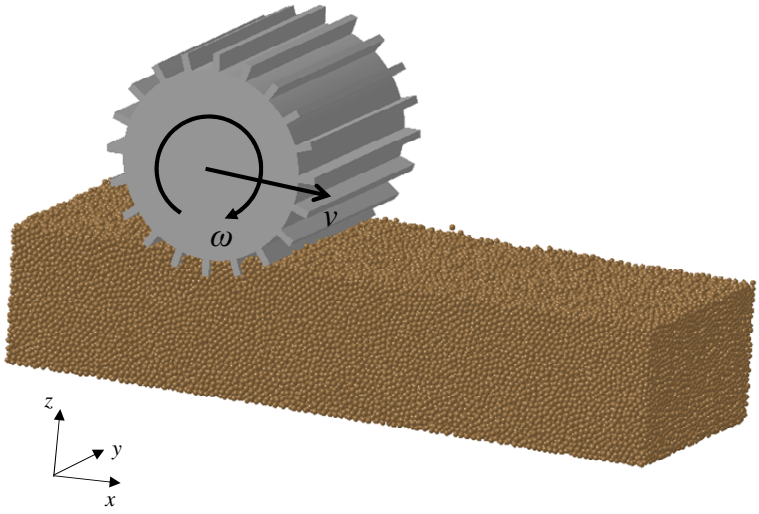

Figure 4.4: DEM analysis model for the single wheel traveling test. The ground condition is the same as the model shown in Fig. 4.1.

Table 4.2: Specifications of wheels.

			Wheel A	Wheel B	Wheel C
Number of grouser	N_g	[-]	20	20	15
Height of grouser	h_g	[mm]	6	9	9
Thickness of grouser	t_g	[mm]		4	
Wheel diameter	D	[mm]		100	
Wheel width	B	[mm]		127	

4.3.2 Comparison of results obtained by DEM and RFT

Because the virtual test bed of the DEM analysis model shown in Fig. 4.4 was the same as that of the plate tests, the same scale factor f already determined was used for comparison of results between by DEM and RFT.

Figs. 4.5(a), 4.6(a), and 4.7(a) show variations in the coefficient of traction as a function of elapsed time under each slippage obtained by DEM

analysis using wheels A, B, and C. Here, a low-pass filter was used (cut-off frequency is 3 Hz) for the results of DEM, as the fluctuation was large. As can be seen from the figure, the drawbar-pull fluctuates owing to the influence of grousers. Furthermore, the drawbar-pull in steady traveling conditions increases with slippage and height of grousers in the range of the examined conditions. Figs. 4.5(b), 4.6(b), and 4.7(b) show variations in the drawbar-pull as a function of elapsed time under each slippage obtained by RFT analysis using three types of wheel. As with DEM analysis results, the drawbar-pull in steady traveling conditions increases with slippage and the height of grousers in the range of examined conditions. In the RFT, the effect of slippage is reflected by the change in the velocity vector angle γ. In addition, the periodic fluctuation of the drawbar-pull by grouser is also reflected owing to the change in γ and β during traveling. Comparing the state of fluctuation between three types of wheel, it can be seen that the amplitude of the drawbar-pull at the same slippage becomes higher together with grouser height. Furthermore, it is also seen from the figures that the period of fluctuation is influenced by the number of grousers. From this fact, it can be confirmed that the RFT makes analysis reflecting the shape of the wheel possible. Furthermore, as has been observed in experiments (e.g., Shikanai et al., 2000 [77]), after the starting of traveling under a constant slippage, drawbar-pull increases gradually and then converges to a steady value.

To examine the applicability of RFT in more detail, we created the stress distribution on the wheel surface during steady traveling, as shown in Fig. 4.8. Here, the stress distribution is the result of Wheel A. The red lines indicate stress generated in the horizontal direction, while the blue lines indicate stress generated in the vertical direction. The length of the lines corresponds to the magnitude of the stresses, and the direction of the lines extending from the wheel surface corresponds to the direction of the stresses applied to the wheel. Compared with the stress in the horizontal direction, the area where the stress acts on the opposite side in the traveling direction (left direction in the figure) at 0.1 slippage is wider than that at 0.5 slippage.

Furthermore, the distribution area of stress in the vertical direction becomes large with the increase in slippage. This is because the translational velocity per unit length increases with low slippage, and the region where the velocity vector angle γ is inclined forward increases. Thus, the phenomenon that the drawbar-pull increases with slippage is naturally expressed by RFT. A similar tendency was also confirmed in Wheels B and C. However, it should be noted that the relationship between sinkage and slippage cannot be properly expressed by RFT, as will be explained in a later discussion.

Fig. 4.9(a) and (b) show the relationship between the steadystate coefficient of traction and slippage obtained by DEM and RFT, respectively. The DEM results show a similar tendency to that reported in Sutoh et al. (2012) [76]. However, there is no quantitative agreement between the DEM and RFT analyses, and the consistency of the influence of grousers (height and number) is not found. The cause of this will be discussed in the next section.

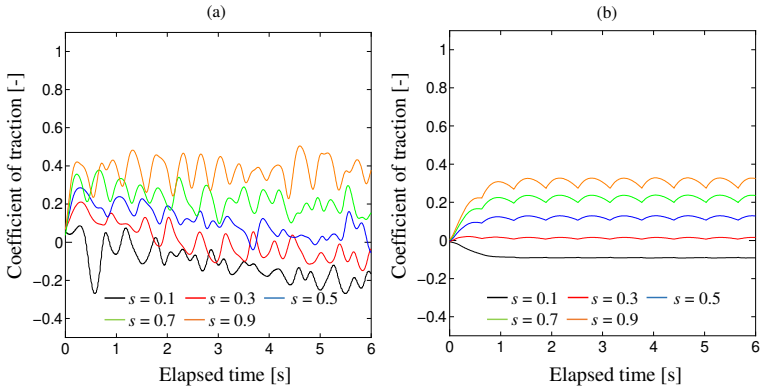

Figure 4.5: Variation of drawbar-pull with elapsed time under each slippage, where the wheel A is used for calculations: (a) DEM; and (b) RFT. The coefficient of traction is computed by dividing the drawbar-pull by the constant wheel load.

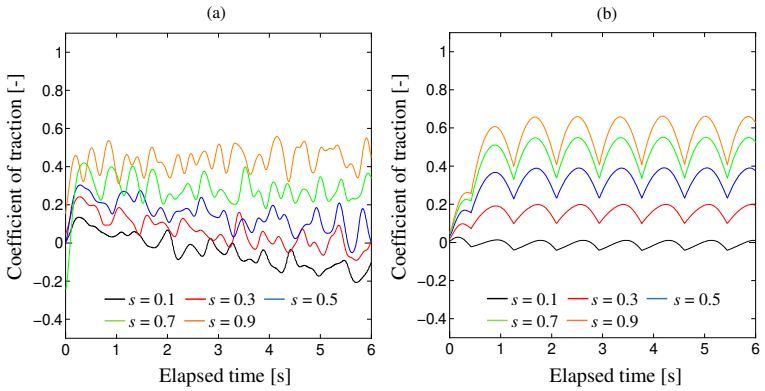

Figure 4.6: Variation of drawbar-pull with elapsed time under each slippage, where the wheel B is used for calculations: (a) DEM; and (b) RFT. The coefficient of traction is computed by dividing the drawbar-pull by the constant wheel load.

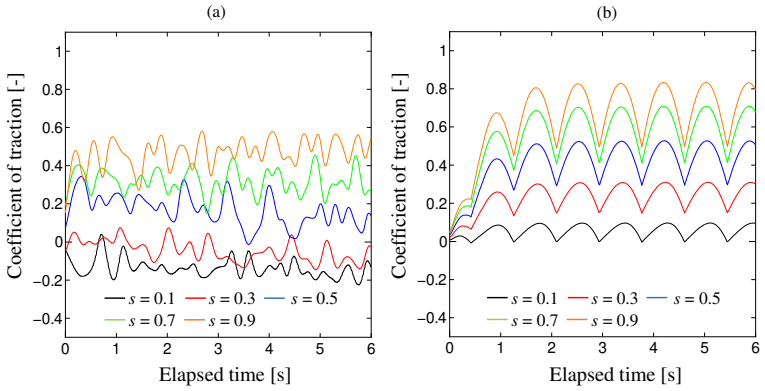

Figure 4.7: Variation of drawbar-pull with elapsed time under each slippage, where the wheel C is used for calculations: (a) DEM; and (b) RFT. The coefficient of traction is computed by dividing the drawbar-pull by the constant wheel load.

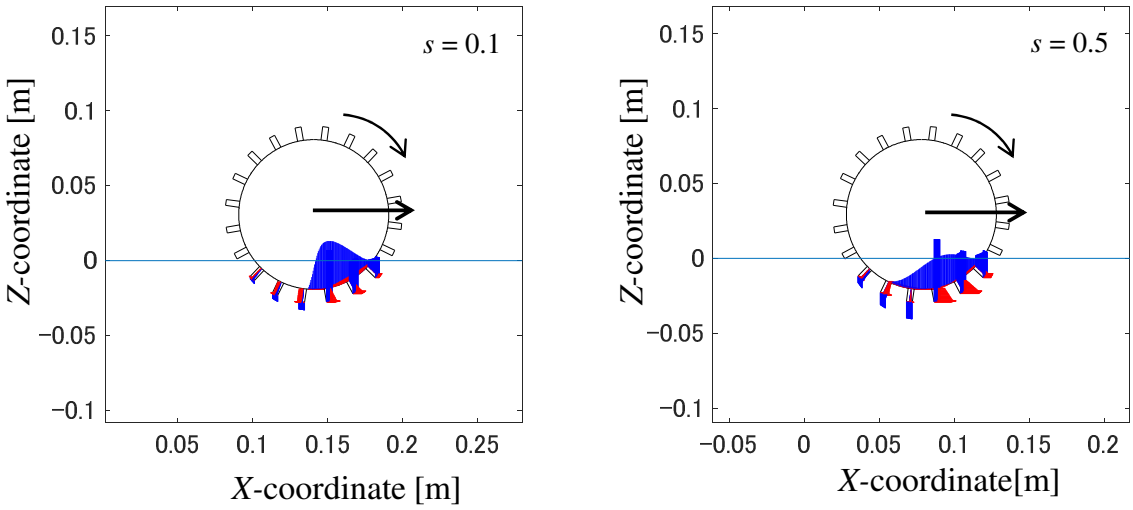

Figure 4.8: Stress distribution on wheel A. The red lines indicates stress generated in the horizontal direction, while the blue lines indicates stress generated in the vertical direction.

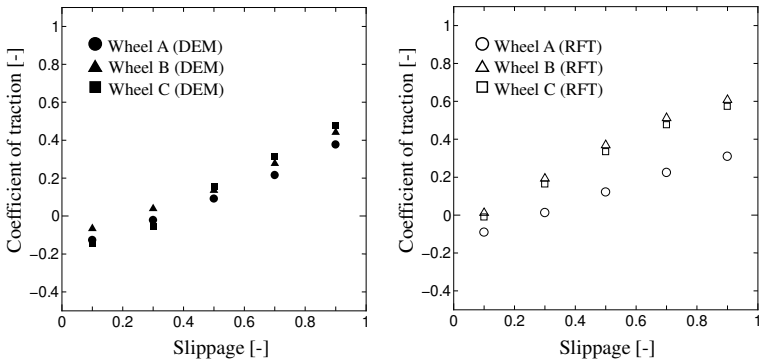

Figure 4.9: The relationship between average coefficient of traction in steady state and slippage: (a) DEM; and (b) RFT.

4.4 Discussion

In this section, we discuss the reason why the relationships between the steady-state drawbar-pull and slippage are different in DEM and RFT. The first reason is that shearing of soil is not considered sufficiently in the calculation of RFT. In general, when the wheel with grousers travels on soft ground, particles are packed between grousers. Hence, an additive driving force is generated by forming a shear plane between soil particles during traveling.

Fig. 4.10 is a contour map of the absolute value of the particle velocity during wheel traveling obtained by DEM analysis using Wheel B. Here, the slippage is 0.5. As is confirmed from the figure, the particles between the grousers have large velocity, and the shearing between the particles is expressed in the DEM analysis. In addition, as RFT is targeted for the movement (like a swim) of the plate in granular media, the moving behavior of soil toward the rear of wheel in a high-slippage regime is not considered. Therefore, as can be seen from Fig. 4.8, the relationship between sinkage and slippage in RFT is not properly evaluated. (Note that this shortcoming is the same for the conventional terramechanics model.)

The second reason is that, to fully demonstrate the resistive force, it is necessary for the plate to move independently. That is, when considering the movement of multiple plates, it is necessary that the distance between the plates is sufficiently secured, whereby the wheel with grousers examined in this study is not necessarily guaranteed this condition. To examine the two above-mentioned reasons in more detail, DEM and RFT analyses of two types of plate test was carried out. Here, the soil condition is the same as in Fig. 4.1.

Fig. 4.11 shows a schematic diagram of the first analysis condition and obtained results. Fig. 4.11(a) shows a case where one independent plate rotates in the soil. On the other hand, the model, as shown in Fig. 4.11(b), consists of two plates, in which the second plate follows the first plate, moving in the same manner as in Fig. 4.11(a). Note that two plates maintain

the parallel relationship and the distance between the normal lines with each other. Fig. 4.11(c) and (d) show the analysis results of variations of resistive-forces in the horizontal direction and vertical direction obtained by DEM and RFT, respectively. The scale factor of RFT is obtained from Fig. 4.1 (i.e., $\zeta = 0.191$). The solid line is the result of DEM, while the dashed line is the result of RFT. As can be seen from the figure, when one plate independently rotates in the soil—Fig. 4.11(a) and (c)—results obtained by DEM and RFT are in good agreement. However, in case of two plates—Fig. 4.11(b) and (d) —the result of DEM analysis is smaller than that of RFT. In RFT, if the plate has the same β and γ, the same resistive force is generated. Hence, the force of the two-plate model is simply twice that of the one-plate model, based on the superposition principle. However, in DEM analysis, when the distance of the plate is short, the number of particles between plates decreases, and the resistive force generated in the rear plate is correspondingly reduced. When the distance between plates becomes sufficiently large, the analysis results obtained by DEM and RFT almost agree with each other, even in the case of multiple plates.

Fig. 4.12(a) shows a schematic diagram of the second analysis condition. In the analysis, a model with a lid attached to two plates penetrated soil by a fixed amount (16 mm), and then it moved at a constant velocity in the horizontal direction. Here, the two vertical plates have a distance such that they do not affect each other, and the sum of the resistive forces almost agrees with the analysis of RFT. Fig. 4.12(b) shows the variation of the resistive force obtained by DEM and RFT. The fluctuation of the result of DEM analysis occurs when getting over the particle. As can be seen from the figure, the value of the resistive force in the steady state is larger in DEM than the value calculated in RFT, because the packed soil particles between two vertical plates are subjected to vertical pressure by the lid and then generate additive driving force by forming a shear plane.

Based on the above two types of analysis results and the result of the particle velocity, shown in Fig. 4.10, when RFT is applied to the analysis of

the wheel with grousers, the plate interval and shearing of particles cannot be ignored. RFT can predict the reaction force with sufficient accuracy for cases where the interaction between the object (plate) and granular media is dominant, such as a legged mobile robot. Meanwhile, to apply RFT to cases where the interaction between particles cannot be ignored, some extension of the model is necessary. Even so, we believe that the low calculation cost and high-precision performance of RFT is quite attractive, and we can use it for various terramechanics problems.

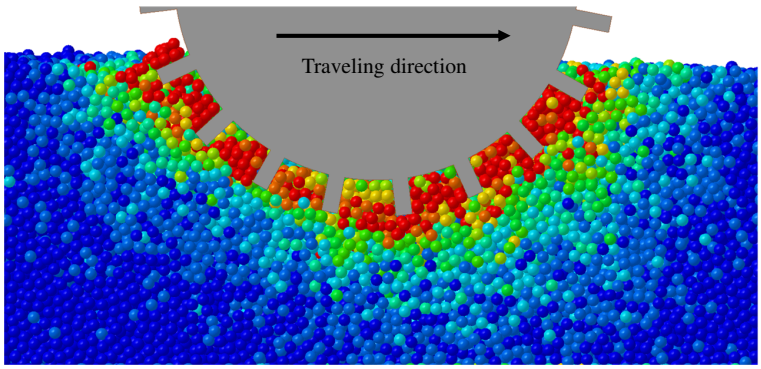

Figure 4.10: Snapshots of the wheel-soil interaction in the DEM analysis, where the wheel B is used and the slippage is 0.5. The colors in the contour map represent the magnitude of particle velocity.

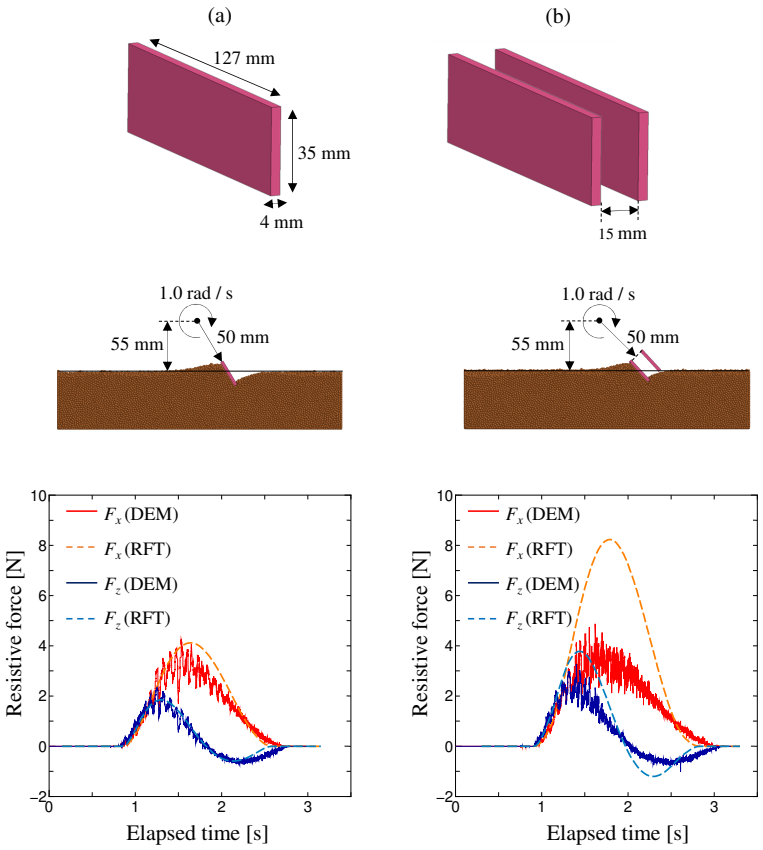

Figure 4.11: Schematic diagram of analysis condition for plate rotation test and variation of resistive force in the horizontal direction and vertical direction with elapsed time: (a) condition of single plate rotation; (b) condition of two plates rotation; (c) results of single plate rotation; and (d) results of two plates rotation.

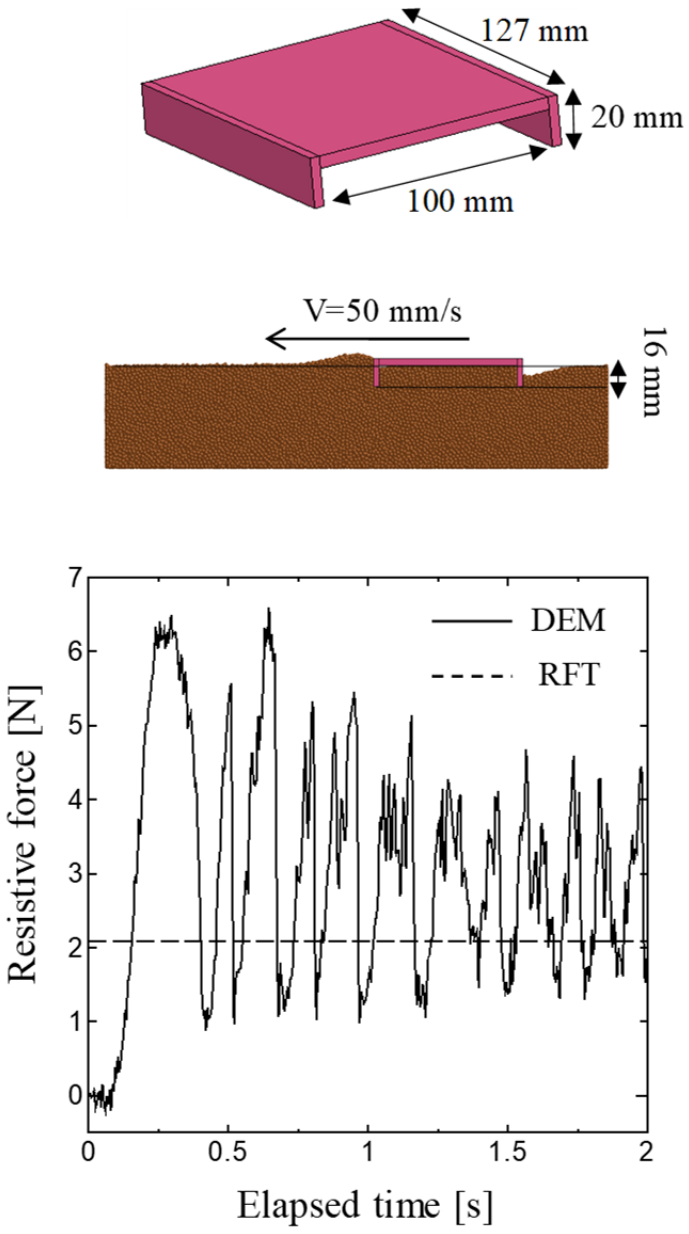

Figure 4.12: Schematic diagram of analysis condition for bulldozing test of lidded plates and variation of resistive force in the horizontal direction with elapsed time: (a) condition of bulldozing test; and (b) results of DEM and RFT analyses.

4.5 Conclusion

In this study, we examined the applicability of RFT for the analysis of a traveling wheel having a grouser by comparing it with the DEM analysis results. Specifically, we conducted plate intrusion/ extrusion and a wheel traveling analysis for a loose frictional soil as a virtual test based on the DEM. In plate tests, the results were revealed to be roughly consistent between DEM and RFT, but quantitative agreement was not confirmed in the wheel traveling analyses. To examine the discrepancy between DEM and RFT for the wheel traveling behavior, we conducted two additional analyses. We found that the discrepancy is because interaction between particles cannot be taken into consideration in RFT. In addition, we found that the distance between grousers also affects the resistive force. Based on the results and discussion, we believe that RFT might be a promising approach in terramechanics, although it is necessary to expand RFT to apply it to the analysis of the traveling behavior of a wheel with grousers. Note that RFT can easily be extended to three-dimensional problems. Therefore, RFT can also be applied to the problem of turning ability that is indispensable for multibody dynamics analysis of vehicles.

In this study, few kinds of numerical conditions were examined using the plane strain condition of DEM. Thus, the range of examined conditions is limited. To shows the robustness of RFT, various conditions should be considered. In addition, RFT should be verified by comparing it with a real test.

5 Examination of wheel shape based on terramechanics analysis

Although RFT has some drawbacks, it enables mechanical analysis considering the complicated shape of an object. Therefore, in this chapter, the traveling characteristics of the grouser wheel are evaluated by utilizing RFT, which is a relatively new terramechanics model proposed in recent years, DEM, which is one of the numerical analysis methods, and model experiments. In addition, through these studies, a grouser shape suitable for lunar / planetary exploration rover wheels will be proposed.

5.1 Introduction

As mentioned in the section 4, surfaces of moon and planet are covered with fine sand called regolith [68], and vehicles can easily sink and get stuck in the ground [78]. To avoid such accidents, the traveling performance of rover wheels has been improved by attaching protrusions called grousers or lugs on the surface of rover wheels. However, the cross-sectional shape of the grousers used is usually rectangular, and other shapes have not been investigated in sufficient detail.

The study of the interaction between soil and machinery is called terramechanics. Traveling performances have been investigated on a wide scale from exploration rovers to mining dump trucks considering terramechanics principles [3]. The evaluation approaches for the traveling performance can be primarily divided into three categories. The first approach involves experimental methods. It is possible to directly obtain the traveling characteristics by conducting physical experiments, for example using targeted vehicles or their undercarriage. The second approach involves performing numerical analysis using the discrete element method (DEM) [39–45, 72]and the finite element method [46–50, 73–75]. In numerical analyses, the traveling performance can be evaluated in detail if appropriate modeling and discretization are carried out as it is possible to track the interaction of the

traveling part and deformable soil with high accuracy. The third approach is based on a semi-empirical theoretical formula known as the terramechanics theory [3, 6, 35, 55, 71, 76]. The terramechanics theory predicts the traveling performance of off-road vehicles using plate intrusion tests and direct shear tests, and is also used in multibody dynamics analysis [6, 12, 15, 35].

Terramechanics-based studies on grousers have been conducted focusing mainly on crawler vehicles [76, 79, 80]. Yong et al. (2012) investigated the influence of grouser height and interval on the driving force. They found that the grouser interval contributes significantly to the generation of the driving force, and a certain ratio of the grouser interval to the grouser height corresponds to the highest thrust. In addition, Muro (1993) measured the driving force under various grouser interval to grouser height ratios and found that the maximum thrust is generated when the ratio is in the range of 3 - 4. Several studies have also been conducted on wheel vehicles. For example, Yang et al. [81] measured lug - soil interaction forces of actively actuated lug. In addition, Yang et al., [82] developed a new form of wheel equipped with actively actuated lug (ALW). They showed that ALW can improve drawbar performance in the traveling experiment of the wheel. However, most previous studies simply considered the cross-sectional shape of the grouser to be rectangular, and only a few studies focused on the evaluation of different grouser shapes.

In this study, we examined the grouser shape of rigid wheels based on all the three approaches mentioned above, namely using a simple DEM analysis, single-wheel experiments, and terramechanics theory. Specifically, we compared the traveling performance of wheels employing rectangular-shaped and trapezoidal-shaped grousers. We verified the effectiveness of the packing effect demonstrated by trapezoidal-shaped grousers, in which soil is strongly compacted between grousers during traveling, as a new concept for wheel design. In terms of terramechanics theory, we adopted the resistive force theory (RFT) [1, 37, 38], which has attracted attention in recent years. The RFT can be employed to evaluate the resistive stress generated in an arbitrarily-

shaped object moving in granular media at low calculation cost. Therefore, the existence of packing effect and its effectiveness can be logically verified using the difference between the drawbar-pulls obtained from single-wheel experiments and RFT.

5.2 Packing effect

5.2.1 Basic concept of packing effect

In this study, we focused on the effectiveness of the trapezoidal-shaped grouser, which has not yet been investigated in existing studies. It is considered that trapezoidal-shaped grousers exhibit packing effect owing to soil compaction between the grousers during motion, which serves to improve the traveling performance. A direct effect of this approach is that the normal stress σ under the rigid wheel becomes large, and sinkage of the wheel is also suppressed.

In the conventional terramechanics theory, the Coulomb's failure criterion defined in Eq. (5.1) is widely used, and traction force is mainly exerted by the shear stress τ generated under the wheel, that is,

$$\tau = c + \sigma \tan \phi \tag{5.1}$$

where c and ϕ denote the cohesion and internal friction angle, respectively. The distribution of normal stress σ is evaluated according to the vertical load and slippage of the wheel, and subsequently, the distribution of shear stress τ can be evaluated using Eq. (5.1). Further, the driving force of grouser wheel is generated not only by the shear stress but also by the resistive force generated by the paddling of grousers. Assuming a simple superposition, the drawbar-pull F_x can be defined as follows:

$$F_x = F_s + F_g - R_c \tag{5.2}$$

$$F_s = \int \tau \cos \theta_s dA \tag{5.3}$$

$$F_g = \sum_{i=1}^{N_g} f_{xi} \tag{5.4}$$

R_c is the traveling resistance, F_s is the force exerted by the shear stress, and F_g is the sum of the resistive forces of N_g grousers in the x direction (see Fig. 5.1).

A rectangular-shaped grouser has been traditionally adopted to maximize the second term in Eq. (5.2) because conventional terramechanics theory does not take into account the change in the soil density between grousers. However, in trapezoidal-shaped grousers, the presence of packing effect can increase the normal stress σ between the grousers and suppress sinkage of the wheel. As a result, the traveling resistance R_c is also considered to decrease. Furthermore, from Eqs. (5.1) and 5.3, it is expected that the first term of Eq. (5.2) increases, and optimization of the tradeoff relationship between F_s, F_g, and R_c can result in a high traveling performance.

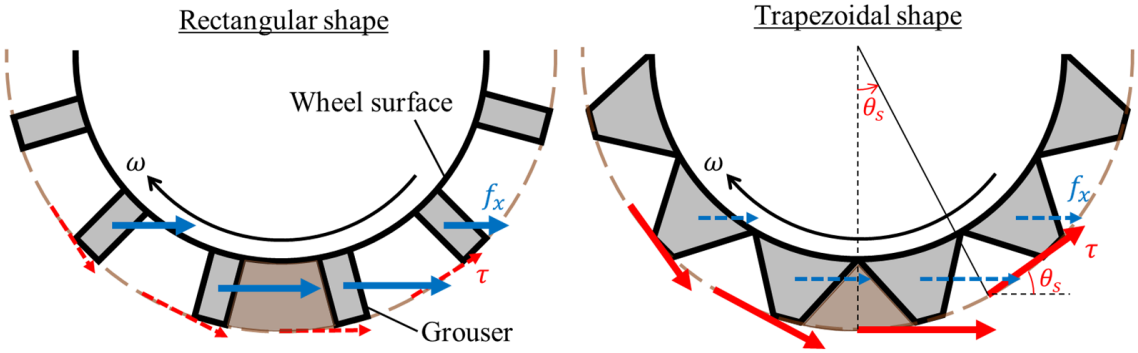

Figure 5.1: Schematic of driving force of grouser wheels: (a) rectangular and (b) trapezoidal grousers.

5.2.2 DEM analysis

A simple intrusion analysis was performed using DEM to confirm the presence of packing effect when trapezoidal-shaped grousers are used. In this study, the commercial software package Rocky DEM was used.

Fig. 5.2 shows the analysis models corresponding to one period of trapezoidal- and rectangular-shaped grousers. Here, to clearly extract the packing effect, the horizontal movement of particles was suppressed on the four side surfaces of the soil boundaries.

The dimensions of rigid intruding objects reflected to the wheel grousers, as described later, and the diameter of the particles was set according to the cumulative probability as shown in the Table 5.1. After configuring the soil particles, objects were set to vertically penetrate at a rate of 10 mm/s. In this study, the loose deposition condition was realized by incorporating free falling of particles from above. The density of particle media was 1581 $\mathrm{kg/m^3}$. Table 5.2 lists the parameters used in the DEM analysis.

Fig. 5.3 shows the relationship between the vertical reaction force and intrusion, where the intrusion is the length of the grouser tip penetrating from the initial soil surface. The figure also shows the variations in the volume fraction, obtained by dividing the particle volume filled between grousers by the space volume between grousers. The vertical reaction force of the trapezoidal grouser is larger than that of the rectangular groove for the same intrusion. This occurs as the increase in the volume fraction of the filling particles for the trapezoidal shape is quicker than that for the rectangular shape and causes a larger compaction with a smaller intrusion. The beginning of compaction corresponds to the inflection point of the volume fraction.

Notably, in Fig. 5.3, the intrusion volumes (volume of the grouser that penetrated the initial soil surface) of the objects are different, while the intrusions are equal.Therefore, as shown in Fig. 5.4, we arranged the relationship between the vertical reaction force and intrusion volume. Here, the intrusion volume was evaluated based on the surface of particle media before deformation. It is confirmed from figure that a higher penetration resistance occurs in the trapezoidal shape even in the same intrusion volume. That is, despite the low intrusion volume, the trapezoidal-shaped grouser exhibits a higher reaction force compared to that the rectangular type, indicating that high compaction of particle media is generated.

Thus, it can be hypothesized that the trapezoidal-shaped grouser exhibits packing effect during motion based on the above DEM analysis results.

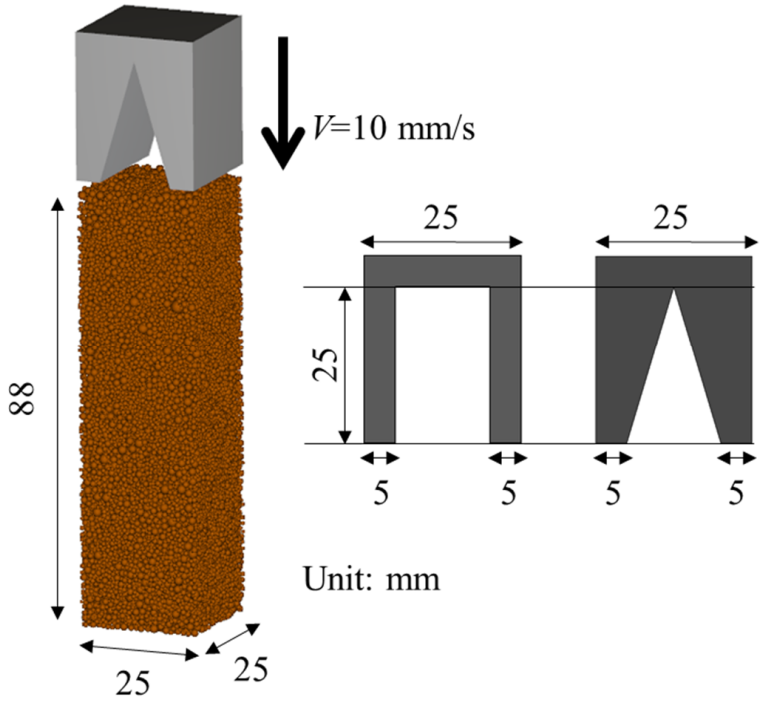

Figure 5.2: DEM analysis model corresponding to one period of the grousers.

Table 5.1: Particle size distribution of DEM analysis model

Particle diameter [m]	Cumulative probability [%]
2758	100.0
2449	99.9
2174	99.3
1930	96.2
1714	87.9
1521	76.0
1351	60.1
1199	43.5
1065	29.5
945.0	17.9
839.0	9.50
745.0	4.00
661.0	1.30
587.0	0.30
521.0	0.00

Table 5.2: Parameters for DEM analysis.

Materials		
Grousers		
Density	[kg/cm^3]	7850
Young's modulus	[GPa]	100
Poisson's modulus	[-]	0.3
Particles		
Particle density	[kg/cm^3]	2600
Young's modulus	[GPa]	0.1
Poisson's modulus	[-]	0.3
Rolling resistance	[-]	0.5
Materials interactions		
Particle – Particle		
Static friction	[-]	0.3
Dynamic friction	[-]	0.3
Restitution coefficient	[-]	0.3
Particle – Geometry (Grouser, Boundary)		
Static friction	[-]	0.0
Dynamic friction	[-]	0.0
Restitution coefficient	[-]	0.3

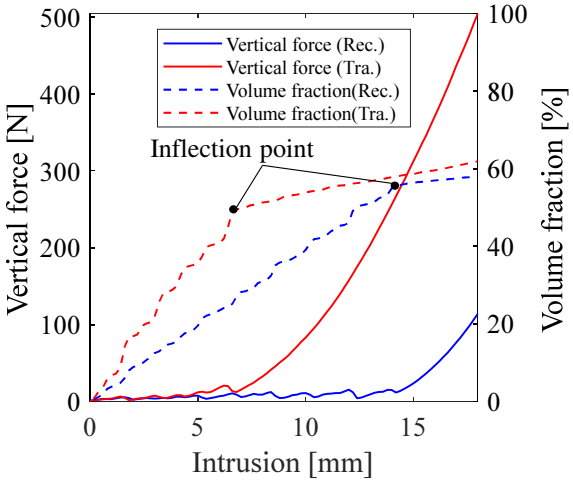

Figure 5.3: Variation in the vertical reaction force and volume fraction with the vertical displacement.

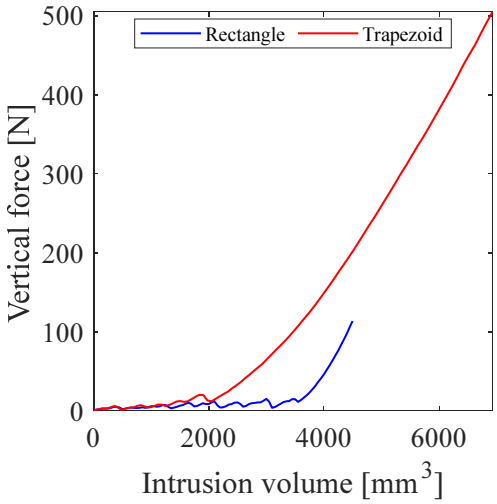

Figure 5.4: Variation in the vertical reaction force with intrusion volume.

5.3 Single-wheel experiment

A single-wheel traveling experiment was conducted using grouser wheels to obtain the traveling performance corresponding to each considered grouser shape.

5.3.1 Experimental setup

Fig. 7.4 shows an overview of the experimental rig. A soil vessel made of acrylic resin, with length, width, and height of 1500 mm, 400 mm, and 400 mm, respectively, was filled with the prescribed amount of sand, and a single-wheel traveled on it. The test bed comprised both a conveyance unit and a wheel-driving unit, and each can be driven by an independent motor. The translational velocity and angular velocity of the wheel were calculated based on data obtained using encoders mounted on the conveyance motor and wheel-driving motor. Thus, by controlling the translation velocity and the angular velocity of the wheel, an arbitrary slippage can be defined.

In this study, slippage is defined by the following equation:

$$s = 1 - \frac{V}{(D/2 + h_g)\,\omega} \tag{5.5}$$

where the radius pertaining to the angular velocity is obtained by adding the radius, $D/2$ of the wheel and the grouser height, h_g. In this study, we conducted forced-slip experiments for four different grouser wheel types, and the slippage was controlled by fixing the angular velocity, ω as 0.2 rad/s and varying the translational velocity, V. Further, the vertical load condition examined in this study is large enough to prevent a walking phenomenon of the grouser wheel.

The forces and torques generated by the wheel locomotion were measured using a six-axis force/torque sensor. Further, the wheel sinkage and traveling distance were measured using magnetic scales. The specifications of the sensors are listed in Table 7.1. The rated load of the force sensor is 200 N, while its detection sensitivity is 28 - 36 LSB/N. The accuracy of the magnetic scale is $\pm(80 + 15\ \mu\mathrm{m/m}\times L_s)$ using the scale length L_s.

In the experiment, the vessel of the single-wheel test bed was filled with Toyoura sand. The soil density was maintained at approximately 1,488 kg/m^3 in each traveling test. Fig. 5.6 shows images of the four types of grouser wheel. The grousers attached to the wheels were fabricated using a 3D printer. The resin material was Accura SL7870.

The dimensions of the wheels are listed in Table 5.4. The numbers of grousers were 12 and 18. The wheel specifications were determined according to previous studies [6, 41, 46]. The same thickness was used at the tip of the grousers, t_g for the four types of wheels. Note that the evaluation of the effect of grouser thickness is beyond the scope of this study.

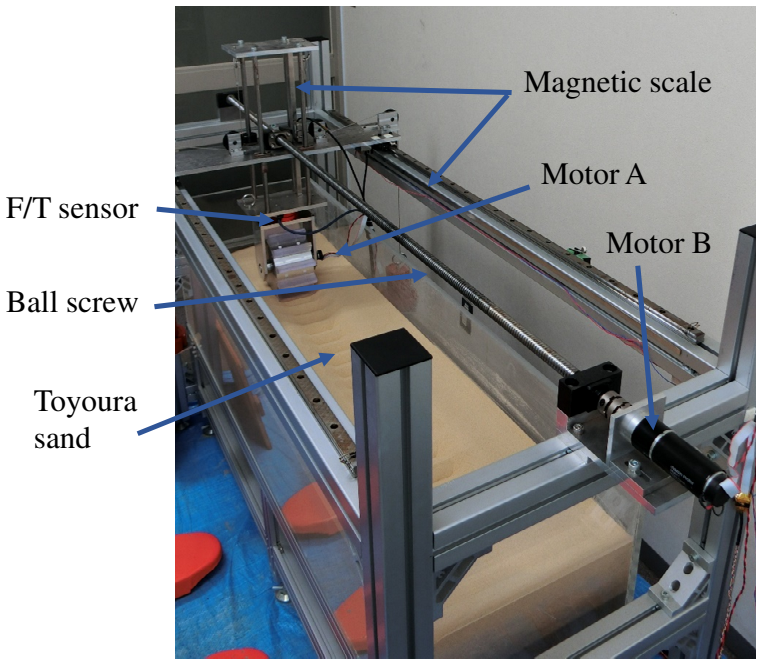

Figure 5.5: Experimental setup of single-wheel traveling apparatus. In the experiment, the translation and angular velocities were controlled under constant wheel load.

Table 5.3: Specifications of sensors.

Motor A	Maxon motor RE-25 10 W
Motor B	Maxon motor RE-40 150 W
Magnetic scale	HIWIN PS-A
F/T sensor	Wacoh-tech DynPick [WEF-6A200-4]

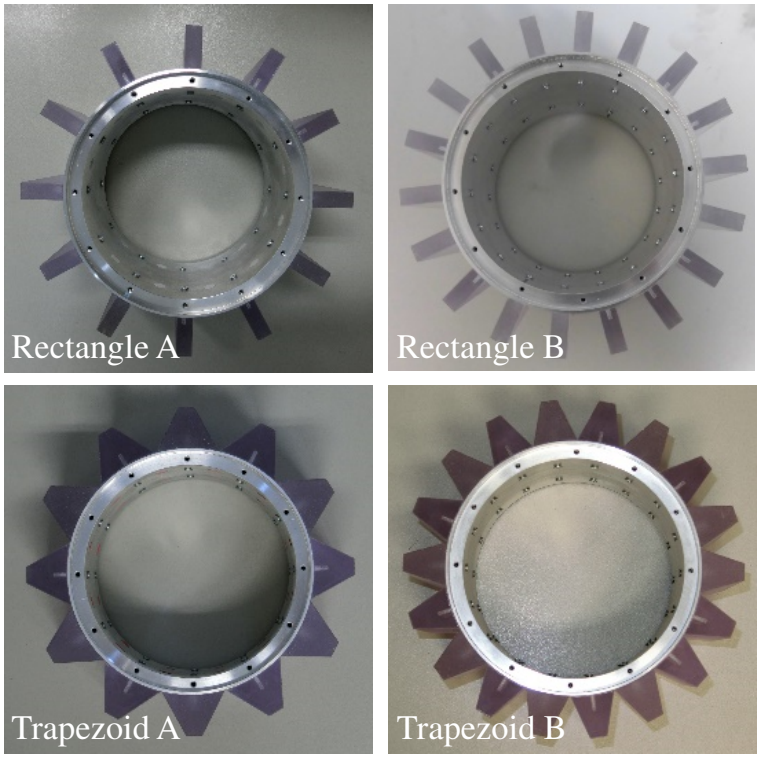

Figure 5.6: Grouser wheels utilized in this study.

Table 5.4: Specifications of wheels.

			Rectangle		Trapezoid	
			A	B	A	B
Diameter	D	[mm]	150			
Width	b	[mm]	100			
Grouser height	h_g	[mm]	25			
Thickness of grouser tip	t_g	[mm]	10			
Number of grousers	N_g	[-]	12	18	12	18
Vertical load	W	[N]	150	150	158	159

5.3.2 Experimental results

In this study, we conducted experiments at slippage values of 0.0, 0.1, 0.3, 0.5, and 0.7. Measurements were conducted three times at each slippage condition. Figs. 5.7 (a) and 5.8 (a) show the variations in the drawbar-pull as a function of the traveling distance, whereas the results for sinkage are shown in Figs. 5.7 (b) and 5.8 (b). In all the conditions examined, the drawbar-pull in the steady rolling state tends to increase as the slippage increased, and then tends to saturate at larger slippage values. Further, it was confirmed that the trend of increase in sinkage corresponding to slippage is the same in all conditions because the shearing action of the sand by grousers per unit traveling distance increased with slippage, whereas the traveling resistance and contact area increased with sinkage. The trends obtained in the present experiment agree with those reported in the study by Sutoh et al. (2012) [76]. Fig. 5.9 shows an image of the terrain surface after the passage of a wheel. As the wheel travels, sand becomes packed between the grousers and is carried rearward. Moreover, the rut width is almost the same as that of the wheels, and the flow of sand to the sides cannot be confirmed. Thus, it is appropriate to restrain the movement of the sand in the lateral direction in the DEM penetration test.

Figs. 5.10 (a) and 5.10 (b) show the steady-state values of the coeffi-

cient of traction and sinkage against slippage, respectively. The coefficient of traction was computed by dividing the drawbar-pull by a constant wheel load. From the figures, it can be confirmed that the steady-state coefficient of traction is slightly lower for trapezoidal-shaped grousers, but the difference between the two cases is insignificant. On the other hand, it can be confirmed that on average, the sinkage of trapezoidal-shaped grousers is suppressed by 30% in wheels with 12 grousers and by 35% in wheels with 18 grousers compared to those of rectangular grousers.

These results indicate that a trapezoidal-shaped grouser can exhibit traction similar to or slightly lower than that of rectangular grousers, while suppressing sinkage. This implies that a trapezoidal-shaped grouser can travel while preventing sinking—which is the factor responsible for making wheels become stuck—thereby enhancing the traveling performance.

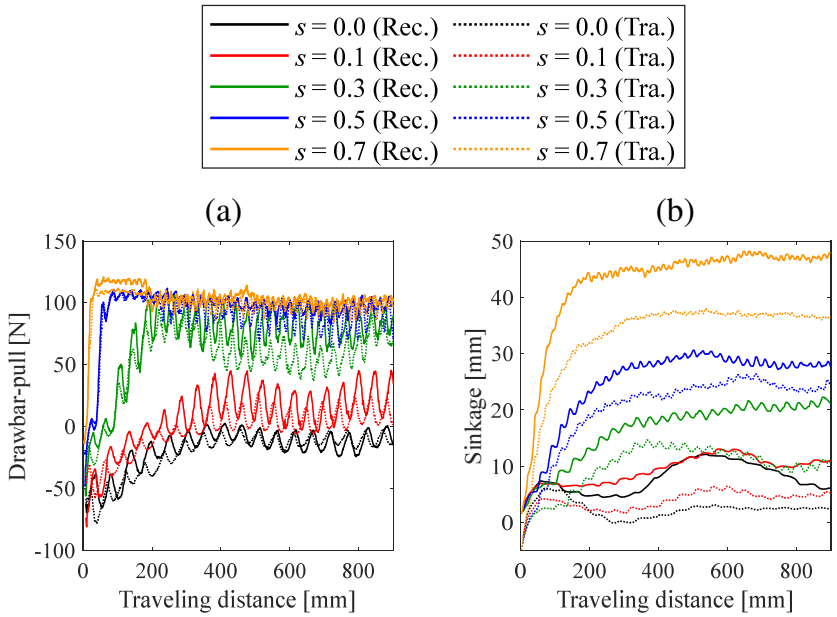

Figure 5.7: Variations in drawbar-pull and sinkage with traveling distance for wheels with 12 grousers (Rectangle A and Trapezoid A): (a) Drawbar-pull, (b) Sinkage.

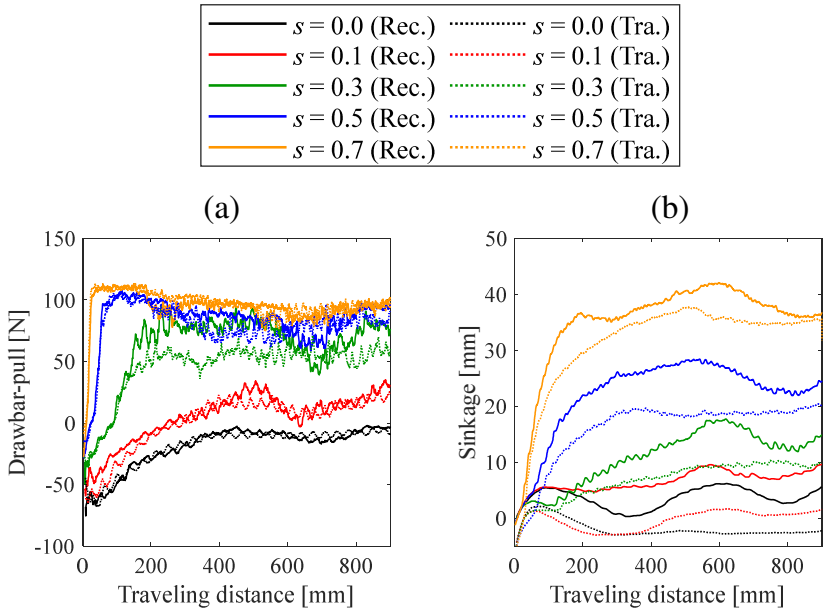

Figure 5.8: Variations in drawbar-pull and sinkage with traveling distance for wheels with 18 grousers (Rectangle B and Trapezoid B): (a) Drawbar-pull, (b) Sinkage.

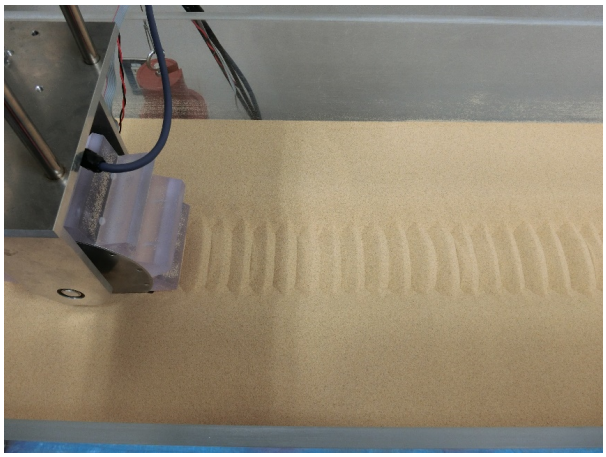

Figure 5.9: Terrain surface after the passage of a wheel.

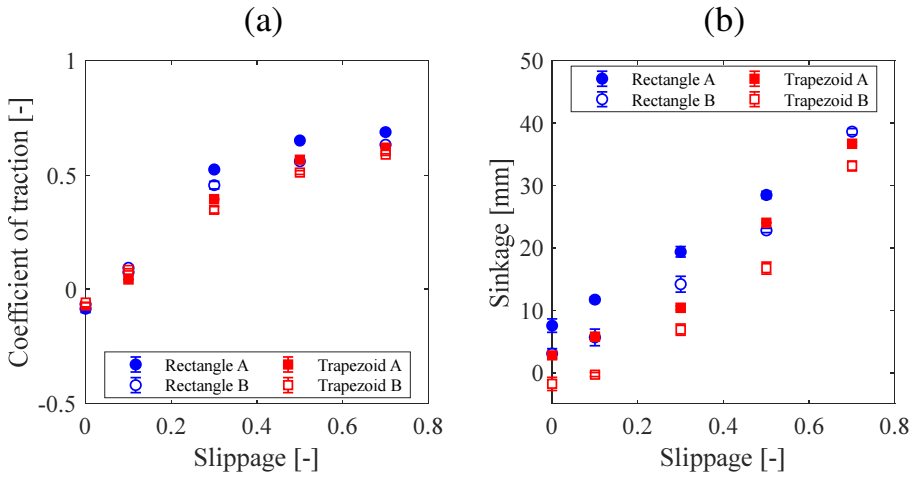

Figure 5.10: Relationship between traveling performance and slippage obtained through experiment: (a) Coefficient of traction, (b) Sinkage. Each plot is evaluated by the average value of steady rolling state.

5.4 Trafficability analysis based on terramechanics theory

We performed trafficability analysis using terramechanics theory to verify the hypothesized effectiveness of the packing effect demonstrated by trapezoidal-shaped grouser. In this section, application of RFT to traveling analyses of the four types of grouser wheels is subsequently described.

5.4.1 Analysis results and discussion

Traveling analysis was performed based on the RFT under the conditions assumed for the single-wheel traveling experiment described in Section 3 (that is, under a constant wheel load and forced-slip condition). As presented in Table 5.4, the dimensions of the wheels were the same as those in the experiment (see Fig. 5.6). The scale factor ζ was set as 1.5 N/cm^3 based on linear approximation of the plate intrusion test using the same soil condition

as the single-wheel experiment. The grouser part was discretized using 30 plates, whereas the wheel part was discretized considering intervals of 0.01 rad.

Fig. 5.11 shows the variations in drawbar-pull with the traveling distance obtained from RFT analysis. It can be observed from the figure that the drawbar-pull fluctuates owing to the influence of the grousers. Fig. 5.12 also shows the results obtained using RFT analysis, in which the lines correspond to the average coefficient of traction in steady state for each slippage. From the figure, it can be confirmed that the coefficient of traction increases with increase in the slippage under all conditions. The RFT is based on the principle of superposition and does not take into account the influence of the grouser interval. Therefore, a higher number of grousers increases the drawbar-pull. Meanwhile, a comparison of the coefficient of traction for each wheel shape indicates that there is no significant difference in the values for rectangular-shaped grousers. However, the values for trapezoidal-shaped grousers were lower than those of rectangular-shaped grousers, particularly at higher slippage because the shape of the grousers affects the resistive stress distribution.

In this study, the scale factor was fixed at 1.5 N/cm^3. However, variations and errors in the scale factor are assumed to exist in reality. According to Li et al., error occurs in the analysis result even when using the scale factor obtained from a plate test [1]. Therefore, this study confirmed the effect of changes in the scale factors on the analysis results. Fig. 5.13 shows the relationship between the slip ratio-coefficient of traction relationship for a wheel with 12 grousers as the scale factor varies from 1.0 N/cm^{3}to 2.5 N/cm^3. The weak dependence of the results on the scale factor does not affect the above discussion.

To carry out a more detailed investigation, we created trajectories of α_x for the motion of a wheel on the stiffness distribution map. Figs. 5.14 and 5.15 show the trajectory made by two grouser wheels at slippage values of 0.1 and 0.5, respectively. In this case, we adopted rectangular wheel A and

trapezoidal wheel A (see Fig. 5.6), and the values of α_x correspond to the midpoint of the grousers as indicated by the black dots in the figure. The trajectory of α_x is plotted with β and γ using solid circles when β and γ follow the definition in Fig. 2.4 (a), whereas hollow circles are used when the parameters follow the definition in Fig. 2.4 (b). Note that when β and γ exhibit discontinuous behavior, the order of their transitions is indicated in the figure by numbers (1) and (2).

As shown in Fig. 5.14, when the slippage is 0.1, β and γ follow the definition in Fig. 2.4 (b) for any considered wheel. The trajectory of the rectangular-shaped grouser seems to shift from (1) to (2) after β reaches $-\pi/2$ (i.e., the plate is vertical). In contrast, in the case of the trapezoidal-shaped grouser, the grouser is lifted from the ground before β inverts, and the trajectories are continuous. This is because the inclination of the trapezoidal grouser offsets β in the positive direction.

Furthermore, as shown in Fig. 5.15, the behavior is the same as the previous one (i.e., the trajectory shifts from (1) to (2)) in which β reverses only in the case of the rectangular-shaped grouser, even for a slippage of 0.5. However, it can be observed that β and γ follow the definition in Fig. 2.4 (a) in both wheels (rectangular A and trapezoidal A) because the translational velocity decreases with increase in the slippage, such that the velocity vector, γ faces the rear side. Notably, the integration of α_x over the trajectory in the case of the rectangular-shaped grouser is larger than that of the trapezoidal-shaped grouser. Therefore, the drawbar-pull of the rectangular-shaped grouser is high in the high slippage regime.

It should be noted that compaction and movement (shearing) of soil are not taken into consideration in the RFT. Therefore, the results shown in Fig. 5.12 reflect only the resistive force of the grouser in the soil; details of these are shown in Figs. 5.14 and 5.15. In the analysis results obtained using RFT, it was predicted that the drawbar-pull drastically reduces in trapezoidal-shaped grousers than in rectangular-shaped grousers. Therefore, if there is no packing effect, the drawbar-pull in the experimental results

shown in Fig. 5.10 should also be considerably lower when trapezoidal-shaped grousers are used. However, the fact that a decrease in the drawbar-pull of the trapezoidal-shaped grouser is smaller and the sinkage is suppressed demonstrates, paradoxically, the existence of the packing effect. Thus, the hypothesized effectiveness of the packing effect owing to the use of trapezoidal-shaped grousers is verified using the three terramechanics approaches, namely, the DEM analysis, wheel experiment, and terramechanics theory.

Finally, we believe that a novel design taking the packing effect of a grouser wheel into consideration can be realized by rationally optimizing the shape and number of trapezoidal-shaped grousers based on several terramechanics approaches.

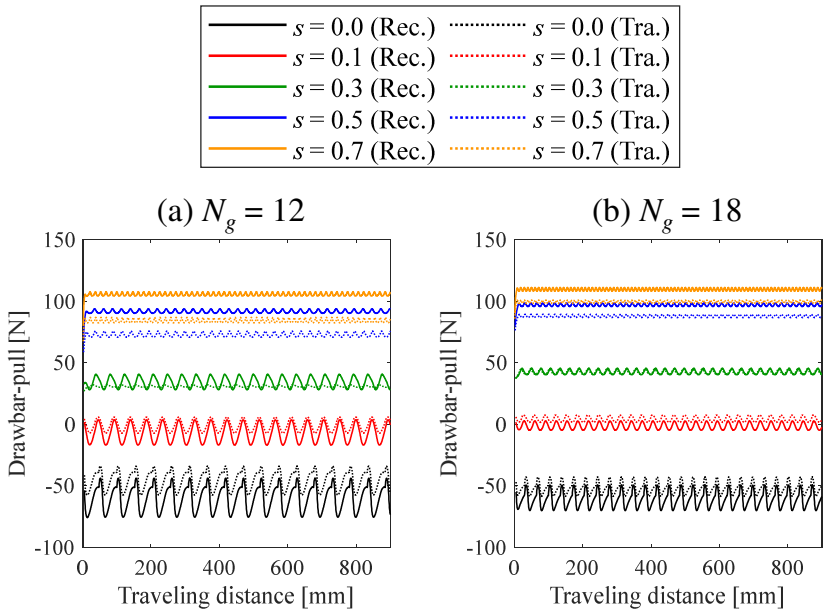

Figure 5.11: Variation of drawbar-pull with traveling distance under different slippage conditions:(a)$N_g = 12$,(b)$N_g = 18$.

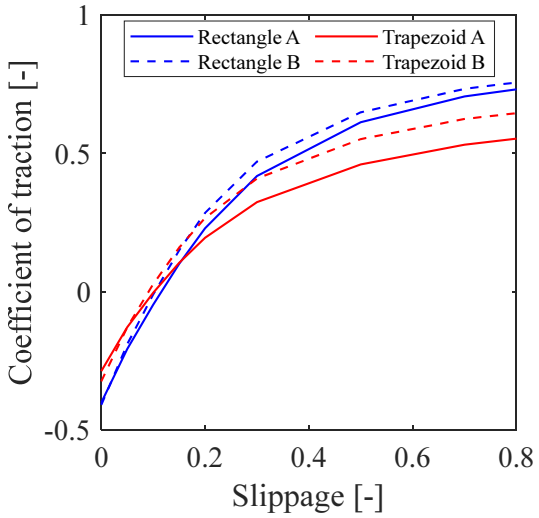

Figure 5.12: Relationship between coefficient of traction and slippage obtained through RFT analysis.

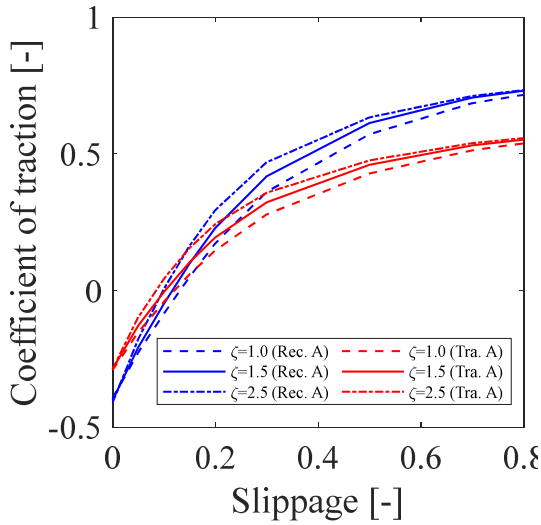

Figure 5.13: Relationship between coefficient of traction and slippage as the scale factor is changed.

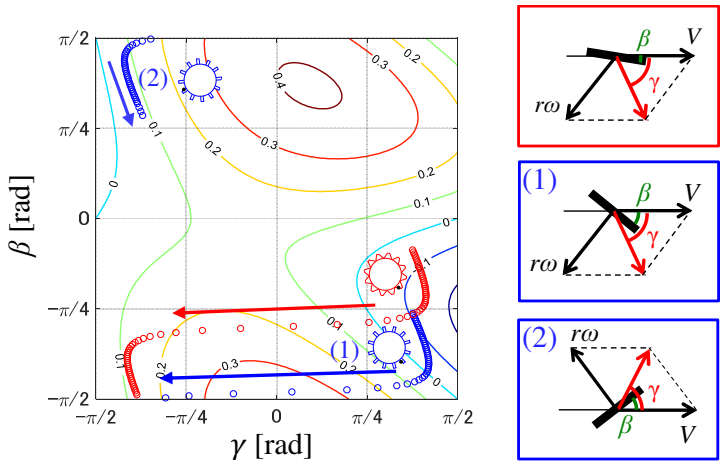

Figure 5.14: Trajectories of α_x during traveling on stiffness distribution map shown in Fig. 5.11 ($s = 0.1$).

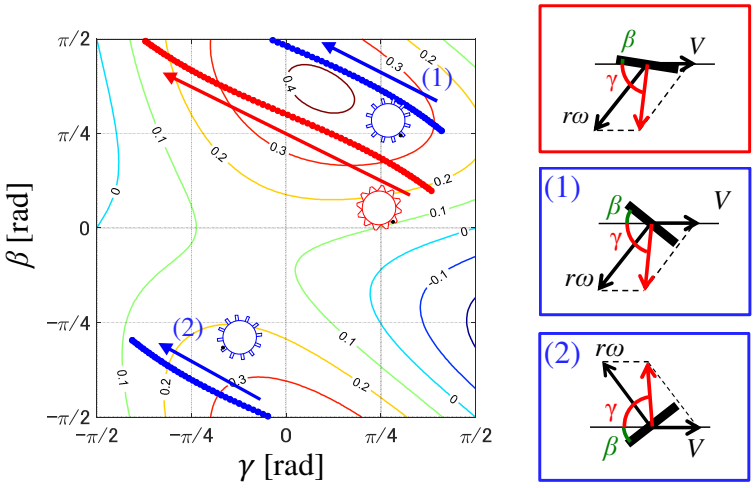

Figure 5.15: Trajectories of α_x during traveling on stiffness distribution map shown in Fig. 5.11 ($s = 0.5$).

5.4.2 Effect of equivalent radius

The analyses in this study were performed using a constant grouser height and wheel diameter. However, differences in wheel cross-sectional areas and circumferences do not allow a fair comparison in terms of the ground pressure. Therefore, this study confirmed the effect of varying the grouser height and the wheel diameter on the locomotion performance, in the grouser height h_g and wheel diameter D such a way that the cross-sectional area and circumference are equivalent. Tables 5.5 and 5.6 show the wheel dimensions when the cross-sectional area and circumference are aligned. A locomotion test was conducted using a wheel with the shape shown in Table . Fig. 5.16 shows the obtained relationship between slippage and the coefficient of traction relationship. The qualitative behavior appears to be independent of the conditions and does not affect the above consideration. On the other hand, as the grouser height decreases, the coefficient of traction also tends to decrease. This is due to the decrease in the resistive force that occurs in the grouser. By changing the wheel dimensions, the ground-contact area and the penetration volume can be made uniform, but the grouser height cannot be set fairly . Arguably, the wheel shape must be examined from various viewpoints while understanding the above relationship.

Table 5.5: Wheel specifications (Wheel A).

		Rectangle A			Trapezoid A
		Normal	Equivalent length	Equivalent area	Normal
D	[mm]	150	162	169	150
h_g	[mm]	25.0	12.6	15.7	25.0

Table 5.6: Wheel specifications (Wheel B).

		Rectangle B			Trapezoid B
		Normal	Equivalent length	Equivalent area	Normal
D	[mm]	150	157	170	150
h_g	[mm]	25.0	17.5	14.9	25.0

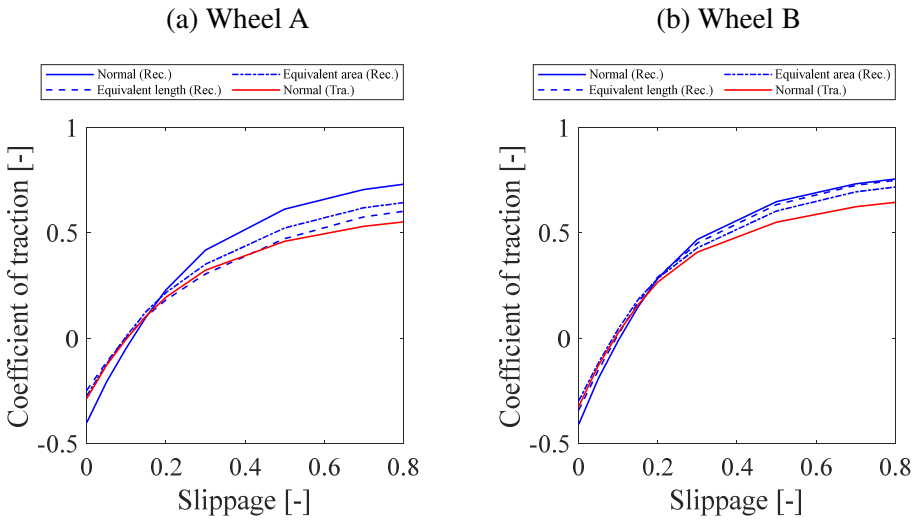

Figure 5.16: Relationship between coefficient of traction and slippage, as a function of the grouser height and wheel diameter, for (a) Wheel A and (b) Wheel B.

5.5 Conclusion

In this study, we investigated the effect of grouser shape on the traveling performance of a rigid wheel. First, an intrusion test corresponding to part of the wheel was conducted using DEM to verify the existence of packing effect when trapezoidal-shaped grousers are used. It was confirmed that the particles between trapezoidal grousers were strongly compressed. Next, single-wheel traveling experiments were conducted to determine the traveling

performance of four types of grouser wheel. The results show that sinkage was suppressed when the trapezoidal-shaped grouser was used although rectangular grouser exerts slightly greater traction. In addition, traveling analysis was performed using the RFT to verify that improvement in the traveling performance is as a result of packing effect owing to the use of the trapezoidal-shaped grouser. A comparative analysis of the two grouser shapes indicate that the drawbar-pull exerted by the trapezoidal-shaped grouser was considerably lower than that of the rectangular-shaped grouser. The difference in the results obtained from experiments and RFT analysis, paradoxically, suggests that the drawbar-pull is improved owing to packing effect as packing effect is not considered in the RFT.

This study confirmed that a trapezoidal grouser improves the locomotion performance as a result of the packing effect. However, depending on the design goal, a trapezoidal grouser is not always optimal. The experimental and terramechanics analysis results demonstrated that a rectangular grouser produces a large resistive force and that the traction coefficient is slightly large. Arguably, the choice and combination of shapes must be tailored as required, e.g., to suppress sinkage or to increase traction . Moreover, the trapezoidal grouser had a much larger cross-sectional area than the rectangular grouser. This suggests that the high packing density results from the larger intrusion volume. Therefore, additional experiments must be conducted, where the intrusion volume is the same for each wheel, to verify the effectiveness of a trapezoidal grouser. Nonetheless, a trapezoidal-shaped grouser, for which the strong packing effect has not been considered to date, can be one of effective approaches to improve the locomotion performance of a rigid wheel.

We plan to optimize the grouser shape for a variety of purposes in the future. In subsequent optimization, we will focus not only on the shape but also the height and interval of the grousers using several terramechanics approaches. In addition, we plan to investigate when packing effect effectively occurs, because it is also important for optimization. Furthermore, we believe that the tradeoff relationship between straight trafficability and turning

performance should be further investigated.

In addition, although vehicle traveling analysis and wheel shape studies were conducted by single-wheel traveling analysis, many of the terrain surface models used for this are simple. The slope targeted in the climbing analysis performed in Chapter 3 was a plane, and the flat terrain surface was targeted in the terramechanics analysis performed in this chapter. However, the terrain surface in the extreme environment represented by actual lunar / planetary exploration and disaster sites has complicated shapes and properties. In the future, terramechanics analysis using a field model that inherits these complicated terrain surface information is ideal.

6 Proposal of multi-stage analysis method

6.1 Introduction

As mentioned in Chapter 1 and Chapter 5, it is indispensable to create a field model that inherits the information of the target terrain surface in detail.Therefore, in this section, using the simulation of wind-blown ripple formation as an example, a modeling method of a terrain field, which uses the soil surface geometry, is proposed for terramechanics analysis. In addition, in order to propose a method for multi-stage analysis for achieving seamlessness with terramechanics analysis, we demonstrated the systematic analysis of single wheel locomotion using numerically created sand ripple fields. For single wheel locomotion analysis, we adopted the resistive force theory (RFT), which has attracted attention in recent years [1,37,38,83]. RFT can be employed to evaluate the resistive stress generated in an arbitrarily shaped object moving in granular media. It has been demonstrated that RFT is suitable for the traveling analysis of a legged mobile robot [1]], and this method has been employed to evaluate the force generated in wheels [37,38,83]. We adopted the programming language MATLAB and its numerical computing environment to perform the simulations of wind ripple formation and wheel locomotion. The multi-stage analysis method proposed in this study can be used for simulations in extreme environments such as planetary surfaces, deserts, and disaster sites, where sensing is difficult.

6.2 Simulation of ripple formation by wind-blown sand

This section presents the simulation of the formation of ripple patterns by wind-blown sand based on the cellular automaton model proposed by Nishimori and Ouchi [17] as the first stage of seamless analysis. The model is a discrete model in space and time with a continuous field variable representing the averaged surface height at each cell. The simulation corresponds to a small-scale model, and a ripple pattern is spontaneously formed by the jump-

ing process of sand grains, known as saltation, when the wind force exceeds a critical value.

6.2.1 Model

It is assumed that the wind ripple pattern is created by two processes, namely, saltation and creep of sand grains [17]. When sand grains on the surface are released into the air under strong wind, the grains are accelerated by the wind. Further, the grains impact on the surrounding grains, releasing them into the air. As a result, sand in a certain area jumps and moves to another area. The dynamics of the saltation process is expressed as follows:

$$\begin{aligned} h'_{i,j} &= h_{i,j} - q \\ h'_{i+\Delta i,j} &= h_{i+\Delta i,j} + q \end{aligned} \tag{6.1}$$

where h is the height of the sand surface at each area (cell of the ith row and the jth column), and q is the transferred height. Eq. (6.1) indicates that when wind blows in the ith direction, sand with a height of q in cell position ($x_{i,j}$, $y_{i,j}$) is released, and is added to another cell position ($x_{i+\Delta i,j}$, $y_{i+\Delta i,j}$). The subscript Δi is the flight length at one saltation, and is expressed using parameters l_0 and b. Using the floor function, Δi is given as follows:

$$\Delta i = floor\left(\frac{l_0 + bh_{i,j}}{dx}\right) \tag{6.2}$$

where l_0 is a control parameter proportional to the wind force, b is a constant related to the average wind velocity a grain experiences in flight, and dx is the lattice length in the ith direction (x direction) of a single cell.

Meanwhile, moving (rolling) to a nearby region when grains cannot maintain their position due to a steep surface gradient is called creep. The dynamics of creep is described by the following equation.

$$h'_{i,j} = h_{i,j} - rh_{i,j} + \frac{r}{6}H_{cross} + \frac{r}{12}H_{diag} \tag{6.3}$$

Eq. (6.4) has the following meanings:

- The sand hill in a certain cell is relaxed by gravity at a speed proportional to the convexity of the sand surface and receives inflow from adjacent cells at the same time. Here, r is the rate of relaxation.
- The distribution of inflow is $rh/6$ from perpendicular crossing cells and $rh/12$ from diagonally adjacent cells.

The inflow term from the perpendicular directions, H_{cross}, and the inflow term from the diagonal directions, H_{diag}, are given as follows:

$$\begin{aligned} H_{\text{cross}} &= h_{i+1,j} + h_{i-1,j} + h_{i,j+1} + h_{i,j-1}, \\ H_{\text{diag}} &= h_{i+1,j+1} + h_{i+1,j-1} + h_{i-1,j-1} + h_{i-1,j+1}. \end{aligned} \tag{6.4}$$

It was assumed that creeping action occurred when the height difference between adjacent cells exceeds the angle of repose.

6.2.2 Analysis results

In the numerical simulation, the dynamics of saltation and creep are evaluated at each time step, and a ripple pattern is formed by repeated calculation. In this study, analysis was performed under five conditions labeled A - E, as listed in Table 6.1. Here, dy is the lattice length of a single cell in the jth direction and was set to be the same as dx. The number of repeated calculation steps is 30000 for each condition. The length of the analyzed soil surface is 1500 mm (row i direction), and the width is 400 mm (column j direction).

Fig. 6.1 shows the variation of the soil surface geometry with the number of repeated steps k, where condition C in Table 6.1 was used. The soil surface shape is irregular at $k = 1$ as the initial configuration of the height of the cells was set using random numbers. At $k = 1000$, the soil surface is close to being flat due to creeping action, and the formation of wind ripples is initiated due to saltation. Then, the wind ripple pattern starts becoming clear ($k = 5000$), and eventually steady state is reached ($k = 30000$). In this study, the wind ripple pattern at $k = 30000$ was used as the steady state and

was reflected in the terrain field modeling for terramechanics analysis, which will be presented later.

Next, the effect of each parameter on wind ripple formation is verified. As presented in Table 6.1, we examined the effects of l_0 and q, which affect the dynamics of saltation. Fig. 6.2 shows the wind ripple patterns under conditions A - E in steady state. As shown in conditions A, B, and C of Fig. 6.2, l_0 affects the wind ripple interval because the distance of saltation changes. Meanwhile, it was verified that variations in q affect the height of the ripples. In the case of condition D with a small q, the ripple pattern is unclear, whereas it becomes quite clear in condition E, which has a large q. It should be noted that the distributions of the initial height using random numbers were the same for conditions A - E.

Table 6.1: Simulation conditions of wind ripple formation. The angle of repose is 30 deg.

		A	B	C	D	E
l_0	[mm]	1.0	100	10		
q	[mm]	0.10			0.025	0.40
b	[-]	0.20				
r	[-]	0.20				
dx, dy	[mm]	5.0				

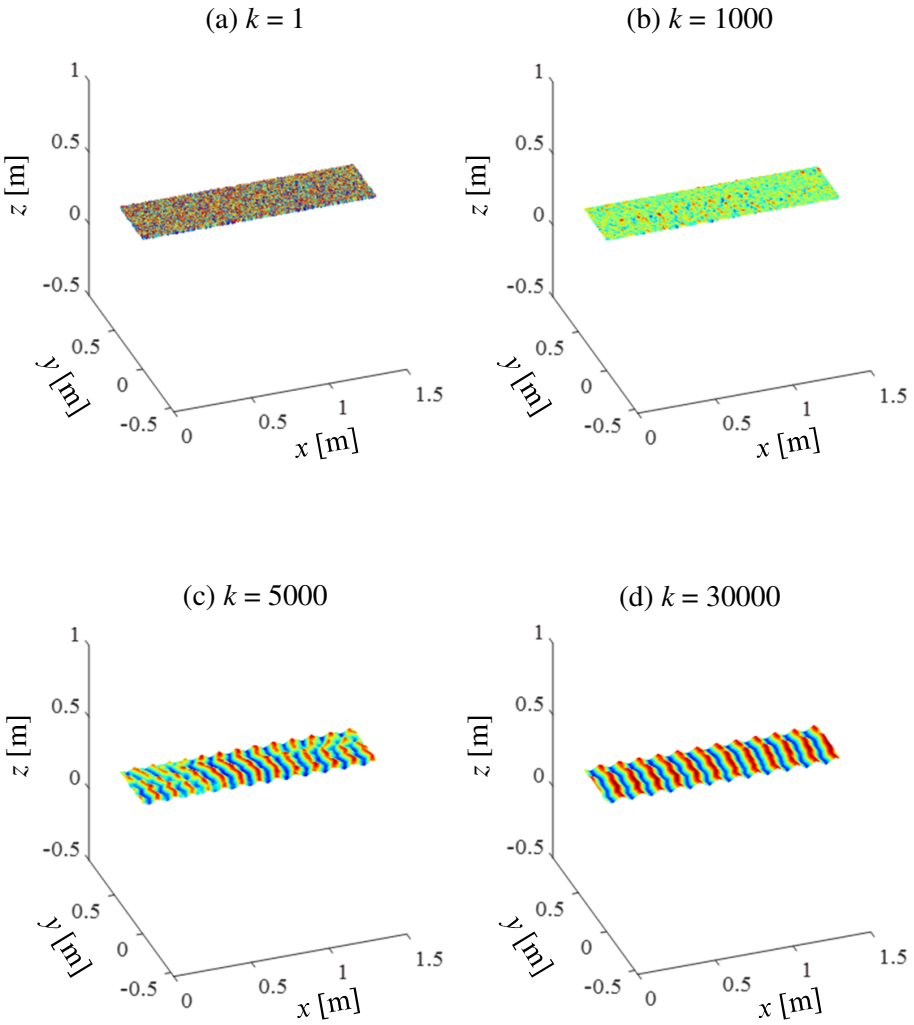

Figure 6.1: Variation of soil surface geometry with number of repetition steps k, where the condition C in Table 6.1 was adopted. The directions of row i and column j correspond to the x and y coordinates, respectively. The unit of each axis is in m.

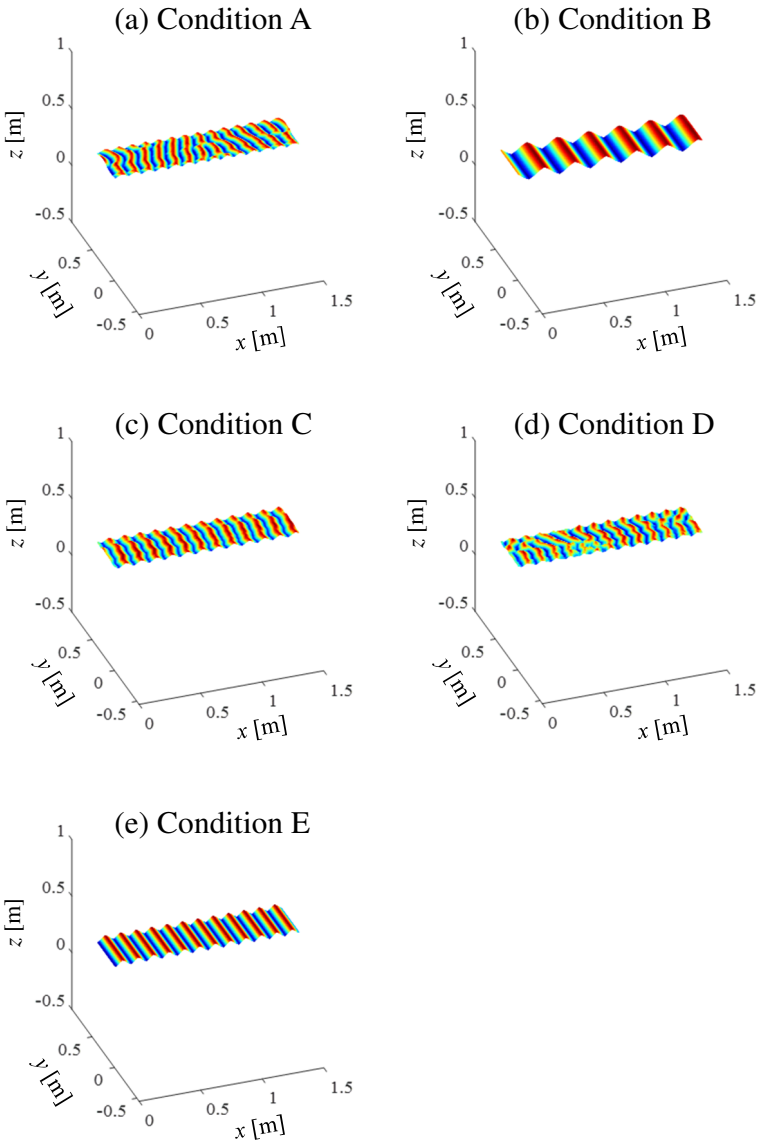

Figure 6.2: Wind ripple patterns under conditions A - E in steady state ($k = 30000$). The unit of each axis is in m.

6.3 Analysis of single wheel locomotion on wind ripples

Single-wheel traveling analysis is performed using the created terrain surface model.In the wheel locomotion analysis, the wheel radius, width, and load were set to $R = 100$ mm, $B = 100$ mm, and $W = 120$ N, respectively, unless stated otherwise. Further, the rotational angular velocity, ω, which is a source of driving for the wheel, was set to 0.5 rad/s. The kinetic characteristics of the wheels are sequentially evaluated based on the equation of motion. A traction load P is applied to the wheels, which is fixed at $P = 15$ N.In addition, an important indicator of off-road trafficability is the slip ratio, s, which is defined as follows:

$$s = 1 - \frac{v}{R\omega} \tag{6.5}$$

Here, $s = 1.0$ corresponds to the wheel being stuck. This slip ratio is used to evaluate the external force by RFT.

In terms of the terrain field modeling, it is necessary to set the soil parameters in addition to the surface topography. In RFT, the scale factor is the only soil parameter, and thus we set $\zeta = 1.0$, assuming soft sandy soil. Fig. 6.3 shows the relationship between the drawbar-pull and the slip ratio when the wheel specifications already described and $\zeta = 1.0$ were used. Here, to determine the characteristics of the analysis conditions, we performed the wheel traveling analysis on a flat road surface in advance. It can be confirmed that the drawbar-pull of the wheel increases as the slip ratio increases, which is consistent with results in existing reports [35, 51].

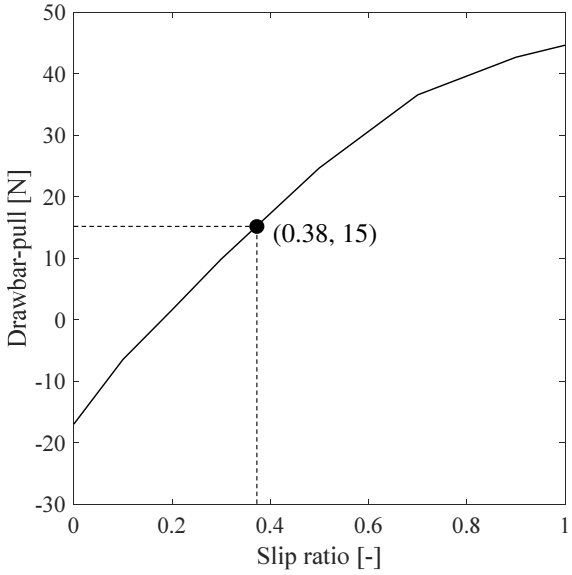

Figure 6.3: Relationship between drawbar-pull and slip ratio, where $R = 100$ mm, $B = 100$ mm, and $W = 120$ N.

6.3.1 Trafficability characteristics of flat road surface

First, analysis results of wheel locomotion on a flat road surface are presented. Here, the wheel travels straight in the x direction, which is achieved by using a constant rotational angular velocity, ω. Fig. 6.4 (a) shows the trajectory of the wheel center, whereas Fig. 6.4 (b) shows the variation of the slip ratio and the travel distance with the elapsed time. It can be observed from the relationship shown in Fig. 6.3 that the slip ratio corresponding to a towing load of $P = 15$ N is approximately 0.38, indicating that the wheel shows steady traveling while balancing. In addition, after the drawbar-pull, F_x exerted by the wheel balances with the towing load, P, a constant velocity linear motion is achieved.

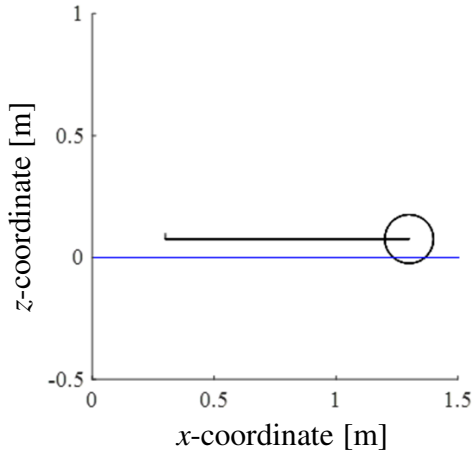

(a)

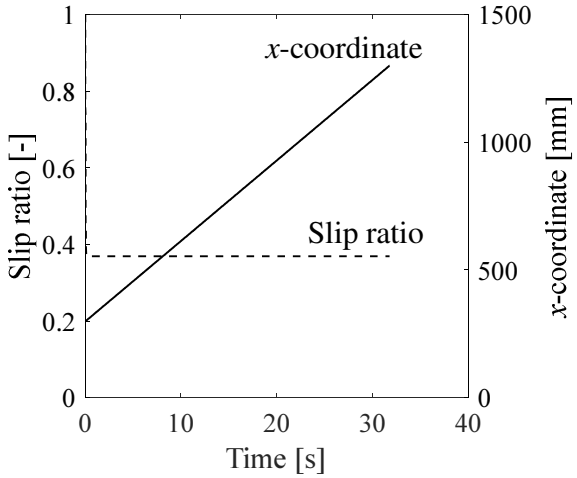

(b)

Figure 6.4: Terramechanics analysis results for a flat road surface: (a) trajectory of the wheel center; (b) variation of the slip ratio (dashed line) and the x-coordinate of the wheel centre (solid line) with the elapsed time.

6.3.2 Trafficability characteristics of wind ripples

Next, the wheel behavior when traveling in the x direction on terrain fields obtained by wind ripple simulation is presented. Here, the traveling position of the wheel in the y direction is the center of the field.

Fig. 6.5 (a) shows the trajectory of the wheel center obtained by terramechanics analysis using field C (Fig. 6.2 (c)). Fig. 6.5 (b) shows the variation of the slip ratio and the traveling distance with the elapsed time. It can be observed from the figures that the wheel repeatedly moves up and down according to the undulation of the terrain field. In addition, the slip ratio and the traveling speed of the wheels also vary according to the surface undulations. Fig. 6.6 shows the stress distributions at t_1 and t_2 depicted in Fig. 6.5. The lines represent the stress vector on the wheel surface. The vertical blue lines represent σ_z; the red and orange lines represent σ_x acting in the traveling direction and its opposite direction, respectively. At time t_1 when the slip ratio reaches its maximum value, the traveling resistance due to the front slope is large, and the slip ratio increases to produce drawbar-pull to overcome this (Fig. 6.6 (a)). On the other hand, time t_2 is when the slip ratio reaches its minimum value. At this time, there is minimal traveling resistance, as the descent along the slope of the ripple is initiated, and the horizontal stress required for driving is small (Fig. 6.6 (b)). Therefore, it is possible to move forward even at a low slip ratio.

In addition, we will examine the trafficability characteristics of terrain fields A, B, D, and E using different parameters in the wind ripple simulation. Figs. 6.7 (a) and 6.7 (b) show variations of the slip ratio and the traveling distance with the elapsed time for each terrain field condition. It can be observed from the figure that the characteristics of the slip ratio and the traveling distance vary according to the terrain fields. In particular, as shown by the blue and black lines in Fig. 6.7 (a) and (b), the traveling characteristics (X- displacement and slip ratio) are not periodic on the irregular fields with undeveloped wind ripples such as the conditions A and D. On the other hand, the wheel becomes stuck in terrain field B (Fig. 6.7 (c)). The reason is that

the traveling resistance due to ripples in front of the wheels is quite large, and it was difficult to produce drawbar-pull to drive forward under the wheel specification used in the analysis.

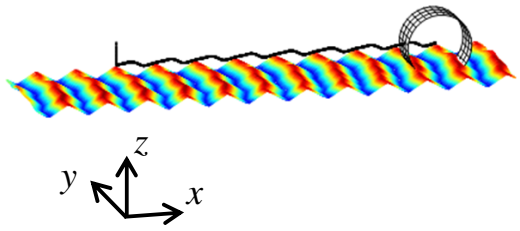

(a)

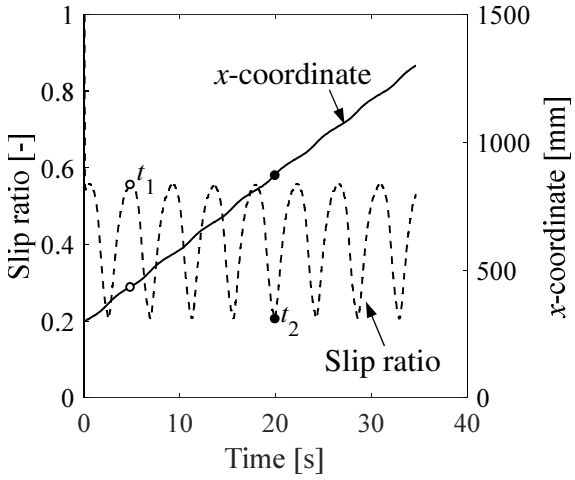

(b)

Figure 6.5: Terramechanics analysis results for Ground C: (a) trajectory of the wheel center; (b) variation of the slip ratio (dashed line) and the x-coordinate of the wheel centre (solid line) with the elapsed time.

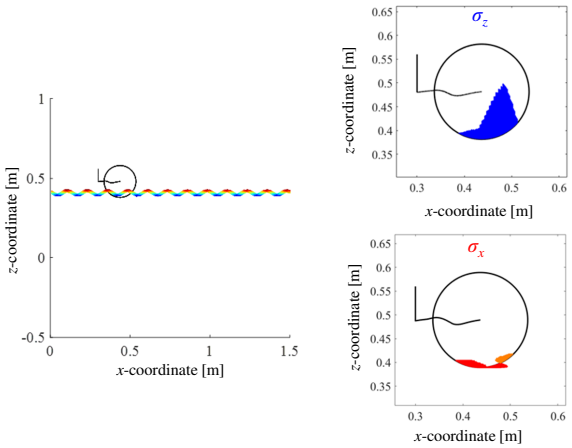

(a) $t = t_1$

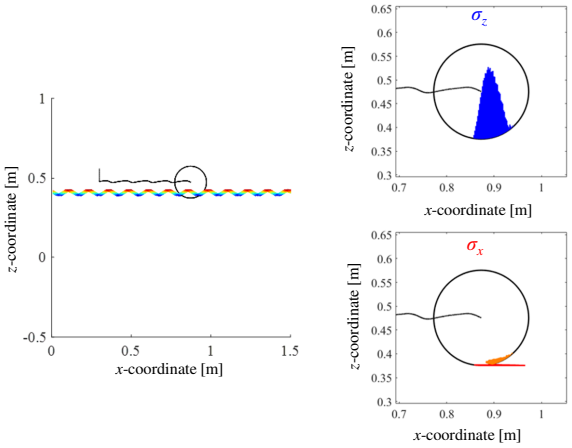

(b) $t = t_2$

Figure 6.6: Stress distribution on the wheel surface for field C: (a) $t = t_1$; (b) $t = t_2$.

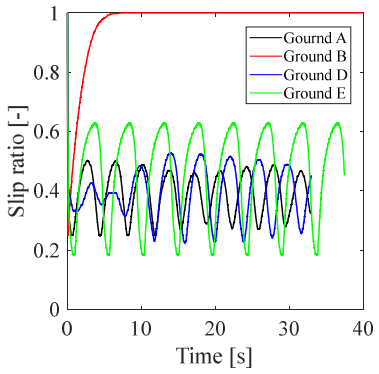

(a)

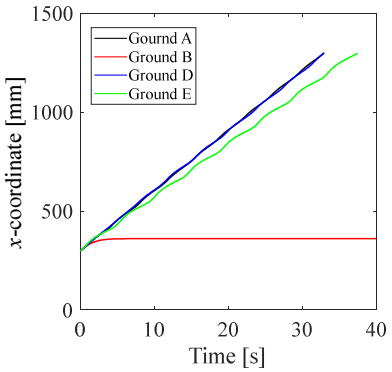

(b)

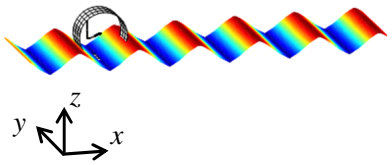

(c)

Figure 6.7: Terramechanics analysis results for field A, B, D, and E: (a) variation of the slip ratio with the elapsed time; (b) variation of the x-coordinate of the wheel center with the elapsed time; (c) trajectory of the wheel center for field B.

6.3.3 Effects of wheel specification and traveling direction

As described in Section 6.3.2, trafficability characterization of the wheel can be performed by reflecting the terrain geometry through terramechanics analysis of wind ripples formed under various conditions. The representative applications of terramechanics analysis are in wheel design and path planning. Therefore, this section presents a case study of trafficability characterization when the wheel specifications and motion conditions are changed for wind ripples formed under the specified conditions (condition C). Here, the wheel load, W and the towing load, P were fixed at 120 N and 15 N, respectively. First, the effect of the wheel radius, R was examined. In the analysis, the wheel radius was set to R = 50 mm, 100 mm, and 200 mm, and the trafficability data were evaluated. Here, ω = 1.0 rad/s, 0.5 rad/s. and 0.25 rad/s were set for each radius to obtain the same theoretical vehicle speed (corresponding to $s = 0.0$). Fig. 6.8 shows the trajectory of the wheel center. Figs. 6.9 (a) and 6.9 (b) show variations of the slip ratio and the traveling distance with the elapsed time. It can be observed from the figures that the larger the wheel radius, the higher the traveling performance. In general, the larger the wheel radius, the smaller the contact pressure and the lower the traveling resistance. Moreover, relative wheel radius with respect to the ripple height increases, producing low traveling resistance during climbing. As a result, the slip ratio required for traveling decreased and the wheel speed increased. On the other hand, when the wheel radius is small, the slip is required to exert the traction necessary for traveling, and the wheel speed is reduced. It should be noted that increasing the wheel radius increases the weight of the vehicle; thus, there is a trade-off relationship between energy consumption and payload during transportation.

Next, the effect of the wheel load, W is examined. In the analysis, the wheel load was set to W = 60 N, 120 N, and 240 N, and the trafficability data were evaluated. Figs. 6.10 (a) and 6.10 (b) show variations in the slip ratio and the traveling distance with the elapsed time. It can be observed from the figures that the lower the wheel load, W, the lower the traveling

performance; at $W = 60$ N, the wheel becomes stuck. This is because the maximum drawbar-pull that can be exerted at low wheel loads is reduced. Thus, the drawbar-pull required to overcome the slope cannot be exerted. On the other hand, a comparison of results obtained at $W = 120$ N and those of 240 N shows that there is minimal difference in the traveling speed, although there is a difference in the slip ratio under field condition C.

Finally, analysis results when the direction of travel is changed are presented. In the above analysis, although the wheel traveled perpendicular to the wind ripples (x direction), it traveled straight at an angle, θ_{tr} around the z axis. Fig. 6.11 shows the trajectory of the wheel center. Figs. 6.12 (a) and 6.12 (b) show variations of the slip ratio and the traveling distance with the elapsed time, respectively. Here, the transverse angle, $\theta_{tr}l$ was set to 0 deg, 5 deg, and 10 deg. As shown in the figures, the periods of fluctuation of the slip ratio are different because the time to reach the slope and the contact angle are different. In addition, the effect of the transverse angle gradually increases with the traveling distance. Further, the traveling speed is also affected due to variation in the slip ratio.

From the above, it can be concluded that terramechanics analysis using the wind ripple formation process under various conditions is effective for the robust design of vehicles [10, 11] and mobile robots [1] and optimal path planning [6,8,12]. The multi-stage analysis method, from terrain formation to vehicle locomotion, presented in this thesis can be employed for simulations in extreme environments such as planetary surfaces, deserts, and disaster sites, where sensing is difficult.

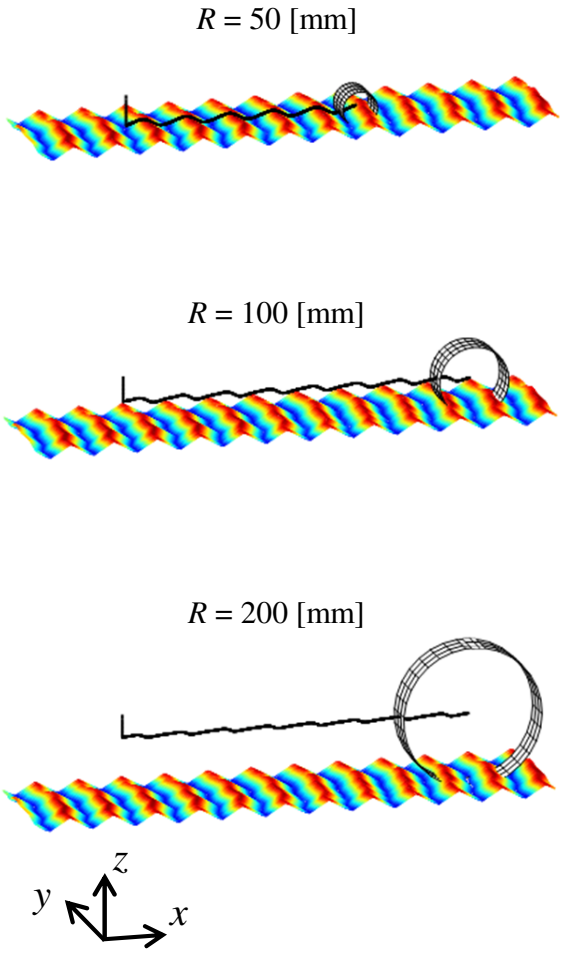

Figure 6.8: Trajectory of the wheel center for field C while varying the wheel radius.

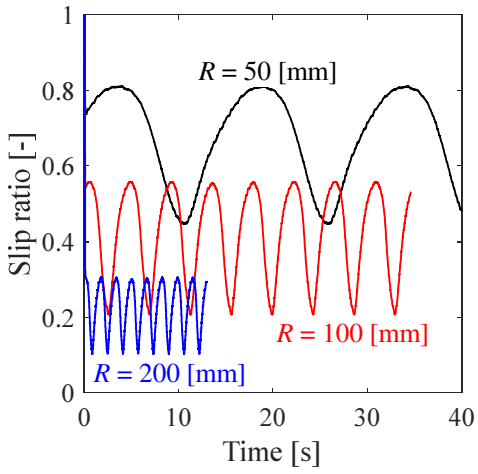

(a)

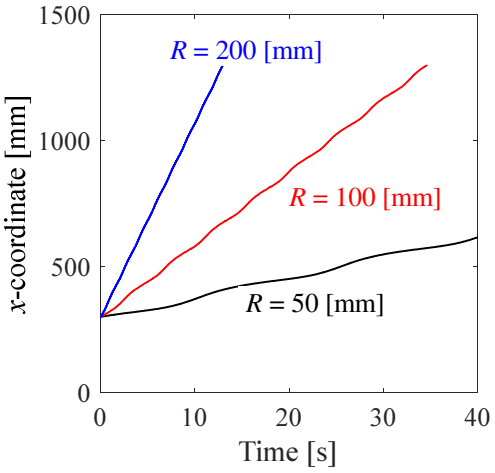

(b)

Figure 6.9: Terramechanics analysis results for field C while varying the wheel radius: (a) variation of the slip ratio with the elapsed time; (b) variation of the x-coordinate of the wheel center with the elapsed time.

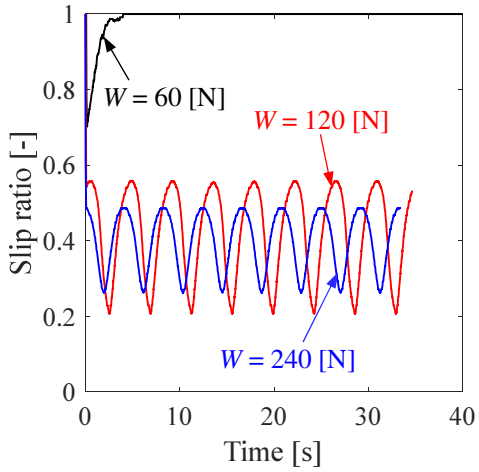

(a)

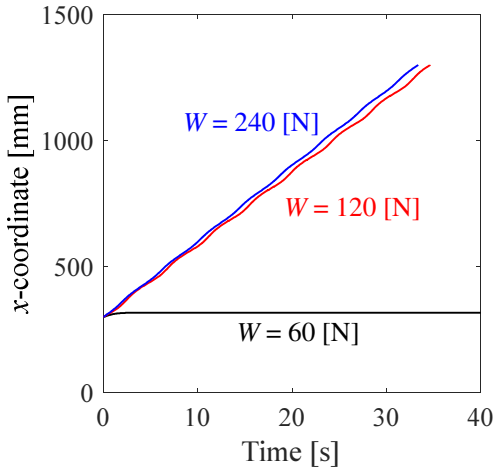

(b)

Figure 6.10: Terramechanics analysis results for field C while varying the wheel load: (a) variation of the slip ratio with the elapsed time; (b) variation of the x-coordinate of the wheel center with the elapsed time.

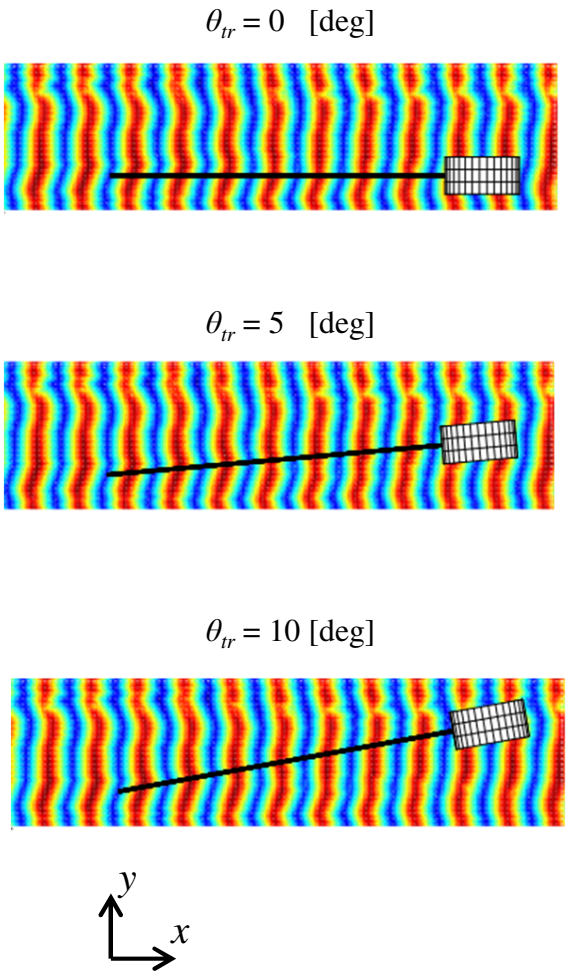

Figure 6.11: Trajectory of the wheel centre for field C while varying the transverse angle.

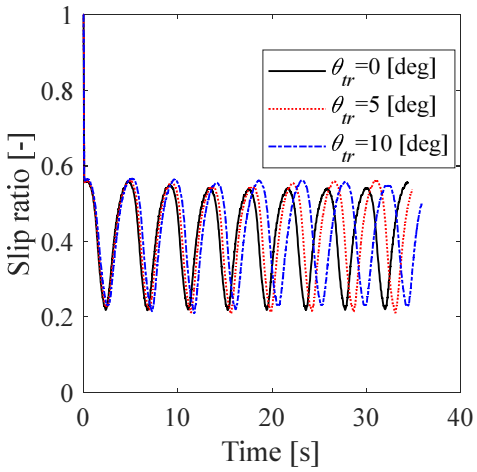

(a)

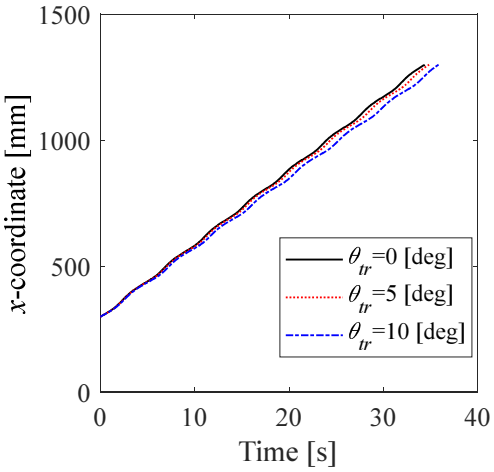

(b)

Figure 6.12: Terramechanics analysis results for field C while varying the transverse angle: (a) variation of the slip ratio with the elapsed time; (b) variation of the x-coordinate of the wheel center with the elapsed time.

6.3.4 Effect of scale factor distribution

Although the scale factor was fixed at 1.0 in this study, parameters are expected to vary on an actual terrain surface. In this section, the scale factor distribution is given for each cell, and the effect on the locomotion performance is confirmed. First, for each cell, random numbers were sampled from a normal distribution with the mean μ_ζ and standard deviation σ_ζ set to $(\mu_\zeta, \sigma_\zeta) = (0.500, 0.125), (1.000, 0.250), (1.500, 0.375)$. A histogram of the scale factors is presented in Fig. 6.13 (c), and the contour map showing their distribution is shown in Fig. 6.13 (d). The expected variation is confirmed. The locomotion characteristics of this terrain surface are shown in Fig. 6.13. Figs. 6.13 (a) and (b) plot the slip ratio and x-coordinate, respectively. The wheel travels three times under conditions with variations. Comparing under the same conditions, it seems that there is not much difference , although there is some variation in the locomotion data. Moreover, there is almost no difference between the results for $(\mu_\zeta, \sigma_\zeta) = (1.000, 0.250)$ and $(\mu_\zeta, \sigma_\zeta) = (1.000, 0.000)$. Under these conditions , the mean value and terrain-surface shape have more influence on the locomotion characteristics than the distribution characteristics of the scale factor.

A scale factor distribution can also be provided, depending on the surface height. In this study, we created a terrain-surface pattern Ⅰ in which the scale factor increases as the terrain surface rises, and a road-surface pattern Ⅱ in which the scale factor decreases. Wheel locomotion was analyzed on these surfaces (Fig. 6.14 (c)), giving the characteristics shown in Fig. 6.14. On the terrain surface of Pattern Ⅰ, the wheels tend to sink in the surface valleys, and the resistance from the front increases. Therefore, the wheels are slippery and the traveling time is effectively longer than on a uniform terrain surface . In contrast, in Pattern Ⅱ, the valley region is compacted and the resistance is reduced, which in turn shortens the traveling time.

As described above, the variation and distribution characteristics of terrain-surface parameters that can be obtained by measurement and numerical analysis can also be reflected in the analyses. This underlies the benefits of the

multi-stage analysis method proposed in this study.

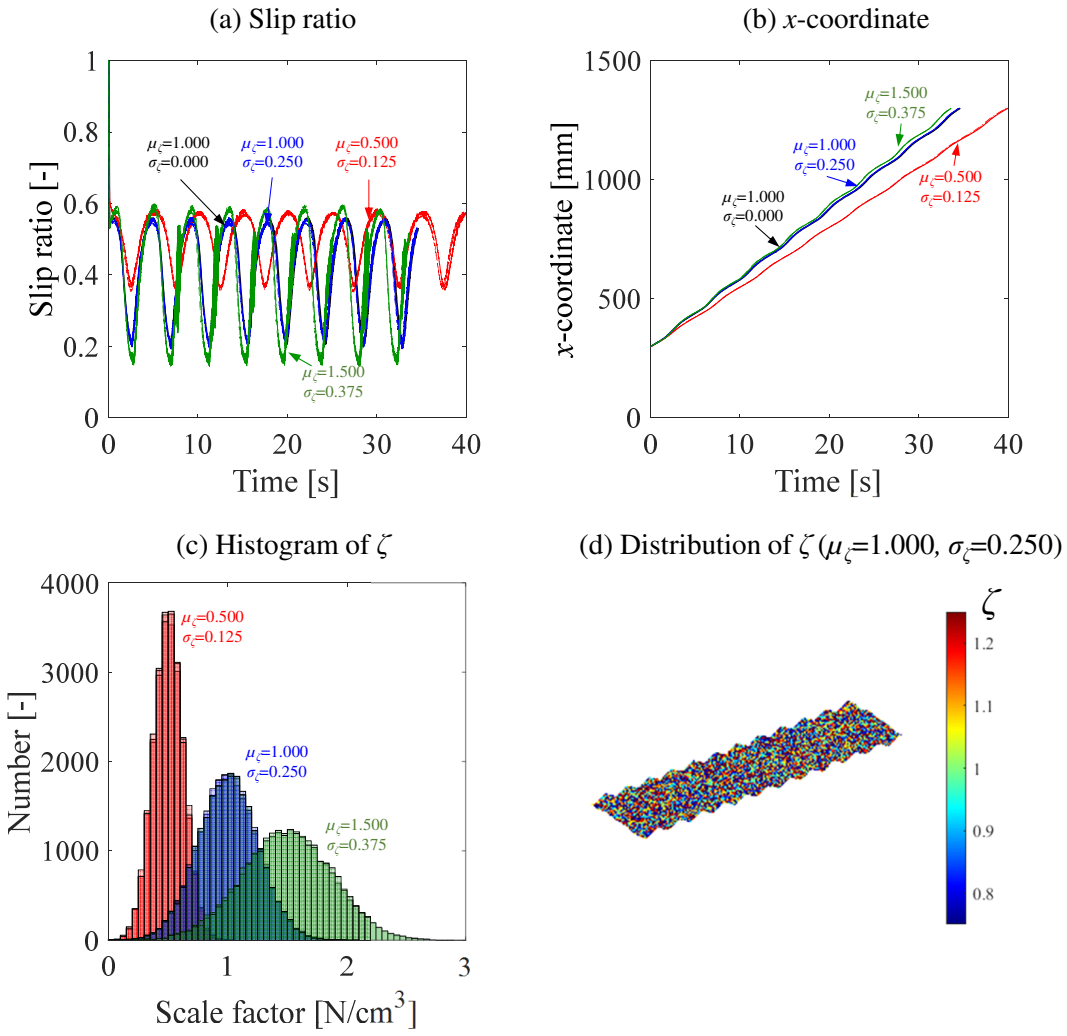

Figure 6.13: Terramechanics analysis results for Ground C, as the scale factor is varied: (a) variation in the slip ratio; (b) variation in the x-coordinate; (c) histogram of the scale factor; (d) scale factor distribution.

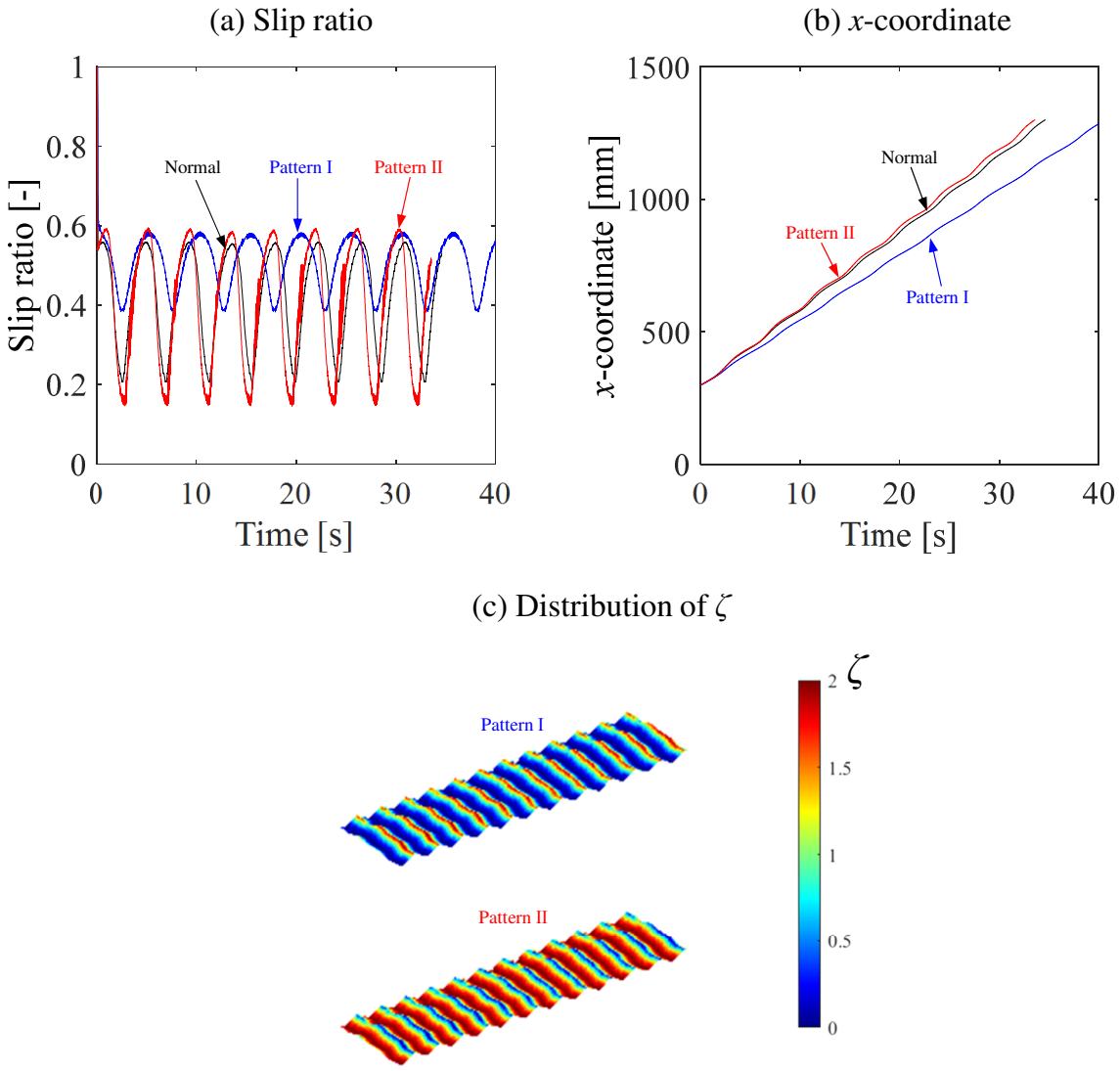

Figure 6.14: erramechanics analysis results for Ground C with a scale factor distribution that depends on the terrain surface height: (a) variation in the slip ratio; (b) variation in the x-coordinate; (c) scale factor distribution.

6.4 Conclusion

The conclusion of this study are summarized below.

- In this study, we proposed a multi-stage analysis method that seamlessly performs the process of ground surface formation and trafficability evaluation. In particular, we used wind ripple simulation for rough terrain modeling as an example and performed the simulation of single wheel locomotion on virtually created ground surfaces using RFT. Then, we performed terramechanics analysis of wheels on terrain fields created under various conditions. The proposed analysis method can be employed for advanced off-road vehicle traveling analysis in the future because various terrain fields can be considered.

- The proposed method of multi-stage terramechanics simulation can be used with other numerical analyses and measurement technologies. For example, information on ground surface deformation can be analyzed in detail for the finite element method or smoothed particle hydrodynamics, and the strain (density) information obtained from the analysis can be used for terrain field modeling and subsequent terramechanics analysis.

- It should be noted that the extension of terramechanics theory for rough terrain needs to be continued, because it is difficult to consider the movement and shearing of soil in conventional theories.

7 Extension of semi-empirical terramechanics approach

7.1 Introduction

A cellular automaton is a method of expressing the overall terrain surface deformation by dividing a field into cells and defining the extent of movement in each cell. The rolling [17, 84], which is a variation mechanism of the cell height can express the action of the soil existing at a high position flowing to a lower position, thereby promoting the stabilization of the terrain surface shape. This method is effective in expressing the interaction between terrain surfaces, but it is difficult to consider the interaction between the object and the terrain surface using only the conventional model. Therefore, in this study, a movement mechanism based on the contact state between the object and terrain surface was introduced in the proposed model. Based on the stress distribution obtained by an interaction model, such as conventional terramechanics models, the amount and direction of movement of the terrain surface were defined. Furthermore, changes in the soil density owing to deformation were considered. In classical terramechanics theory, the normal stress that occurs on the surface of objects depends on soil density [3, 35], which changes with ground deformation. In this study, the change in density is evaluated from the strain on the ground, and this is linked to the change in the analysis parameters.

First, a plate drag analysis based on the proposed model was performed. The horizontal resistive force generated when a vertical plate was displaced horizontally was evaluated. Moreover, experiments were conducted under the same conditions, and the analysis parameters were validated by comparing the results. Second, a single-wheel traveling analysis was performed using the obtained parameters. The proposed model was validated by comparing the experimental results such as those of sinkage and drawbar-pull with the model-based results. Notably, the traveling experiments and analyses were

performed not only on flat terrain surface, but also on sinusoidal-shaped surfaces, in which the terrain surface deformation considerably affects the traveling characteristics.

7.2 Terrain surface deformation and change in terramechanics parameter

This section describes the extended model that can express the deformation and property variations of the terrain surface caused by the interaction between the object and terrain surface. The model derivation is based on the flow shown in Fig. 7.1, and the details are presented in the subsequent subsections.

7.2.1 Terrain surface deformation

The terrain surface deformation is expressed based on a cellular automaton. In this study, in addition to the rolling action used by Nishimori and Ouchi [17], the moving action (bulldozing and removal of soil) is incorporated.

Fig. 7.2 shows the schematic of the moving action, which can be expressed as follows:

$$\begin{aligned} dh^{\mathrm{mov}}_{i,j} &= -S_{i,j} \\ dh^{\mathrm{mov}}_{i+di,j+dj} &= R_1 S_{i,j} \end{aligned} \tag{7.1}$$

Here, $dh^{\mathrm{movl}}_{i,j}$ represents the amount of change in the terrain surface height in a certain cell by the moving reaction. Subscripts i and j indicate the cell numbers corresponding to the x and y directions, respectively. According to Eq. (7.1), the soil height in a certain cell, $S_{i,j}$, moves to an adjacent cell in a certain direction. Because the soil is expected to be compressed or expanded, it moves with a height multiplied by the ratio R_1 to the destination. Subscripts di and dj are determined considering the stress distribution for each cell, as evaluated using conventional terramechanics models (such as BWR and RFT). As shown in Fig. 7.2, if the x-stress generated on the wheel is

in the negative direction, di is 1, because the soil is pushed in the positive direction of the x-axis. In contrast, in the region behind the wheel, di is -1, because the wheel shifts the soil rearward.

The amount of movement $S_{i,j}$ is determined considering the penetration of the object into the terrain surface, $\delta_{i,j}$. To stabilize the terrain surface deformation, $S_{i,j}$ is controlled by the penetration amount $\delta_{i,j}$ multiplied by the ratio, i.e.,

$$S_{i,j} = R_2 \delta_{i,j} \tag{7.2}$$

In this manner, the proposed model can represent the terrain surface deformation caused by the interaction between the object and soil.

Fig. 7.3 shows the schematic of the rolling action, which reflects the deformation that occurs when a steep slope is difficult to maintain. This action can be expressed as follows:

$$dh_{i,j}^{\text{roll}} = -rh_{i,j} + \frac{r}{6} H_{\text{cross}} + \frac{r}{12} H_{\text{diag}} \tag{7.3}$$

Here, $dh_{i,j}^{\text{roll}}$ is the amount of change in the terrain surface height in a certain cell. According to the abovementioned equation, the soil present in a certain cell rolls to the adjacent cell because of gravity and receives an inflow from the outside, as shown in Fig. 7.3. The outflow rate is multiplied by the ratio r to the height $h_{i,j}$ of the cell. Moreover, $rh/6$ flows in from the vertical and horizontal directions, and $rh/12$ flows from the diagonal direction. The vertical and horizontal inflow terms and diagonal terms can be defined as H_{cross} and H_{diag}, respectively:

$$\begin{aligned} H_{\text{cross}} &= h_{i+1,j} + h_{i-1,j} + h_{i,j+1} + h_{i,j-1}, \\ H_{\text{diag}} &= h_{i+1,j+1} + h_{i+1,j-1} + h_{i-1,j-1} + h_{i-1,j+1}. \end{aligned} \tag{7.4}$$

The rolling action is assumed to occur only when the gradient of the adjacent cells exceeds the angle of repose ϕ_r.

The amount of change in the height evaluated from the two actions is simultaneously applied to all cells, and the terrain surface shape for the next

step, $h'_{i,j}$, is determined as follows:

$$h'_{i,j} = h_{i,j} + dh^{\mathrm{roll}}_{i,j} + dh^{\mathrm{mov}}_{i,j} \tag{7.5}$$

The calculation of the terrain surface deformation is repeated within one time step of the terramechanics analysis to ensure that the terrain surface is stably deformed.

7.2.2 Changes in parameters owing to the terrain surface deformation

In practice, the property of the terrain surface might change with deformation. In this study, the change in density is estimated based on the strain of the ground and incorporated in the terramechanics model. The volumetric strain on the terrain surface can be defined as follows:

$$(1 + \varepsilon_v)\, V_0 = V \tag{7.6}$$

where V_0 is the initial volume corresponding to one cell, and V is the volume after deformation. Because the mass m must be conserved in the ground, it can be expressed as follows in terms of the initial density ρ_0 and density ρ after deformation.

$$m = \rho_0 V_0 = \rho V \tag{7.7}$$

Substituting Eq. (7.6) into Eq. (7.7) yields the following relation.

$$\rho = \frac{\rho_0}{1 + \varepsilon_v} \tag{7.8}$$

By substituting Eq. (7.8) into Eq. (2.1) of the BWR model, the property change owing to the terrain surface deformation can be reflected.

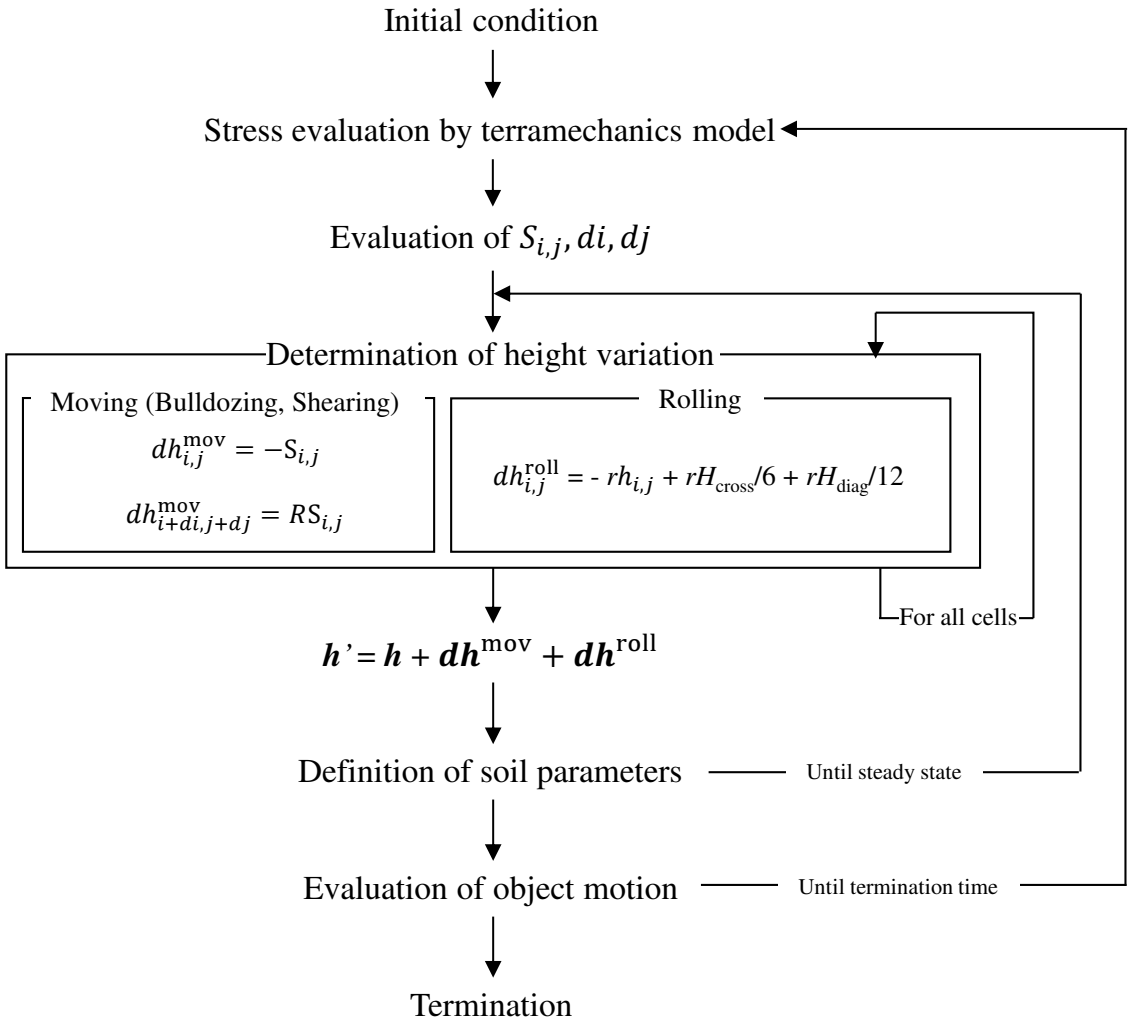

Figure 7.1: Terramechanics analysis flow considering the terrain surface deformation.

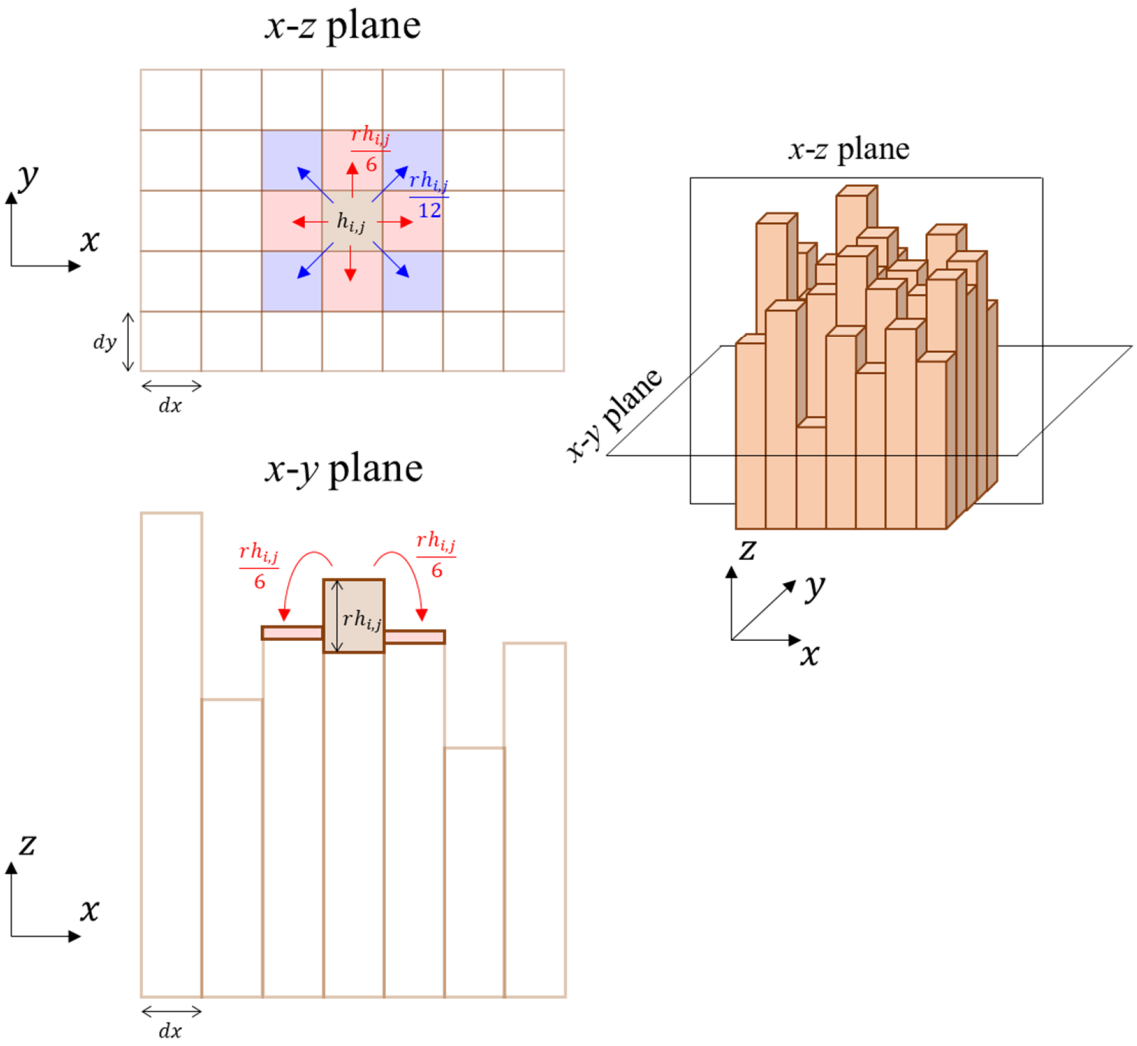

Figure 7.2: Schematic of moving action.

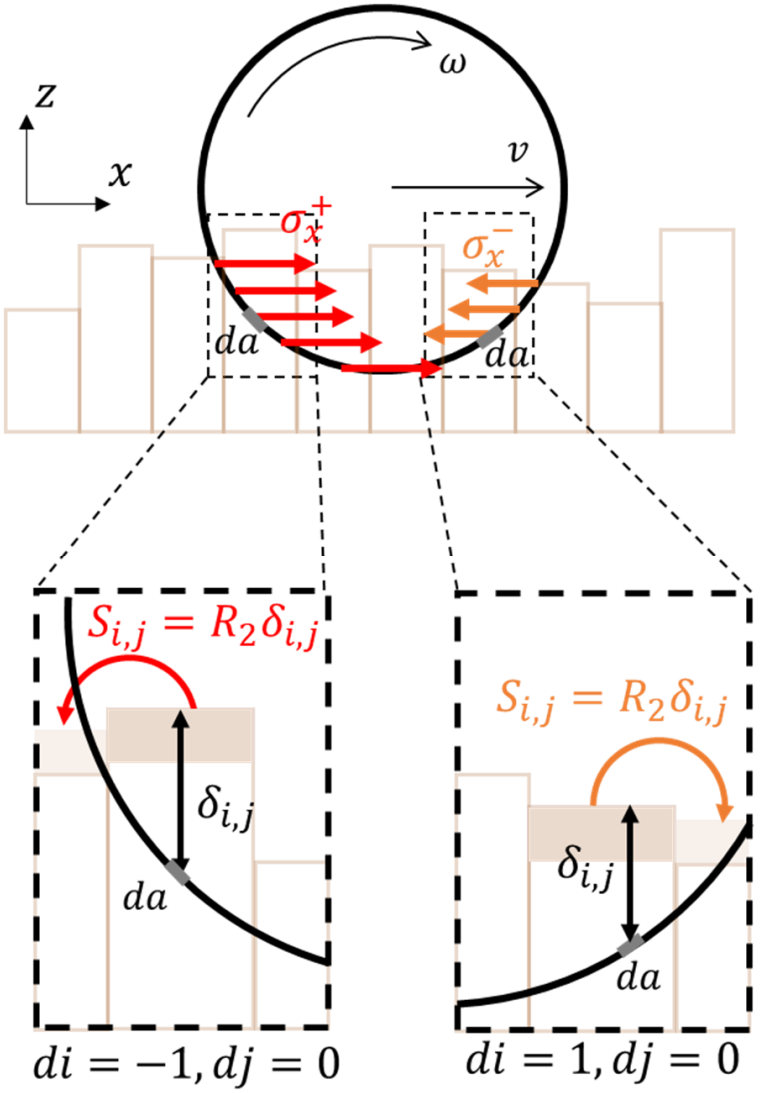

Figure 7.3: Schematic of rolling action.

7.3 Experimental apparatus

This section describes the experimental apparatus used in the verification tests. Fig. 7.4 shows an overview of the experimental rig. A soil vessel made

of acrylic resin, with a length, width, and height of 1500 mm, 400 mm, and 400 mm, respectively, was filled with the prescribed amount of sand, here, Toyoura sand, the bulk density of which was maintained at approximately 1,488 kg/m^3 in the plate and traveling tests . A single-wheel ran over the sand. The test bed involved a conveyance unit and wheel-driving unit, each of which was driven by an independent motor. The translational velocity and angular velocity of the wheel were calculated based on the data obtained using encoders mounted on the conveyance motor and wheel-driving motor. Thus, by controlling the translation and angular velocities of the wheel, an arbitrary slip ratio could be set. In the traveling experiments, forced-slip experiments were conducted, and the slip ratio was controlled by fixing the angular velocity, ω as 0.2 rad/s and varying the translational velocity v. In addition, the plate drag test could be implemented by replacing the wheel part of the apparatus with the plate, as shown in Fig. 7.8.

The forces and torques generated by the wheel locomotion were measured using a six-axis force/torque sensor. Furthermore, the wheel sinkage and traveling distance were measured using magnetic scales. The specifications of the sensors are listed in Table 7.1.

The sinusoidal terrain surface was created using a rake, as shown in Fig. 7.5. By sliding this in the transverse direction against the wheel locomotion, a terrain surface according to the rake shape could be generated.

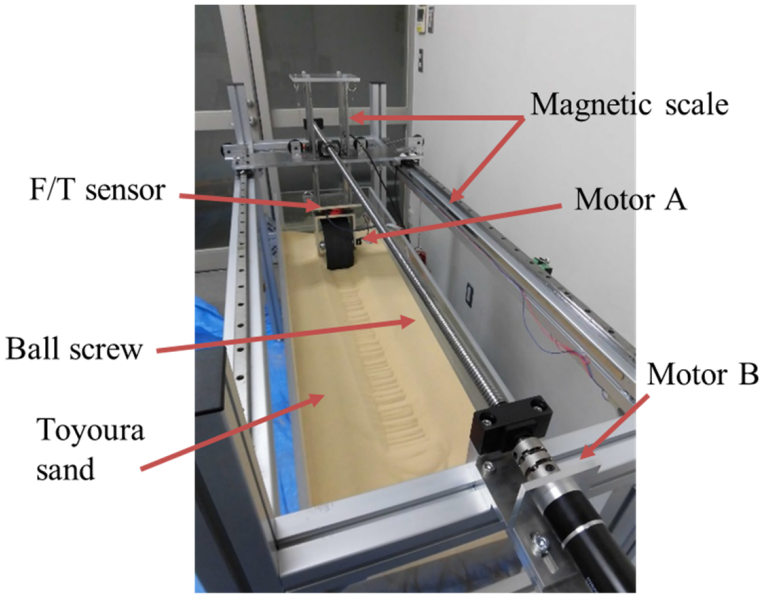

Figure 7.4: Experimental setup of single-wheel traveling apparatus. The translation and angular velocities were controlled under a constant wheel load.

Table 7.1: Specifications of sensors.

Motor A	Maxon motor RE-25 10 W
Motor B	Maxon motor RE-40 150 W
Magnetic scale	HIWIN PS-A
F/T sensor	Wacoh-tech DynPick [WEF-6A200-4]

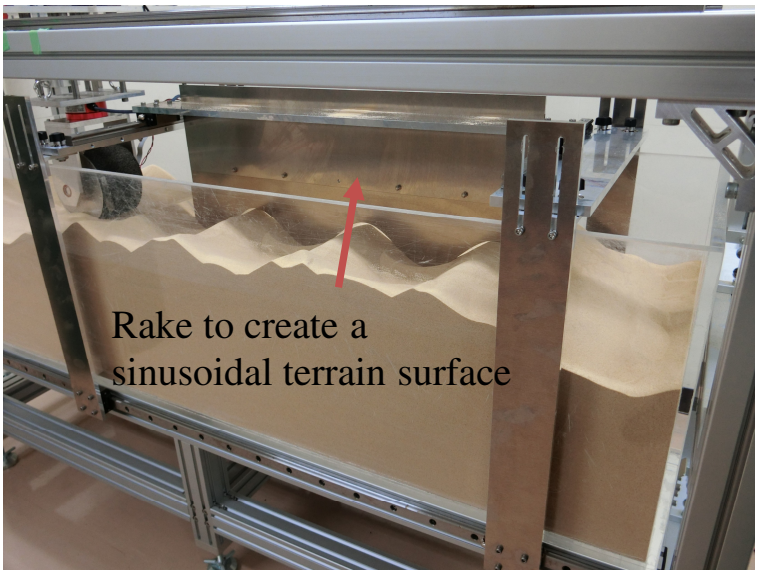

Figure 7.5: Rake to create a terrain surface with a sinusoidal shape.

7.4 Plate drag analysis

A plate drag test was conducted, in which a vertical plate with a width of 137 mm was displaced horizontally at a constant velocity $v_p = 10$ mm/s and depth (initial sinkage) of 10 mm. The horizontal force applied to the plate was measured. The test was performed three times to confirm the reproducibility. Next, the numerical analysis was performed under the same conditions as in the experiment, and the terrain surface deformation owing to the the translation of the plate was evaluated using the proposed model coupled with the RFT. The scale factor ζ required for the RFT was set as $\zeta = 0.180$ [N/cm^3].

The testbed in the analysis had dimensions of 1.5×0.40× 0.25 m and was discretized into cells with lengths of $di \times dj$=5.0 mm×5.0 mm. In general, a finer discretization corresponds to a higher accuracy and less noise, albeit at a higher calculation cost. The cell size was determined considering this trade-off. The analysis parameters for the moving and rolling reactions are listed

in Table 7.2. These values were determined by observing the terrain surface deformation and comparing the resistive forces obtained in the experiments and numerical analysis.

Fig. 7.6 shows the experimentally and analytically obtained change in the resistive force over time. The resistive force gradually increases and eventually attains a steady state in experiments. This phenomenon likely occurs because the carried sand accumulates in front of the plate, and its volume is reflected in the resistive force. According to the results obtained based on the proposed model, the resistive force increases with the displacement of the plate, which is in agreement with the experimental results. Fig. 7.7 shows the state of the terrain surface deformation. A carried lump is formed in front of the plate, and the lump flows sideways through the rolling action of sand, such that embankments are formed on the side of the plate. This phenomenon can also be observed in the experimental results, as shown in Fig. 7.8. Thus, the proposed model can quantitatively express the terrain surface deformation of sand.

Fig. 7.7 shows the stress distribution on the plate, evaluated using the RFT. According to the side viewpoint, the horizontal stress (indicated by red lines) increases as the depth increases. The overhead viewpoint illustrates the stress distribution in the width direction. Specifically, because of the rolling action, the height of the terrain surface decreases, and the stress decreases toward the side. This phenomenon is a notable result obtained by introducing the terrain surface deformation model.

It should be noted that in the conventional terramechanics analysis that does not consider the terrain surface deformation, the resistive force evaluated using the RFT does not change because the orientation angle β, velocity vector angle γ, and sinkage z are constant (see the dotted line in Fig. 7.6).

Table 7.2: Analysis parameters for the cellular automata

ϕ_r	[deg.]	34.0
r	[-]	0.20
R_1	[-]	0.99
R_2	[-]	0.20

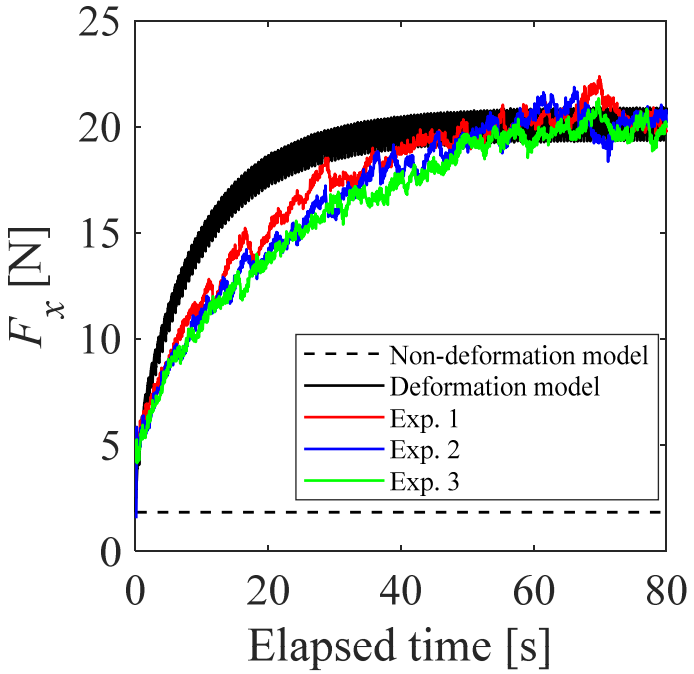

Figure 7.6: Variations in the resistive force with the elapsed time.

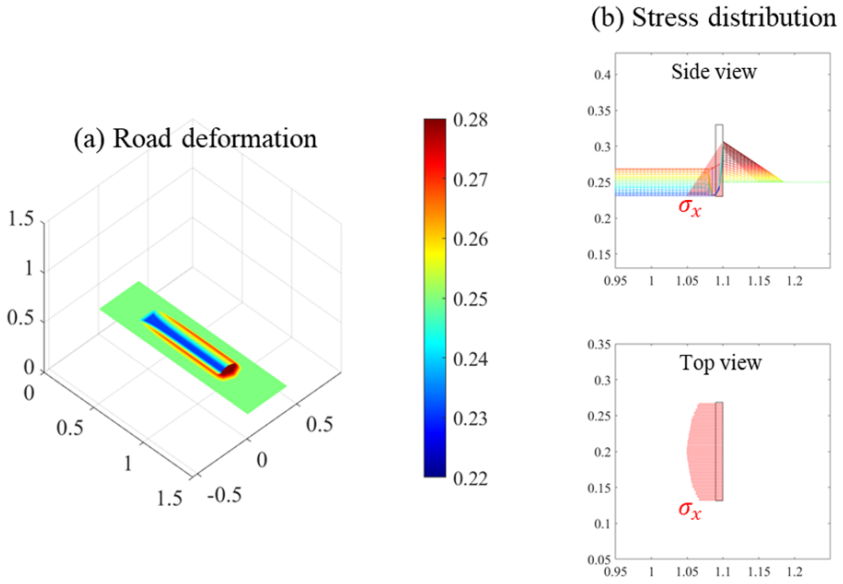

Figure 7.7: Terrain surface shape and stress distribution generated on the plate, obtained in the simulation based on the proposed model: (a) Terrain surface shape after passage through the plate; (b) Stress distribution.

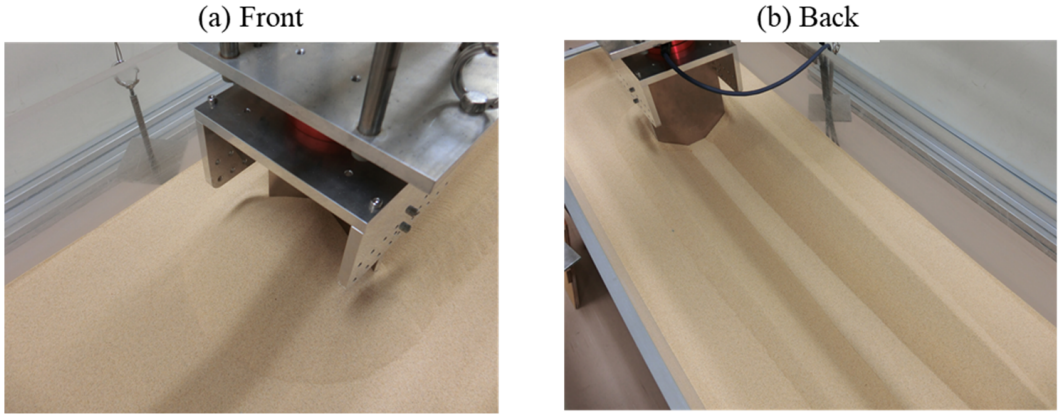

Figure 7.8: Terrain surface shape after the plate drag test.

7.5 Wheel traveling analysis

Single-wheel traveling analyses were performed using the same terrain surface deformation parameters as those in the plate drag test. The angular velocity ω was set as 0.2 rad/s and the translational velocity v was varied to realize the forced-slip condition. The slip ratio was set as s=0.0, 0.1, 0.3, 0.5, and 0.7, and the traveling characteristics under each condition were evaluated. Furthermore, a traveling analysis was performed on not only a flat terrain surface but also a terrain surface with a sinusoidal shape. This analysis condition was considered to verify the proposed model for the case in which the terrain surface deformation in front of the wheels considerably influences the traveling.

The specifications for the rigid wheel are listed in Table 7.3. The parameters used in the terramechanics model (BWR model) are listed in Table 7.4. The parameters for the moving and rolling actions were the same as those in the plate test. The wheel loads for the traveling tests on a flat terrain surface and sinusoidal surface were different. The analysis results were compared with the experimental results and discussed.

Table 7.3: Specifications of the rigid wheel.

Wheel diameter	[mm]	200
Wheel width	[mm]	100
Vertical load	[N]	154 (Flat), 66.7 (Sinusoidal)

Table 7.4: Analysis parameters of BWR model used for stress evaluation.

c	[Pa]	0.0
ϕ_i	[deg.]	34.0
ρ_0	[kg/m^3]	1488
g	[m/s^2]	9.81
n	[-]	1.0
k_c	[-]	0.0
k_ϕ	[-]	34.3
a_0	[-]	0.20
a_1	[-]	0.30
k_x	[m]	0.035

7.5.1 Flat terrain surface

First, we examine the single-wheel traveling phenomena on a flat terrain surface. Fig. 7.9 shows the variation in the drawbar-pull and sinkage as a function of the traveling distance at each slip ratio, as obtained experimentally. Fig. 7.10 shows the corresponding values obtained using the proposed model. According to both the experiment and analysis results, the drawbar-pull and sinkage decrease and increase gradually, respectively, and converge to a steady value. This phenomenon occurs because the initial sinkage of the wheel increases the traveling resistance in the initial stage. Furthermore, in the steady rolling conditions, the drawbar-pull and sinkage increase with the slip ratio in the range of the examined conditions.

Fig. 7.11 shows the traveling characteristics in the steady state plotted against the slip ratio. The figure shows the results for the three experiments as well as those obtained using the conventional model that does not incorporate the terrain surface deformation. The parameters for the BWR model were the same as those for the proposed model.

According to the conventional model, the change in the sinkage with respect to the slip ratio is small because the conventional model does not

consider the removal of sand owing to the wheel shearing and forward extrusion (bulldozing). In contrast, the results obtained using the proposed model coupled with the BWR model are based on the moving and rolling actions, and a reasonable change in the sinkage can be confirmed. The trend of the sinkage against the slip ratio is similar to that obtained experimentally. In addition, the results of the drawbar-pull obtained using the proposed model are in agreement with the experimental results.

Fig. 7.12(a) and 7.12(b) show the residual deformation of the terrain surface after wheel traveling under the slip ratios of 0.3 and 0.7, respectively. The longitudinal length of the terrain is 1.5 m. The colors in the contour map represent the deformation of the terrain surface in the vertical direction (unit: m). In addition, the figure shows the results of the stress distribution on the wheel surface during the steady state. At the relatively low slip ratio of 0.3, the area in which the horizontal stress acts positively (red area in the figure) is not significant. Thus, the drawbar-pull is low. In contrast, at a high slip ratio of 0.7, the area in which the horizontal stress acts in the positive direction is large, and the sand moves rearward of the wheel. This phenomenon indicates that the lump of sand in front of the wheel is smaller, and the rut surface behind the wheel is higher than that under the low-slip condition.

Moreover, in the case of the high slip ratio, the shearing action because of the rotation and translation of the wheel per unit distance traveled longitudinally is large. Therefore, the sinkage increases owing to the rearward movement of the soil. Overall, this type of terrain surface deformation and the accompanying changes in the contact state, which affect the traveling characteristics, can be reasonably evaluated using the proposed model.

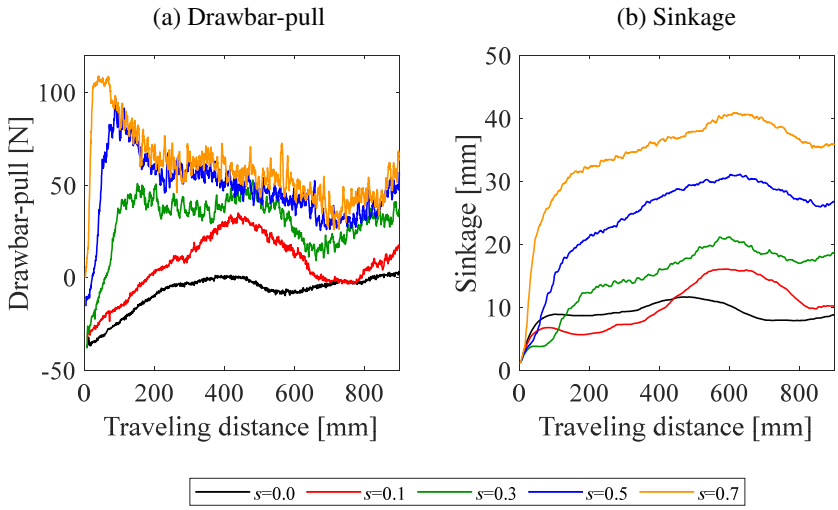

Figure 7.9: Variations in the (a) drawbar-pull and (b) sinkage with the traveling distance, as obtained experimentally. The results correspond to seven levels of the slip ratio s.

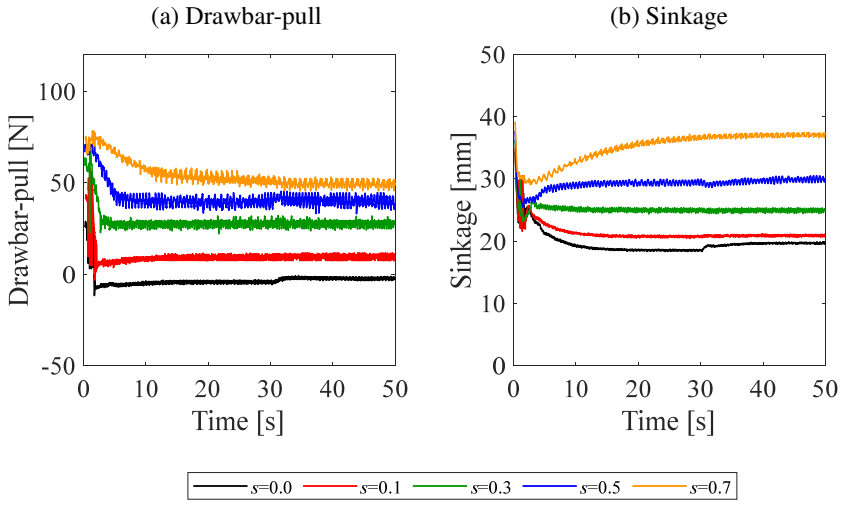

Figure 7.10: Variations in the (a) drawbar-pull and (b) sinkage with the elapsed time, as obtained using the proposed model.

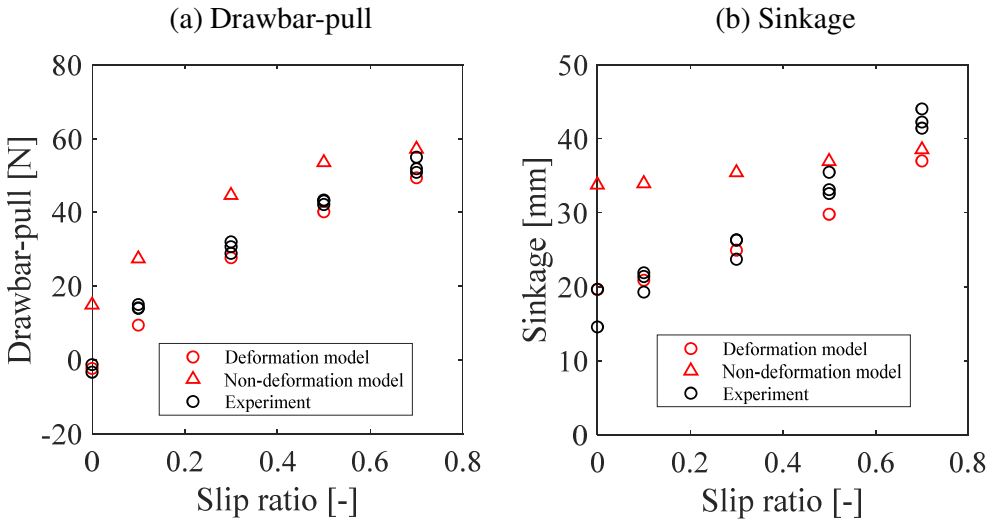

Figure 7.11: Relationship between the steady-state traveling characteristics and slip ratio: (a) drawbar-pull; (b) sinkage.

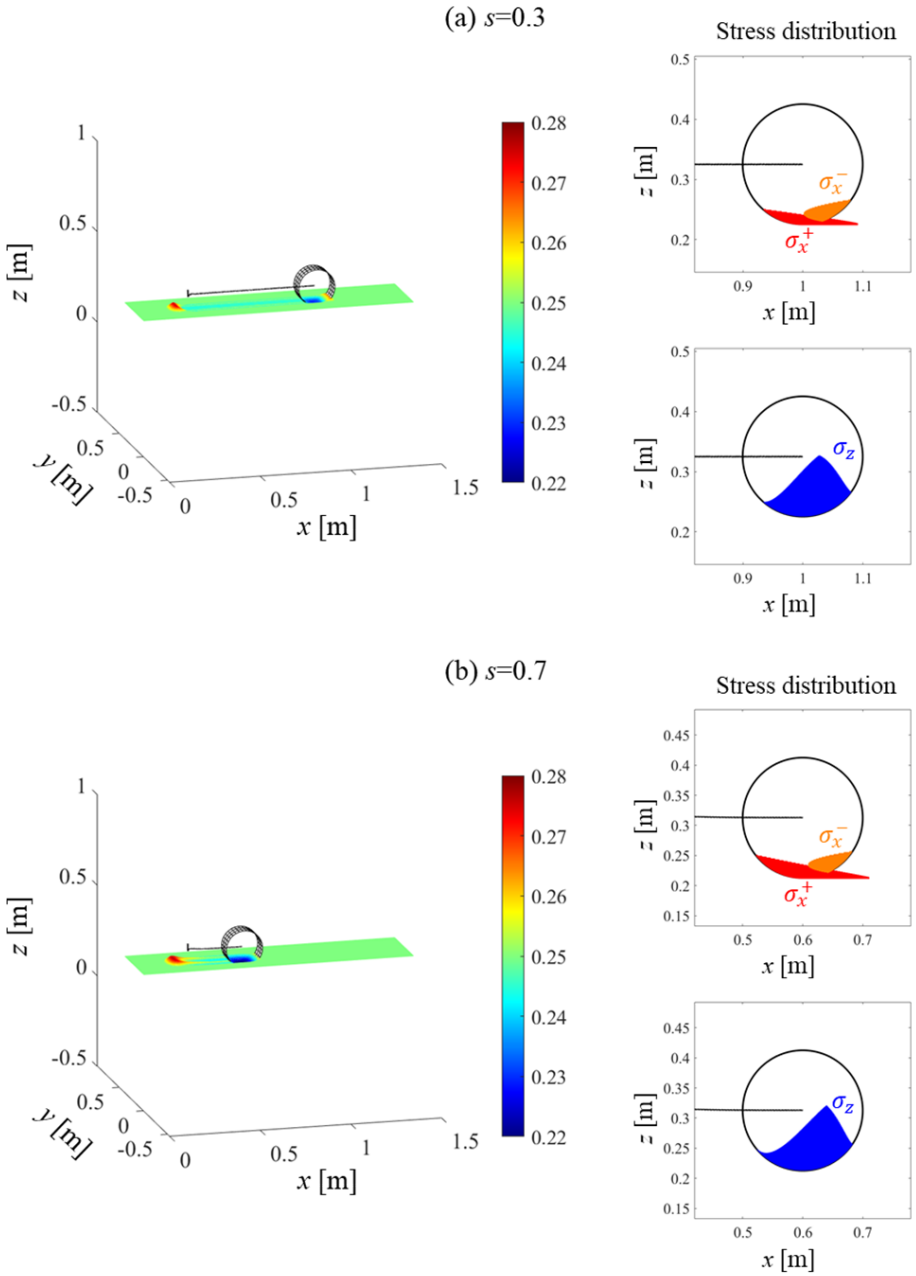

Figure 7.12: Residual deformation of the terrain surface and stress distribution on the wheel surface in the steady state: (a)s=0.3; (b)s=0.7. The black line in the figure shows the trajectory of the wheel center.

7.5.2 Sinusoidal terrain surface

This section describes the analysis of the traveling characteristics of the wheels on the sinusoidal terrain surface. The traveling characteristics were obtained at a slip ratio of 0.3. The target terrain surface was a sinusoidal surface with an amplitude of 3.0 cm and wavelength of 22.5 cm (Fig. 7.5). In the proposed model, the interaction with the slope, such as those in the form of the contact angles θ_f and θ_r, automatically changed depending on the contact state, as shown in Fig. 7.13; therefore, the model and the parameters used for traveling on a flat terrain surface could be adopted.

Fig. 7.14 shows the changes in the drawbar-pull and vertical translation of the wheel center over time. The calculated values fluctuate according to the shape of the terrain surface under all the conditions. However, in the analysis based on the conventional model, the period of the sinkage variation is different from that observed in the experiment, and the amplitude increases. In the actual phenomenon, when the wheel pushes the sand forward, and the sinusoidal-shaped surface deforms, the amplitude of the vertical translation of the wheel decreases, and its peak position shifts. The conventional model does not consider such terrain surface deformations.

In contrast, according to the proposed model, the traveling resistance is generated in the front of the wheel owing to the bulldozing effect. This phenomenon can be confirmed from the stress distribution shown in Fig. 7.15. The terrain surface deformation, which similar to the actual phenomenon, as shown in Fig. **??**, can be qualitatively expressed. In particular, the sinkage behavior approaches the amplitude of the experimental results, as observed from the terrain surface deformation and stress distribution shown in Fig. 7.15.

Fig. 7.15 shows the stress distribution at time $t = t_1$ and $t = t_2$, when the drawbar-pull is the minimum and maximum, respectively. At $t = t_1$, a sand lump exists in front of the wheel, and the area in which a negative σ_x is generated on the wheel surface is large. This stress distribution deforms the terrain surface, and the abovementioned phenomenon is reproduced. At $t =$

t_2, the wheel goes down the slope. In this situation, the shearing area is large, and the sand is moved rearward. The results of the drawbar-pull obtained using the proposed model are in agreement with the experiment. This finding could be attributed to the fact that the contact state, similar to the actual phenomenon, was evaluated using the terrain surface deformation, and the traveling resistance was suitably reflected, which could not be accomplished using the conventional model. These results demonstrate that the proposed model is effective to realize terramechanics analyses under non-flat terrain surface conditions.

(a) Descending

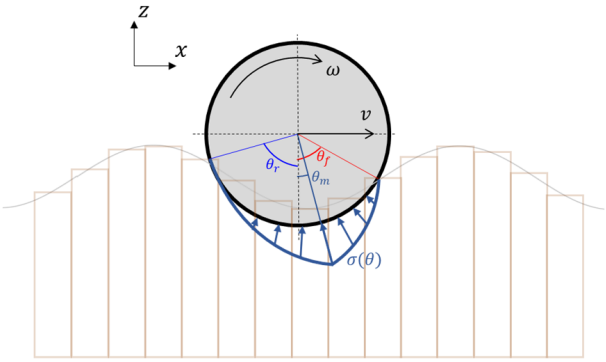

(b) Climbing

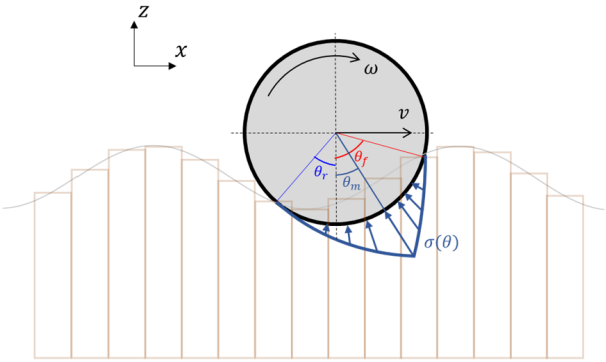

Figure 7.13: Determination of θ_f and θ_r in the proposed model for uneven terrain surface: (a) Descending; (b) Ascending.

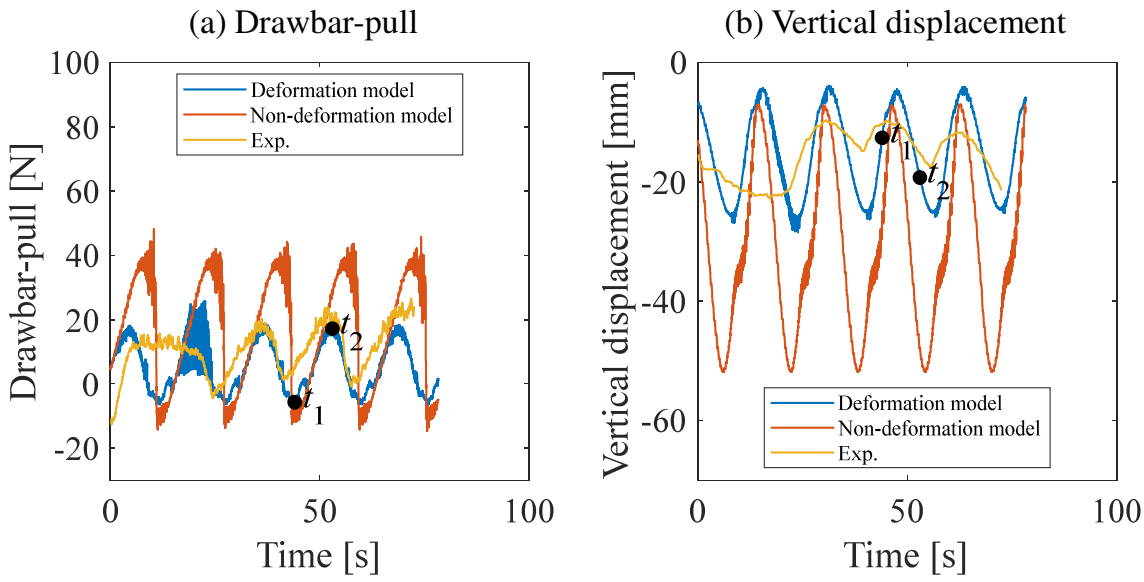

Figure 7.14: Variations in a)drawbar-pull and (b) vertical displacement with the elapsed time on the sinusoidal surface.

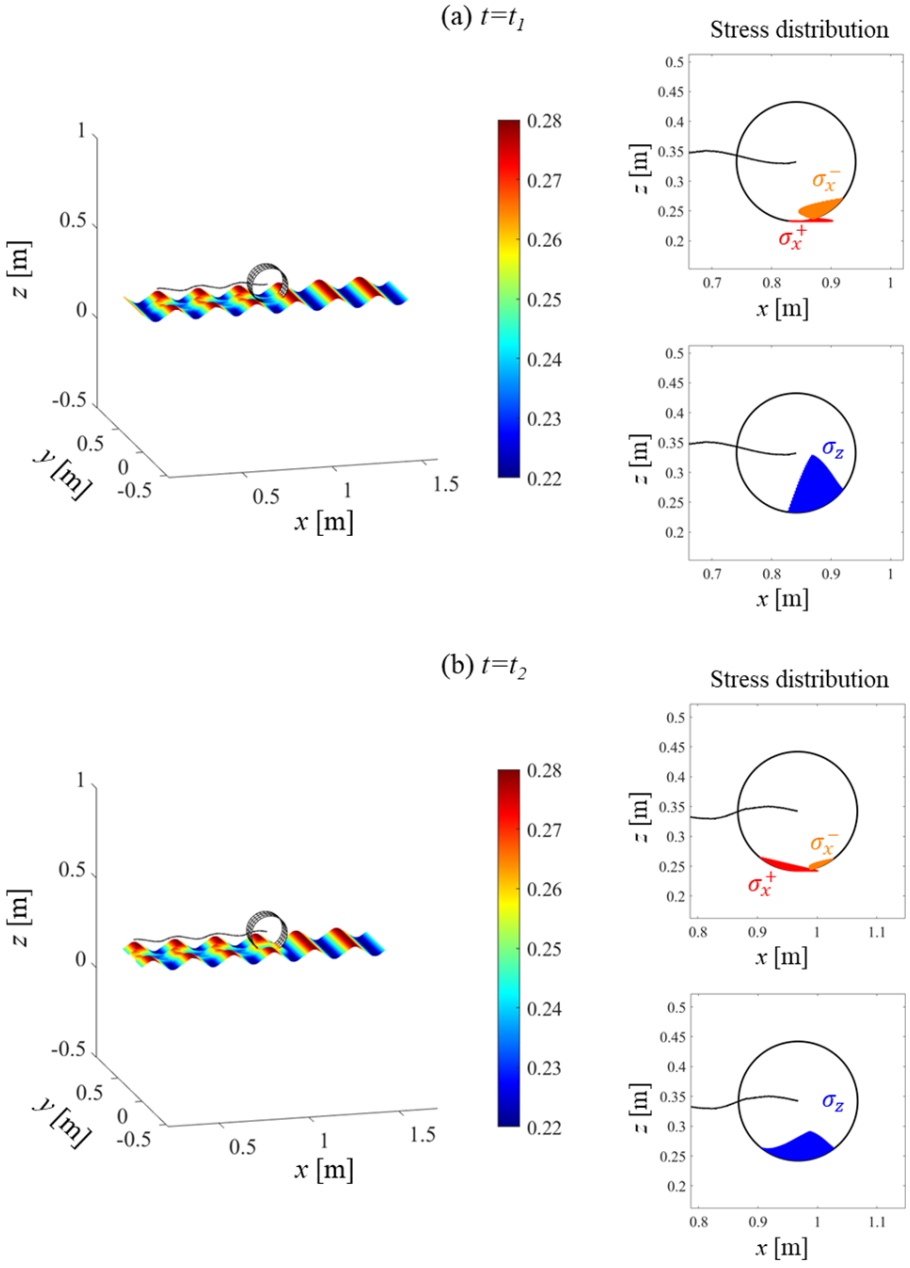

Figure 7.15: Terrain surface deformation after traveling on sinusoidal surface and stress distribution on the wheel surface: (a)$t = t_1$; (b)$t = t_2$. The black line indicates the trajectory of the wheel center.

7.6 Conclusion

We developed an extended terramechanics model, which incorporated the terrain surface deformation mechanism based on cellular automata.

First, a plate drag test was conducted, and the results were compared with those of the proposed model. The analysis results obtained using the proposed model were in agreement with those obtained experimentally. In particular, the same terrain surface deformation as that confirmed in the actual phenomenon was represented. Next, a single-wheel traveling analysis was conducted considering the terrain surface deformation parameters obtained in the plate drag test. The experimentally obtained drawbar-pull and sinkage could be reasonably simulated, which is difficult to realize conventional methods. The proposed model could help realize high-precision simulations taking into account the terrain surface deformation. In addition, the proposed model could be applied to not only a flat terrain surface, but also a rough terrain surface such as that with a sinusoidal shape. The proposed model is expected to effective in solving various terramechanics problems because arbitrary interaction models can be used for the stress evaluation for the moving action. Moreover, the proposed method can likely be applied to not only wheel traveling problems but also excavation problems.

In addition, because the numerical simulation associated with the proposed model has a relatively low computational cost, it can likely be implemented in multibody dynamics analysis. Future work will be aimed at implementing the proposed model in multibody dynamics analysis and realizing a full-vehicle simulation considering the terrain surface deformation.

8 Summary and future work

8.1 Summary

In this study, several traveling analyses have been conducted with the aim of proposing a new terramechanics analysis method that compensates for the limitations of the conventional method.

In Chapter 3, the traveling analysis of a dump truck for mining has been performed as an example of multibody dynamics analysis using a terramechanics model. A BWR model has been introduced for the interaction between tire and ground, and the traveling characteristics of the vehicle on rough terrain have been verified. Furthermore, a control method called the traction control system (TCS) installed in the actual machine has been introduced in this simulation. In this chapter, the influence of this control on the traveling performance and control method has been examined. This simulation made it possible to evaluate the traveling characteristics of vehicles under various terrain surface conditions and to examine the effects of control methods on traveling characteristics.

In Chapter 4, the traveling analysis of wheels with grousers has been performed using the RFT. The applicability of the RFT has been examined by simulating wheels with grousers using DEM and RFT and comparing both results. It was confirmed that the use of the RFT is effective in terramechanics analysis, although it has the drawback that sand shear and movement are not considered.

In Chapter 5, a grouser shape for wheels has been proposed based on a simulation using the RFT. In this chapter, an RFT-based terramechanics simulation has been performed while complementarily utilizing DEM analysis and model experiments. Accordingly, a wheel with a trapezoidal grouser has been proposed. The proposed shape has a packing effect in which the particles between the grousers are strongly compressed. It was confirmed that, by applying this shape to the wheels, the decrease in drawbar-pull due to the grouser shape was suppressed more than expected, and the sinking

of the wheels was significantly suppressed. Although it will be necessary to optimize the detailed specifications of the proposed shape in the future, it was suggested that the trapezoidal grouser is an effective shape for a wheel for a lunar/planetary exploration rover.

In Chapter 6, a multi-stage analysis method has been proposed that uses the terrain surface information obtained from other simulation and measurement techniques in a field model for terramechanics simulation. As an example of the terrain surface formation simulation, a wind pattern generation simulation based on a cellular automaton has been performed, and a single-wheel traveling simulation that utilizes the terrain surface information obtained thus has been performed. The proposed method is expected to be linked with other numerical analyses, such as FEM and DEM, and measurement technologies, such as drones and LiDAR.

In Chapter 7, analysis methods for evaluating terrain surface deformation and property changes associated with the interaction between the ground and the machine have been proposed. The validity of the proposed method has been verified by comparing the results obtained from the plate drag analysis and wheel traveling analysis based on the proposed method with the results of model experiments. The proposed method expresses the deformation of the terrain surface due to the interaction between the object and the ground and facilitates a simulation that accurately reproduces the phenomenon confirmed in the experiment.

8.2 Future work

This research has several possible directions to be addressed as future works.

8.2.1 Implementation of the proposed model to MBD analysis

In this thesis, proposals for new analysis methods have been made in Chapter 6 and Chapter 7. Further studies will be possible by introducing these models to MBD analysis such as that performed in Chapter 3. Performing

simulations that consider the posture and mechanism of the vehicle can be useful for various purposes, such as the optimization of work processes and route planning. In addition, the method proposed in this thesis is effective not only for the traveling phenomenon but also for the examination of other works. The plate drag analysis performed in Chapter 7 can be applied to the excavation phenomenon of bulldozers. Performing a vehicle simulation that introduces this method can be useful for examining the optimum excavation process at the site.

8.2.2 Traveling analysis considering turning

In this thesis, we have conducted a simulation focusing on the straight-ahead traveling of a vehicle. However, the vehicle turns in actual phenomena, and hence, a simulation that expresses the traveling phenomenon when the vehicle turns is required. In addition, the ground surface on the side of the tire is deformed even when turning. More accurate simulation becomes possible by applying the model proposed in Chapter 7 to the turning phenomenon.

8.2.3 Cooperation with actual machine control

In this thesis, studies focusing on numerical analysis have been conducted. However, this analysis method should be used to control the actual machine. In recent years, a method called a digital twin, in which the control of an actual machine and simulation in a virtual space are performed in parallel, has attracted attention. More advanced control can be realized by applying the method proposed in this thesis as a simulation for controlling the actual machine. In addition, by combining machine learning and other optimization methods, control and simulation can be performed while optimizing parameters simultaneously. It is expected that the prediction accuracy will be improved by performing the simulation while optimizing, and the control performed based on this method will also be advanced.

Acknowledgement

It is my pleasure to acknowledge the people who have helped me for this work.

First, I wish to express my gratitude to Associate Professor Shingo Ozaki, for his suggestions and guidance throughout this work. The construction of simulation models that we have been working on in this study and the verification using these could not be done without his ideas. In addition, I consulted on various matters other than research activities, which was a great support.

I would be grateful to the members of the thesis examination committee, Associate Professor Shingo Ozaki (Chairman of the committee), Professor Yoshiaki Akiniwa, Professor Yu Qiang, Professor Yasukazu Sato, and Professor Kazushi Sanada for their constructive comments to this study. In particular, Professor Kazushi Sanada gave me a guidance in the laboratory experience program ROUTE when I was in my third year of undergraduate school. The fun of numerical analysis that I experienced there was the catalyst for entering doctoral course.

I wish to express my sincere thanks to everyone who cooperated in writing this thesis. In the MBD analysis conducted in Chapter 3, Mr. Shinya Kondo (Komatsu Ltd.), Koji Uematsu (Komatsu Ltd.), the alumni Mr. Takaki Ogawa, and Mr. Tomoya Suzuki helped me. Alumni Mr. Yoshitomo Oba and Mr. Kota Katsushima helped with the DEM analysis performed in Chapter 4. In the examination conducted in Chapter 5, the alumni Mr. Ryota Aso helped me with the experiment, and my colleague Mr. Yutaro Watanabe helped me with the numerical analysis. In the experiment in Chapter 7, I asked Mr. Hiroki Kawakami who was a member of ROUTE, alumini Mr. Takayuki Ichikawa, and Mr. Kota Katsushima to help me. Furthermore, the experiment apparatus used throughout the research was designed by Professor Taizo Kobayashi (Ritsumeikan University).

I also wish to express my thanks to Professor Taizo Kobayashi (Ritsumeikan University), Associate Professor Genya Ishigami (Keio University),

Associate Professor Shotaro Yamada (Tohoku University), Mr. Mitsuru Yamada (Public Work Research Institute), and Mr. Shunsuke Miyamoto (Komatsu Ltd.), for their advice, which helped me develop my career as a researcher. Moreover, I would like to acknowledge all of my colleagues and the alumni of the Ozaki Laboratory at Yokoahama National University. I will never forget the time I spent enthusiastically discussing with them and enjoying events in the laboratory.

Finally, I would like to express my best gratitude to my family, relatives and Yuka Kamiya for supporting my entire life.

References

[1] Chen Li, Tingnan Zhang, and Daniel I Goldman. A terradynamics of legged locomotion on granular media. *science*, 339(6126):1408–1412, 2013.

[2] Mieczyslaw Gregory Bekker. Theory of land locomotion. 1956.

[3] Jo Yung Wong. *Theory of ground vehicles*. John Wiley & Sons, 2008.

[4] JY Wong. Dynamics of tracked vehicles. *Vehicle system dynamics*, 28(2-3):197–219, 1997.

[5] Vladimir V Vantsevich. Road and off-road vehicle system dynamics. understanding the future from the past. *Vehicle system dynamics*, 53(2):137–153, 2015.

[6] Feng Zhou, Raymond E Arvidson, Keith Bennett, Brian Trease, Randel Lindemann, Paolo Bellutta, Karl Iagnemma, and Carmine Senatore. Simulations of mars rover traverses. *Journal of Field Robotics*, 31(1):141–160, 2014.

[7] Satoshi Tadokoro. *Disaster Robotics: Results from the ImPACT Tough Robotics Challenge*, volume 128. Springer, 2019.

[8] Bernd Schäfer, Andreas Gibbesch, Rainer Krenn, and Bernhard Rebele. Planetary rover mobility simulation on soft and uneven terrain. *Vehicle System Dynamics*, 48(1):149–169, 2010.

[9] Brian Trease, Raymond Arvidson, Randel Lindemann, Keith Bennett, Feng Zhou, Karl Iagnemma, Carmine Senatore, and Lauren Van Dyke. Dynamic modeling and soil mechanics for path planning of the mars exploration rovers. In *International Design Engineering Technical Conferences and Computers and Information in Engineering Conference*, volume 54839, pages 755–765, 2011.

[10] Gaurav Sharma, Sidharth Tiwary, Abhishek Kumar, HN Suresha Kumar, and KA Keshava Murthy. Systematic design and development of a flexible wheel for low mass lunar rover. *Journal of Terramechanics*, 76:39–52, 2018.

[11] Masataku Sutoh, Kenji Nagaoka, Keiji Nagatani, and Kazuya Yoshida. Design of wheels with grousers for planetary rovers traveling over loose soil. *Journal of Terramechanics*, 50(5-6):345–353, 2013.

[12] Raymond E Arvidson, Karl D Iagnemma, Mark Maimone, Abigail A Fraeman, Feng Zhou, Matthew C Heverly, Paolo Bellutta, David Rubin, Nathan T Stein, John P Grotzinger, et al. Mars science laboratory curiosity rover megaripple crossings up to sol 710 in gale crater. *Journal of Field Robotics*, 34(3):495–518, 2017.

[13] Joseph B Raymond and Paramsothy Jayakumar. The shearing edge of tracked vehicle–soil interactions in path clearing applications utilizing multi-body dynamics modeling & simulation. *Journal of Terramechanics*, 58:39–50, 2015.

[14] Weihua Li, Liang Ding, Haibo Gao, Zongquan Deng, and Nan Li. Rostdyn: Rover simulation based on terramechanics and dynamics. *Journal of Terramechanics*, 50(3):199–210, 2013.

[15] Singo Ozaki, Hirotaka Suzuki, Shinya Kondo, and Kouji Uematsu. Fembased terramechancis analysis of tire traveling on multi-layered ground. In *Proceedings of the 8th Americas Regional Conference of the ISTVS*, Detroit, USA, 2016.

[16] Atsunari Katsuki, Macoto Kikuchi, Hiraku Nishimori, Noritaka Endo, and Keisuke Taniguchi. Cellular model for sand dunes with saltation, avalanche and strong erosion: collisional simulation of barchans. *Earth Surface Processes and Landforms*, 36(3):372–382, 2011.

[17] Hiraku Nishimori and Noriyuki Ouchi. Formation of ripple patterns and dunes by wind-blown sand. *Physical Review Letters*, 71(1):197, 1993.

[18] Lucie Guignier, Hirofumi Niiya, Hiraku Nishimori, Dimitri Lague, and Alexandre Valance. Sand dunes as migrating strings. *Physical Review E*, 87(5):052206, 2013.

[19] Nicolas Taberlet, Stephen W Morris, and Jim N McElwaine. Washboard road: the dynamics of granular ripples formed by rolling wheels. *Physical review letters*, 99(6):068003, 2007.

[20] Anne-Florence Bitbol, Nicolas Taberlet, Stephen W Morris, and Jim N McElwaine. Scaling and dynamics of washboard roads. *Physical Review E*, 79(6):061308, 2009.

[21] Bernadette Kenneally, Odon M Musimbi, Judith Wang, and Michael A Mooney. Finite element analysis of vibratory roller response on layered soil systems. *Computers and Geotechnics*, 67:73–82, 2015.

[22] Dieter Pietzsch and Wolfgang Poppy. Simulation of soil compaction with vibratory rollers. *Journal of terramechanics*, 29(6):585–597, 1992.

[23] Tushar Bhandari, Fursan Hamad, Christian Moormann, KG Sharma, and Bernhard Westrich. Numerical modelling of seismic slope failure using mpm. *Computers and Geotechnics*, 75:126–134, 2016.

[24] SB Miles and CL Ho. Rigorous landslide hazard zonation using newmark's method and stochastic ground motion simulation. *Soil Dynamics and Earthquake Engineering*, 18(4):305–323, 1999.

[25] S Di Gregorio, R Kongo, C Siciliano, M Sorriso-Valvo, and W Spataro. Mount ontake landslide simulation by the cellular automata model sciddica-3. *Physics and Chemistry of the Earth, Part A: Solid Earth and Geodesy*, 24(2):131–137, 1999.

[26] Fawu Wang and Kyoji Sassa. Landslide simulation by a geotechnical model combined with a model for apparent friction change. *Physics and Chemistry of the Earth, Parts A/B/C*, 35(3-5):149–161, 2010.

[27] Ha Hong Bui, Ryoichi Fukagawa, Kazunari Sako, and John Craig Wells. Slope stability analysis and discontinuous slope failure simulation by elasto-plastic smoothed particle hydrodynamics (sph). *Géotechnique*, 61(7):565–574, 2011.

[28] Ha H Bui and Ryoichi Fukagawa. An improved sph method for saturated soils and its application to investigate the mechanisms of embankment failure: case of hydrostatic pore-water pressure. *International Journal for Numerical and Analytical Methods in Geomechanics*, 37(1):31–50, 2013.

[29] Peter Sampl and Thomas Zwinger. Avalanche simulation with samos. *Annals of Glaciology*, 38:393–398, 2004.

[30] Harald Norem, Fridtjov Irgens, and Bonsak Schieldrop. Simulation of snow-avalanche flow in run-out zones. *Annals of Glaciology*, 13:218–225, 1989.

[31] Rudolf Sailer, Wolfgang Fellin, Reinhard Fromm, Philipp Jörg, Lambert Rammer, Peter Sampl, and Andreas Schaffhauser. Snow avalanche mass-balance calculation and simulation-model verification. *Annals of Glaciology*, 48:183–192, 2008.

[32] Focal mechanism catalog using initial motion. `http://www.data.jma.go.jp/svd/eqev/data/mech/ini/mc201809.html`.

[33] Hiromitsu Yamagishi and Fumiaki Yamazaki. Landslides by the 2018 hokkaido iburi-tobu earthquake on september 6. *Landslides*, 15(12):2521–2524, 2018.

[34] Richard A. Kerr. Mars rover trapped in sand, but what can end a mission? *Science*, 324(5930):998–998, 2009.

[35] Genya Ishigami, Akiko Miwa, Keiji Nagatani, and Kazuya Yoshida. Terramechanics-based model for steering maneuver of planetary exploration rovers on loose soil. *Journal of Field robotics*, 24(3):233–250, 2007.

[36] Tingnan Zhang and Daniel I Goldman. The effectiveness of resistive force theory in granular locomotion. *Physics of Fluids*, 26(10):101308, 2014.

[37] Hesam Askari and Ken Kamrin. Intrusion rheology in grains and other flowable materials. *Nature materials*, 15(12):1274–1279, 2016.

[38] James Slonaker, D Carrington Motley, Qiong Zhang, Stephen Townsend, Carmine Senatore, Karl Iagnemma, and Ken Kamrin. General scaling relations for locomotion in granular media. *Physical Review E*, 95(5):052901, 2017.

[39] Kenta Nishiyama, Hiroshi Nakashima, Taiki Yoshida, Tomomi Ono, Hiroshi Shimizu, Juro Miyasaka, and Katsuaki Ohdoi. 2d fe–dem analysis of tractive performance of an elastic wheel for planetary rovers. *Journal of Terramechanics*, 64:23–35, 2016.

[40] H Nakashima, H Fujii, A Oida, M Momozu, Y Kawase, H Kanamori, S Aoki, and T Yokoyama. Parametric analysis of lugged wheel performance for a lunar microrover by means of dem. *Journal of Terramechanics*, 44(2):153–162, 2007.

[41] Jerome B Johnson, Anton V Kulchitsky, Paul Duvoy, Karl Iagnemma, Carmine Senatore, Raymond E Arvidson, and Jeffery Moore. Discrete element method simulations of mars exploration rover wheel performance. *Journal of Terramechanics*, 62:31–40, 2015.

[42] Margaret A Knuth, JB Johnson, MA Hopkins, RJ Sullivan, and JM Moore. Discrete element modeling of a mars exploration rover wheel in granular material. *Journal of Terramechanics*, 49(1):27–36, 2012.

[43] H Nakashima, H Fujii, A Oida, M Momozu, H Kanamori, S Aoki, T Yokoyama, H Shimizu, J Miyasaka, and K Ohdoi. Discrete element method analysis of single wheel performance for a small lunar rover on sloped terrain. *Journal of Terramechanics*, 47(5):307–321, 2010.

[44] William Smith and Huei Peng. Modeling of wheel–soil interaction over rough terrain using the discrete element method. *Journal of Terramechanics*, 50(5-6):277–287, 2013.

[45] Wen Li, Yong Huang, Yi Cui, Sujun Dong, and Jun Wang. Trafficability analysis of lunar mare terrain by means of the discrete element method for wheeled rover locomotion. *Journal of Terramechanics*, 47(3):161–172, 2010.

[46] Shingo Ozaki, Kosuke Hinata, Carmine Senatore, and Karl Iagnemma. Finite element analysis of periodic ripple formation under rigid wheels. *Journal of Terramechanics*, 61:11–22, 2015.

[47] Shingo Ozaki and Wataru Kondo. Finite element analysis of tire traveling performance using anisotropic frictional interaction model. *Journal of Terramechanics*, 64:1–9, 2016.

[48] CW Fervers. Improved fem simulation model for tire–soil interaction. *Journal of Terramechanics*, 41(2-3):87–100, 2004.

[49] Omar Gonzalez Cueto, Ciro E Iglesias Coronel, Elvis Lopez Bravo, Carlos A Recarey Morfa, and Miguel Herrera Suárez. Modelling in fem the soil pressures distribution caused by a tyre on a rhodic ferralsol soil. *Journal of Terramechanics*, 63:61–67, 2016.

[50] RC Chiroux, WA Foster Jr, CE Johnson, SA Shoop, and RL Raper. Three-dimensional finite element analysis of soil interaction with a rigid wheel. 2005.

[51] Liang Ding, Haibo Gao, Zongquan Deng, Keiji Nagatani, and Kazuya Yoshida. Experimental study and analysis on driving wheels' performance for planetary exploration rovers moving in deformable soil. *Journal of Terramechanics*, 48(1):27–45, 2011.

[52] MG Bekker. Introduction to terrain-vehicle systems, 1969. *Ann Arbor: The University of Michigan Press*.

[53] Hiroki Tsubaki and Genya Ishigami. Experimental study on wheel-soil interaction mechanics using in-wheel sensor and particle image velocimetry part i: Analysis and modeling of normal stress of lightweight wheeled vehicles. *Journal of Terramechanics*, 93:23–39.

[54] Shota Horiko and Genya Ishigami. Experimental study on wheel-soil interaction mechanics using in-wheel sensor and particle image velocimetry part ii. analysis and modeling of shear stress of lightweight wheeled vehicle. *Journal of Terramechanics*, 91:243–256, 2020.

[55] C Senatore and K Iagnemma. Analysis of stress distributions under lightweight wheeled vehicles. *Journal of Terramechanics*, 51:1–17, 2014.

[56] Hiroaki Katsuragi and Douglas J Durian. Unified force law for granular impact cratering. *Nature physics*, 3(6):420–423, 2007.

[57] Devaraj Van Der Meer. Impact on granular beds. *Annual review of fluid mechanics*, 49, 2017.

[58] Agarwal Shashank, Karsai Andras, Goldman Daniel I, and Kamrin Ken. A generalized resistive force theory for rate-dependent intrusion phenomena in granular media. *arXiv preprint arXiv:2005.10976*, 2020.

[59] Shingo Ozaki, K Hikida, and K Hashiguchi. Elastoplastic formulation for friction with orthotropic anisotropy and rotational hardening. *International Journal of Solids and Structures*, 49(3-4):648–657, 2012.

[60] Shingo Ozaki, Takeru Matsuura, and Satoru Maegawa. Rate-, state-, and pressure-dependent friction model based on the elastoplastic theory. *Friction*, pages 1–16, 2020.

[61] K Hashiguchi and S Ozaki. Constitutive equation for friction with transition from static to kinetic friction and recovery of static friction. *International Journal of Plasticity*, 24(11):2102–2124, 2008.

[62] 田島大輔, 浜本研一, 三浦悟, 登尾大地, 中山裕, 林和彦, and 前原貴徳. 深層強化学習を用いたブルドーザまき出し作業経路の自動生成. In **自動制御連合講演会講演論文集 第** *61* **回自動制御連合講演会**, pages 1473–1475. 自動制御連合講演会, 2018.

[63] Jo-Yung Wong and AR Reece. Prediction of rigid wheel performance based on the analysis of soil-wheel stresses part i. performance of driven rigid wheels. *Journal of Terramechanics*, 4(1):81–98, 1967.

[64] Jo-Yung Wong and AR Reece. Prediction of rigid wheel performance based on the analysis of soil-wheel stresses: Part ii. performance of towed rigid wheels. *Journal of Terramechanics*, 4(2):7–25, 1967.

[65] C Senatore and C Sandu. Off-road tire modeling and the multi-pass effect for vehicle dynamics simulation. *Journal of Terramechanics*, 48(4):265–276, 2011.

[66] <米ラスベガス MINExpo INTERNATIONAL 2016 に実機展示>コマツ、全く新しいコンセプトのキャブレス無人ダンプ車両を開発. `https://home.komatsu/jp/press/2016/product/1188933\_1584.html`.

[67] I.C. Holm. Multi-pass behavior of pneumatic tires. *Journal of Terramechanics*, 6:47.

[68] Grant H Heiken, David T Vaniman, and Bevan M French. Lunar sourcebook-a user's guide to the moon. *Research supported by NASA,. Cambridge, England, Cambridge University Press, 1991, 753 p. No individual items are abstracted in this volume.*, 1991.

[69] Taizo Kobayashi, Hidetoshi Ochiai, Yusuke Suyama, Shigeru Aoki, Noriyuki Yasufuku, and Kiyoshi Omine. Bearing capacity of shallow foundations in a low gravity environment. *Soils and foundations*, 49(1):115–134, 2009.

[70] LL Johnson and RH King. Measurement of force to excavate extraterrestrial regolith with a small bucket-wheel device. *Journal of Terramechanics*, 47(2):87–95, 2010.

[71] Jo Yung Wong. Predicting the performances of rigid rover wheels on extraterrestrial surfaces based on test results obtained on earth. *Journal of Terramechanics*, 49(1):49–61, 2012.

[72] Mingjing Jiang, Fang Liu, Zhifu Shen, and Min Zheng. Distinct element simulation of lugged wheel performance under extraterrestrial environmental effects. *Acta Astronautica*, 99:37–51, 2014.

[73] JP Hambleton and A Drescher. Modeling wheel-induced rutting in soils: Indentation. *Journal of Terramechanics*, 45(6):201–211, 2008.

[74] JP Hambleton and A Drescher. Modeling wheel-induced rutting in soils: Rolling. *Journal of Terramechanics*, 46(2):35–47, 2009.

[75] Kaiming Xia. Finite element modeling of tire/terrain interaction: Application to predicting soil compaction and tire mobility. *Journal of Terramechanics*, 48(2):113–123, 2011.

[76] Masataku Sutoh, Junya Yusa, Tsuyoshi Ito, Keiji Nagatani, and Kazuya Yoshida. Traveling performance evaluation of planetary rovers on loose soil. *Journal of Field Robotics*, 29(4):648–662, 2012.

[77] T Shikanai, K Hashiguchi, Y Nohse, M Ueno, and T Okayasu. Precise measurement of soil deformation and fluctuation in drawbar pull for steel and rubber-coated rigid wheels. *Journal of terramechanics*, 37(1):21–39, 2000.

[78] Taizo Kobayashi, Yoichiro Fujiwara, Junya Yamakawa, Noriyuki Yasufuku, and Kiyoshi Omine. Mobility performance of a rigid wheel in low gravity environments. *Journal of Terramechanics*, 47(4):261–274, 2010.

[79] Raymond Nen Yong, Ezzat A Fattah, and Nicolas Skiadas. *Vehicle traction mechanics*. Elsevier, 2012.

[80] T. Muro. Terramechanics. *Gihodo shuppan, in Japanese*, pages 1–235, 1993.

[81] Yang Yang, Yi Sun, Shugen Ma, and Ryohei Yamamoto. Characteristics of normal and tangential forces acting on a single lug during translational motion in sandy soil. *Journal of Terramechanics*, 55:47–59, 2014.

[82] Yang Yang, Yi Sun, and Shugen Ma. Drawbar pull of a wheel with an actively actuated lug on sandy terrain. *Journal of Terramechanics*, 56:17–24, 2014.

[83] Shashank Agarwal, Carmine Senatore, Tingnan Zhang, Mark Kingsbury, Karl Iagnemma, Daniel I Goldman, and Ken Kamrin. Modeling of the interaction of rigid wheels with dry granular media. *Journal of Terramechanics*, 85:1–14, 2019.

[84] BT Werner. Eolian dunes: computer simulations and attractor interpretation. *Geology*, 23(12):1107–1110, 1995.

A Code for terramechanics analysis

An example of the MATLAB function for the terramechanics simulation introduced in this study is shown below. This chapter presents the terramechanics model used in the single-wheel locomotion analysis.

A.1 Terramechanics model

Listing 1: Terramechanics model (BWR model) used for single-wheel traveling analysis

```
function [Fx,Fz,Ty,Fz_Damp,Delta_ij,M_ij,sigmaX,sigmaZ] =
    TerraModel(x,y,z,vz,s_dyn,Z_field,rho_field,Para_Terra,
    Wheel_mat)

%%%%%%%%%%%%%%%%%%%%%%%%%%%%%%%%
i_Terra=1;
%Terramechanics model
R=Para_Terra(i_Terra);
i_Terra=i_Terra+1;
B=Para_Terra(i_Terra);
i_Terra=i_Terra+1;

c=Para_Terra(i_Terra);
i_Terra=i_Terra+1;
phi=Para_Terra(i_Terra);
i_Terra=i_Terra+1;
kc=Para_Terra(i_Terra);
i_Terra=i_Terra+1;
kphi=Para_Terra(i_Terra);
i_Terra=i_Terra+1;
n=Para_Terra(i_Terra);
i_Terra=i_Terra+1;
kx=Para_Terra(i_Terra);
i_Terra=i_Terra+1;
a0=Para_Terra(i_Terra);
i_Terra=i_Terra+1;
a1=Para_Terra(i_Terra);
i_Terra=i_Terra+1;
g=Para_Terra(i_Terra);
i_Terra=i_Terra+1;
```

```
29
30 dtheta=Para_Terra(i_Terra);
31 i_Terra=i_Terra+1;
32 dw=Para_Terra(i_Terra);
33 i_Terra=i_Terra+1;
34
35 Xmin=Para_Terra(i_Terra);
36 i_Terra=i_Terra+1;
37 Ymin=Para_Terra(i_Terra);
38 i_Terra=i_Terra+1;
39 dx=Para_Terra(i_Terra);
40 i_Terra=i_Terra+1;
41 dy=Para_Terra(i_Terra);
42 %%%%%%%%%%%%%%%%%%%%%%%%%%%%%%%
43
44 Fx=0;
45 Fz=0;
46 Ty=0;
47
48 Field_size=size(Z_field);
49
50 imax=Field_size(1,1);
51 jmax=Field_size(1,2);
52
53 M_ij=zeros(imax,jmax);
54 Delta_ij=zeros(imax,jmax);
55
56 Wheel_size=size(Wheel_mat);
57 i_terra_max=Wheel_size(1,1);
58 j_terra_max=Wheel_size(1,2);
59
60 sigmaX=zeros(i_terra_max,j_terra_max);
61 sigmaZ=zeros(i_terra_max,j_terra_max);
62
63 w=dw/2;
64 j_terra=1;
65 while j_terra<=j_terra_max
66
67     %
68     thetar=10^-100;
69     thetaf=10^-100;
70     thetac=-pi;
71     StateRear=1;
72     StateInside=0;
```

```
73      i_find_theta=1;
74      while thetac<=pi
75          xc=x+R*sin(thetac);
76          yc=y-B/2-dw/2+dw*j_terra;
77          zc=z-R*cos(thetac);
78
79          %
80          i_field=ceil( (xc-Xmin)/dx );
81          j_field=ceil( (yc-Ymin)/dy );
82
83          %
84          Delta = zc - Z_field(i_field,j_field);
85
86          if StateRear==1&&Delta<=0&&thetac<=0
87              StateRear=0;
88              StateInside=1;
89              thetar=-thetac;
90              if thetar>=pi/2
91                  thetar=pi/2;
92              end
93          elseif StateInside==1&&Delta>=0&&thetac>=0
94              StateInside=0;
95              thetaf=thetac;
96              if thetaf>=pi/2
97                  thetaf=pi/2;
98              end
99          elseif StateInside==1&&thetac>=pi/2
100             StateInside=0;
101             thetaf=pi/2;
102         end
103
104         i_find_theta=i_find_theta+1;
105         thetac=thetac+dtheta;
106     end
107     thetam=(a0+a1*s_dyn)*thetaf;
108
109
110     theta=-pi;
111     i_terra=1;
112     while i_terra<i_terra_max
113
114         l=R*(thetaf+thetar);
115         jx=R*(thetaf-theta-(1-s_dyn)*(sin(thetaf)-sin(theta))
                ;
```

```
116         if thetam<=theta&&theta<=thetaf
117             Sinkage_Bekker=R*(cos(theta)-cos(thetaf));
118         elseif -thetar<=theta&&theta<=thetam
119             Sinkage_Bekker=R*(cos(thetaf-(theta+thetar)/(
                    thetam+thetar)*(thetaf-thetam))-cos(thetaf));
120         else
121             Sinkage_Bekker=0;
122             jx=0;
123         end
124
125         %
126         xc=x+R*sin(theta);
127         yc=y-B/2-dw/2+dw*j_terra;
128         zc=z-R*cos(theta);
129
130         %
131         i_field=ceil( (xc-Xmin)/dx );
132         j_field=ceil( (yc-Ymin)/dy );
133
134         %
135         if l>=B
136             sigma=(c*kc+rho_field(i_field,j_field)*g*B*kphi)
                    *(Sinkage_Bekker/B).^n;
137         elseif l<B
138             sigma=(c*kc+rho_field(i_field,j_field)*g*l*kphi)
                    *(Sinkage_Bekker/l).^n;
139         else
140             sigma=0;
141         end
142         tau_B =(c+sigma*tan(phi))* (1-exp(-jx/kx));
143
144         %
145         sigmaX(i_terra,j_terra)=-sigma*sin(theta)+tau_B*cos(
                theta);
146         sigmaZ(i_terra,j_terra)= sigma*cos(theta)+tau_B*sin(
                theta);
147
148         if sigmaZ(i_terra,j_terra)<=0
149             sigmaX(i_terra,j_terra)= 0;
150             sigmaZ(i_terra,j_terra)= 0;
151         end
152
153         %
154         Delta_ij(i_field,j_field)=max(Delta_ij(i_field,j_field
```

```
            ),Z_field(i_field,j_field)-zc);
155
156         if Delta_ij(i_field,j_field)>0
157             if sigmaX(i_terra,j_terra)<0
158                 M_ij(i_field,j_field)=1;
159             elseif sigmaX(i_terra,j_terra)>0
160                 M_ij(i_field,j_field)=2;
161             end
162         end
163
164         %
165         dA=R*dtheta*dw;
166         Fx=Fx+sigmaX(i_terra,j_terra)*dA;
167         Fz=Fz+sigmaZ(i_terra,j_terra)*dA;
168         Ty=Ty+R*tau_B*dA;
169
170         theta=theta+dtheta;
171         i_terra=i_terra+1;
172     end
173
174     w=w+dw;
175     j_terra=j_terra+1;
176 end
177 Damp_z=Fz/(R*1.5);
178 Fz_Damp=Fz-Damp_z*vz;
179 if Fz_Damp<=0
180     Fz_Damp=0;
181 end
182
183 end
```